Conceptual Design of the Lambda Disks Detector for the $\overline{\text{P}}$ANDA Experiment

Ph.D. Thesis

By

AJAY KUMAR

DISCIPLINE OF PHYSICS

INDIAN INSTITUTE OF TECHNOLOGY INDORE

MAY 2016

Conceptual Design of the Lambda Disks Detector for the $\overline{\text{P}}$ANDA Experiment

A THESIS

Submitted in partial fulfillment of the
requirements for the award of the degree

of

DOCTOR OF PHILOSOPHY

by

AJAY KUMAR

DISCIPLINE OF PHYSICS

INDIAN INSTITUTE OF TECHNOLOGY INDORE

MAY 2016

.

Dedicated

to

My Loving Mother

Acknowledgements

This thesis becomes a reality with the kind support and help of many individuals, I would like to extend my sincere thank to all of them.

Foremost, I am grateful to Almighty God for giving me wisdom , the strength, and good health that were necessary to complete this thesis work.

Firstly, I would like to express my sincere gratitude to my supervisor Prof. Ankhi Roy and Co-supervisor Prof. Raghunath Sahoo for the continuous support during my Ph.D, for their patience and motivation. Their guidance helped me a lot for my research work. I could not have imagined having a better supervisor for my Ph.D other than Prof. Ankhi Roy.

Besides my supervisors, I would like to thank my PSPC committee members: Prof. Manavendra Mahato and Prof. Abhinav Kranti for their insightful comments and encouragement, but also for hard questions, which incented me to widen my research from various perspectives.

My sincere thanks also goes to Prof. James Ritman, Director, IKP, Forschungszentrum Jülich, Germany and Dr. Tobias Stockmanns, who have provided me an opportunity to join their team as visiting a research scholar, and gave access to the laboratory and research facilities. Without their precious support, it would not be possible to conduct this research. I want to extend my special thanks to Dr. Dariusch Deerman, Dr. Andreas Herten, Dr. Huagen Xu, Ludovico Bianchi, Lu Cao, Jennifer Puetz for their wonderful interactions and help during my stay in Germany.

I would like to express my sincere gratitude to Prof. Pradeep Mathur, Director, IIT Indore, for his continuous support throughout my Ph.D. period during my stay in IIT Bombay and IIT Indore.

My special thank and tribute also goes to late. Prof. P. N. Puntambekar, who has played a role of local guardian during my hard time in the

starting of my Ph.D.

I would like to thank Prof. Raghava Verma for his valuable advises during my Ph.D course work at IIT Bombay.

I wish to express my special thank to Dr. Prakher Garg, for his priceless time and help during my thesis writing period. Apart from this, I have learned so many things form his valuable comments, encouragement and motivation which he gave me during his stay in IIT Indore.

I take this opportunity to express my gratitude to all faculty members of the Discipline of Physics of IIT Indore for their help and support.

I thank my fellow lab mates Ankita Goswami, Sudeep Ghosh, Samsul and Sudheer for their stimulating discussions during this journey.

I would like to convey my thank to my dear friends Aditya Nath Mishra, Mahesh Chandra, Shailendra Kumar Saxena, Ajay Pratap Singh, Fozia Aziz, Bhausahib Dhokale, Rajendra Nasani, Bhagwati Sharma. Nitesh Saxena, Nishant Saxena for their kind help every time and more than their moral support during ups and downs in this period. Also I will never forget all the fun, we have had together throughout the whole research period.

Last but not least, I would like to thank my family: My father and to my brother, sister with beloved Nonu and Donu for their support, patience and strong believe in me with unconditional love in this whole duration.

(Ajay Kumar)

Abstract

$\overline{\text{P}}$ANDA (anti**P**roton **AN**nihilations at **DA**rmstadt) is a future experiment in the FAIR (**F**acility for **A**ntiproton and **I**on **R**esearch) facility located next to GSI, Darmstadt, Germany. The HESR (**H**igh **E**nergy **S**torage **R**ing) of the FAIR facility will provide antiproton beam of any momentum between 1.5 GeV/c and 15 GeV/c.

Main physics motivation of $\overline{\text{P}}$ANDA is to explore the low energy regime of Quantum Chromodynamics (QCD). Mainly it will focus on the following areas: charmonium spectroscopy, search for the gluonic states, hadrons in nuclear matter, hypernuclei physics and electromagnetic processes.

The $\overline{\text{P}}$ANDA detector setup is made up of two major parts - target spectrometer and forward spectrometer. Target spectrometer consists of tracking detectors, particle identification detectors, electromagnetic calorimeter. Micro Vertex Detector (MVD) is the innermost tracking detector of the target spectrometer. It has four barrel layers and six disks layers. After the last disk layer of MVD and first layer of Gas Electron Multipliers (GEM), there is a large detector free volume. By including the Lambda Disks Detector (LDD) into the $\overline{\text{P}}$ANDA setup, there is a possibility to extend hyperon study in the $\overline{\text{P}}$ANDA physics program. Hyperons have a large decay length of the order of a few centimeters. Therefore, they travel a large distance before decaying into other particles. The LDD will have the capability to improve the reconstruction probability of hyperons having a longer decay length.

Also present database of hyperon physics is not complete. PS185 experiment at the LEAR (**L**ow **E**nergy **A**ntiproton **R**ing) facility had measured $\Lambda\bar{\Lambda}$ cross-section from its beam production threshold momentum (1.436 GeV/c) to 2 GeV/c and Bubble Chamber experiment provides cross-section above 2 GeV/c with low statistics and there is no data available above 7 GeV/c. Not only addition of LDD will verify previous measured cross-section below 7 GeV/c, it may also provide data above 7 GeV/c with large statistics.

In the proposed geometry of the Lambda Disks Detector, the outer and inner ring of these disks are both made up of Double-sided Silicon Strip Sensors. The outer ring has been kept similar to the outermost layers of the MVD forward disks. Both sides of the trapezoidal silicon strip sensors for the outer ring of the Lambda Disks have 512 strips with a pitch of 67.5 μm. Each sensor has a stereo angle of 15^0 between the two long edges and the sensor thickness is 285 μm. Inner ring of the disks has 768 strips per side with a pitch of 45 μm. Each sensor of inner ring has a stereo angle of 25.138^0 with sensor height of 46 mm.

To test the capability of LDD, we have simulated and reconstructed $\bar{p}p \rightarrow \Lambda\bar{\Lambda}$ channel under the $\overline{\text{P}}$ANDA simulation framework at beam momentum 1.8 GeV/c that is near threshold beam momentum of the reaction and other at 4 GeV/c to compare the performance of the detector with increasing beam momentum. In order to perform the feasibility studies for the Lambda Disks Detector of the $\overline{\text{P}}$ANDA experiment, we have studied the angular distributions from the daughter particles of Lambda (Λ) hyperons to map the direction of the final state particles inside the target spectrometer.

The decay length of the produced hyperons is studied which is in good agreement with the PDG value ($c\tau$ = 7.89 cm). Momentum correlations (p_z versus p_T) of Λ hyperons as well as their decay products are studied to understand the kinematics of these particles. The decay vertex positions of produced Λ hyperons are studied to make estimate of events decaying before the LDD since this detector detects final state particles (p, $\bar{p}$, π^-, π^+) from this decay channel.

We have also studied vertex and momentum resolution from $\bar{p}p \rightarrow \Lambda\bar{\Lambda}$ channel with and without the LDD. We have found that vertex resolution of Λ and $\bar{\Lambda}$ remain unchanged after the addition of LDD. However, we observed that the addition of LDD spoils the momentum resolution in the z-direction and remain unchanged in transverse direction. Hit count studies of the daughter particles from both hyperons are performed and observed that hit counts are increased after the addition of LDD to the detector

set up. At low beam momentum (1.8 GeV/c), the most significant effect is the increment in the number of hits of protons in the angular range of the Lambda Disks. The average number of hit points per track rises above four, which allows individual tracking of the particle. At a higher beam momentum (4.0 GeV/c), antiprotons are forward boosted in comparison to protons and usually have more than six hits in angular coverage of the Lambda Disks. Final state pions (π^+ and π^-) register more than six hits after the addition of LDD to the $\overline{\text{P}}$ANDA. The increment in the particle hits after adding the LDD is a positive sign towards its development. We have estimated mass resolution and reconstruction efficiency of Λ and $\bar{\Lambda}$ hyperons with and without the LDD, which are most important parameters for the feasibility studies of this detector. A double Gaussian function is fitted to the mass distribution of hyperons because the combinatorial background is also Gaussian in nature.

Average reconstruction efficiency of Λ is around 42% at the lower beam momentum and 25% at the higher beam momentum whereas for $\bar{\Lambda}$ it is 48% at the lower beam momentum and 52% at the higher momentum. Average reconstruction efficiency of Λ is decreasing whereas $\bar{\Lambda}$ reconstruction efficiency is increasing with the increase with the beam momentum. Reconstruction efficiency of $\Lambda\bar{\Lambda}$ events is estimated and found to be 28.5% and 20% at beam momenta 1.8 GeV/c and 4.0 GeV/c respectively.

As the addition of a new detector should not affect the reconstruction of already well reconstructed channels, therefore, we have studied two mesonic channels $\bar{p}p \rightarrow D^{*+}D^{*-} \rightarrow D^0\pi^+\bar{D}^0\pi^-$ and $\bar{p}p \rightarrow J/\psi\pi^+\pi^-$ in the presence of LDD. These two selected channels are very important for charmonium physics program of the $\overline{\text{P}}$ANDA experiment. Reconstruction efficiency and mass resolution of the produced mesons are studied for these two channels. Simulation results show that reconstruction efficiency of these mesons are not affected after the addition of LDD to the $\overline{\text{P}}$ANDA setup.

As a part of this thesis to gain hardware experience, we have done the characterization of trapezoidal Double-sided Silicon Strip Sensors. We

have perform Quality Assurance (QA) tests which is basically I-V and C-V characterization of these sensors. Most important parameters of QA tests are leakage current and depletion voltage of the whole sensor as well as individual strips. It is essential to know these parameters before the operation. We have done the characterization of Double-sided Silicon Strip Sensors using two different biasing techniques with a probe station and a dedicated test board setup in Forschungszentrum Jülich, Germany. From the I-V and C-V characterization results, we have observed that measured values of the required parameters are in good agreement with the values, provided by the manufacturer (CiS) of these sensors. The value of leakage current and depletion voltage for each characterized sensor are found near about 4 μA and 100 V respectively. Leakage current and depletion voltage of strips from the n-side and the p-side are also measured and found near about 2 μA and 100 V respectively.

The QA tests on the DC-DC converters are also performed which is required for constant power supply to each sensor used for the LDD. The QA tests include I-V characteristics, efficiency measurements, load regulation on the available DC-DC converter modules. Our results are found in good agreement with the data provided by the manufacturers.

One of the important studies for a developing detector is the estimation of material budget. We have performed material budget study for the current geometry of the Lambda Disks. This geometry consist of silicon sensors in inner and outer ring with support structure made up of the carbon. Materials used for the LDD should be as low as possible due to the restriction imposed by the detectors located in the forward and backward direction. The concerning parameter for the material budget is fractional radiation length and it is found 20% of X_0, complete radiation length.
The organization of the thesis is as follows:

Chapter 1: This chapter gives a short introduction of Standard Model and QCD. We have discussed $\overline{\text{P}}$ANDA physics program in details. It elaborates how the $\overline{\text{P}}$ANDA experiment could shed light on some of the unanswered questions in hadron physics and non-perturbative regime of QCD. At the

end, we have discussed the present status of hyperon physics and requirement of Lambda Disks Detector for the reconstruction of hyperons.

Chapter 2: This chapter describes the Facility of Antiproton and Ion research which will be future accelerator facility at GSI. We basically discuss the various experimental programs which use this facility. Special emphasis has been given to the $\overline{\text{P}}$ANDA experiment and its sub-detector systems.

Chapter 3: In this chapter Lambda Disks Detector layout is discussed. A description of the detector technology, material budget of the LDD is given. The efforts have been made towards the mechanical services for the Lambda Disks Detector.

Chapter 4: Simulation studies for the $\overline{\text{P}}$ANDA Lambda Disks Detector are presented in details for three physics channels in this chapter.

Chapter 5: This chapter describes the characterization of the Double-sided Silicon Strip Sensors and DC-DC converters.

Chapter 6: This chapter provides summary and conclusions drawn from this thesis work and future outlook.

List of Publications

1. **"Acceptance Studies of an Additional Lambda Disk Detector for the PANDA Experiment",**
   Ajay Kumar, Ankhi Roy [for the PANDA Collaboration].
   Nucl. Part. Phys. Proc. **270-272**, *50-53 (2016).*

2. **"Study of doubly strange systems using stored antiprotons",**
   B. Singh,...., **A. Kumar**, A. Roy et al. [For the PANDA Collaboration]. *Nucl. Phys. A* **954** *(2016) 323.*

3. **"Experimental access to Transition Distribution Amplitudes with the PANDA experiment at FAIR",**
   B. P. Singh,...., **A. Kumar**, A. Roy, R. Sahoo et al. [For the PANDA Collaboration]. *Eur. Phys. J. A* **51**, *no. 8, 107 (2015).*

4. **"Development of the Lambda Disk Detector for the PANDA Experiment",**
   Ajay Kumar, Ankhi Roy [For the PANDA Collaboration].
   Proceedings of the International DAE Symp. on Nucl. Phys. 58 (2013).

5. **"Simulations to Measure Hyperons using Lambda Disk",**
   Ajay Kumar [For the PANDA Collaboration].
   Proceedings of the DAE Symp. on Nucl. Phys. 57 (2012).

6. **"Charactrization of Double-Sided Micro Strip Silicon Sensors with different biasing technologies",**
   Ajay Kumar et al., [For the PANDA Collaboration]. (to be submitted to Nucl. Instrum. Meth.).

7. **"Feasibility studies of time-like proton electromagnetic form factors at PANDA at FAIR",** B. Singh,...., **A.Kumar**, A. Roy et al. [For the PANDA Collaboration]. (to be submitted to EPJ)

Contents

Figures

Tables

Chapter 1

Introduction

One of the main aims of physics is to understand the world around us. A curious mind wants to find and understand the basics building blocks of matter. Particle physics explores this type of fundamental queries. Physicists have developed a theory called the Standard Model of particle physics which describes the universe in terms of matter and force. In this chapter, we will talk about the Standard Model and Quantum Chromodynamics (QCD), the theory of strong force. In this thesis, we have introduced a new detector for the $\overline{\text{P}}$ANDA experiment named as Lambda Disks Detector. The aim of this detector is to improve the efficiency of hyperons. So, we will illustrate $\overline{\text{P}}$ANDA physics program, present status of hyperon physics and the concept of Lambda Disks Detector here.

1.1 The Standard Model

Standard Model of particle physics deals with all the elementary particles and the fundamental interactions in nature. The interactions correspond to three of the known fundamental forces in nature: the strong force, the weak force, the electromagnetic force. They are mediated by particles called gauge bosons. Photon is the mediator of electromagnetic force. Gluons are the force carriers of strong force. $W^{\pm}$ and Z bosons are mediator for the weak force. Atoms are made up of electrons and nucleus. Electron is one of the elementary particles. However, nucleus is made up of protons and neutrons, which are examples of composite particles, named as hadrons. Hadrons are made up of elementary particles called as quarks and quarks are classified according to different flavors quantum numbers - up (u), down

(d), charm (c), strange (s), top (t) and bottom (b). Each quark and antiquark can have any of the three different color quantum numbers (red, blue, green). Leptons include electrons (e), electron neutrinos (ν_e), muons (μ) and muon neutrinos (ν_μ), taus (τ), tau neutrinos (ν_τ). Each lepton has its own antilepton. All elementary particles and mediators of fundamental forces are tabulated in Figure 1.1. The Higgs boson is as shown in the Figure different from the other bosons. It does not mediate any force, but it interacts with the other elementary particles with a strength depending on their mass. The Higgs boson is part of the mechanism that gives mass to the other elementary particles in the Standard Model. The fourth known force in nature, gravity, acts very weakly for the elementary particles and is not included in the Standard Model.

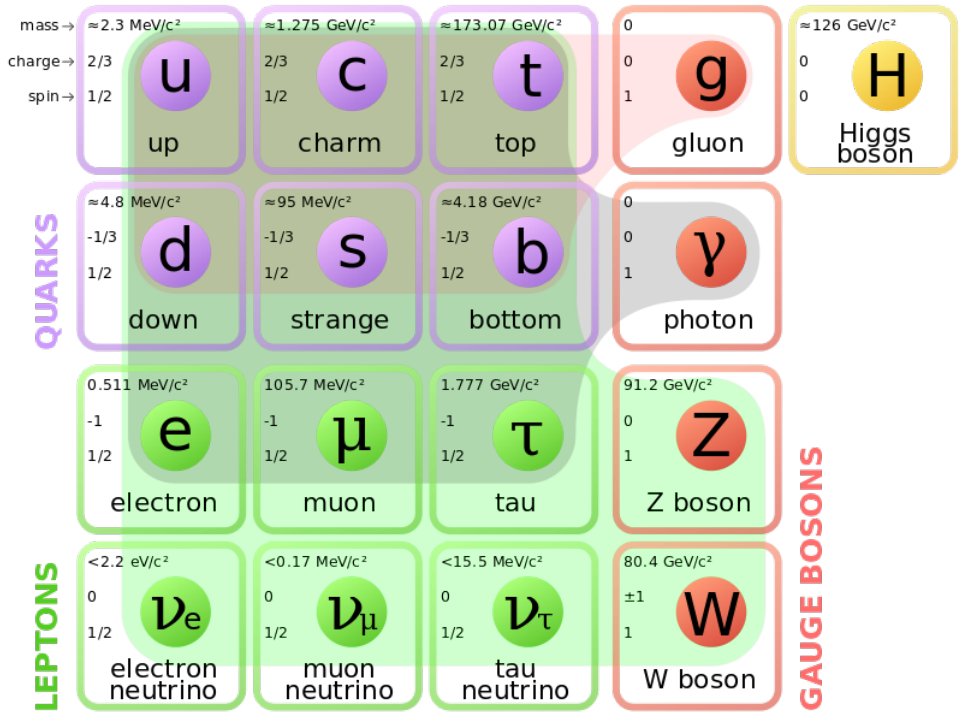

Figure 1.1: Elementary particles of the Standard Model [1].

1.2 Quantum Chromodynamics (QCD)

QCD is the theory of strong interaction, a fundamental force describing the interactions of quarks and gluons found in hadrons. QCD describes the interaction of color-charged particles via the exchange of gluons, which

play a role similar to that of photons in QED. Both gluons and photons are massless as demanded by gauge symmetry of quantum field theory. There is however one striking difference between the two theories: gluons carry color charge and therefore interact with each other, whereas photons are electrically neutral and hence do not interact with each other. As a consequence, at short distances or correspondingly at large momentum transfers, the coupling becomes small and the quarks inside the hadrons behave as free, non-interacting particles. This phenomenon is known as asymptotic freedom. In this kinetic region perturbative QCD - similar to the method used in QED - can be applied to calculate the interaction between quarks and gluons. On the other hand, at large distances (equivalent to small momentum transfers), the coupling constant becomes large leading to confinement of quarks inside hadrons. In nature, therefore one observes color singlet states only. The variation of coupling constant as a function of energy scale is shown in Figure 1.2.

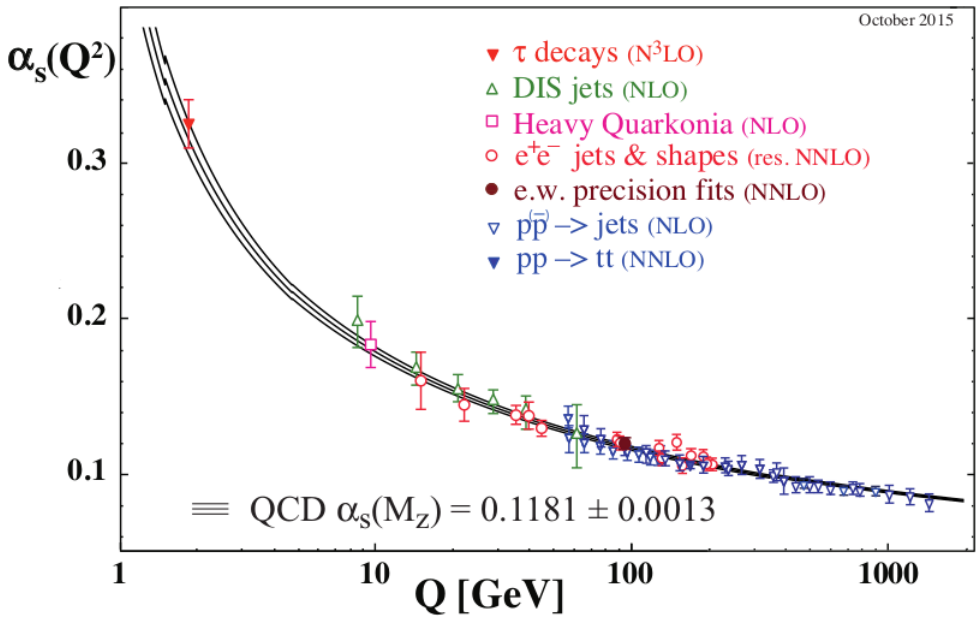

Figure 1.2: Measurements of coupling constant (α_s) as a function of the energy scale (Q). Figure is adopted from Ref. [2].

Hadrons can be of two different types - mesons which are made up of quark and antiquark ($q\bar{q}$) and baryons which are the combinations of three quarks (qqq) or antiquarks ($\bar{q}\bar{q}\bar{q}$). Construction of hadrons are described

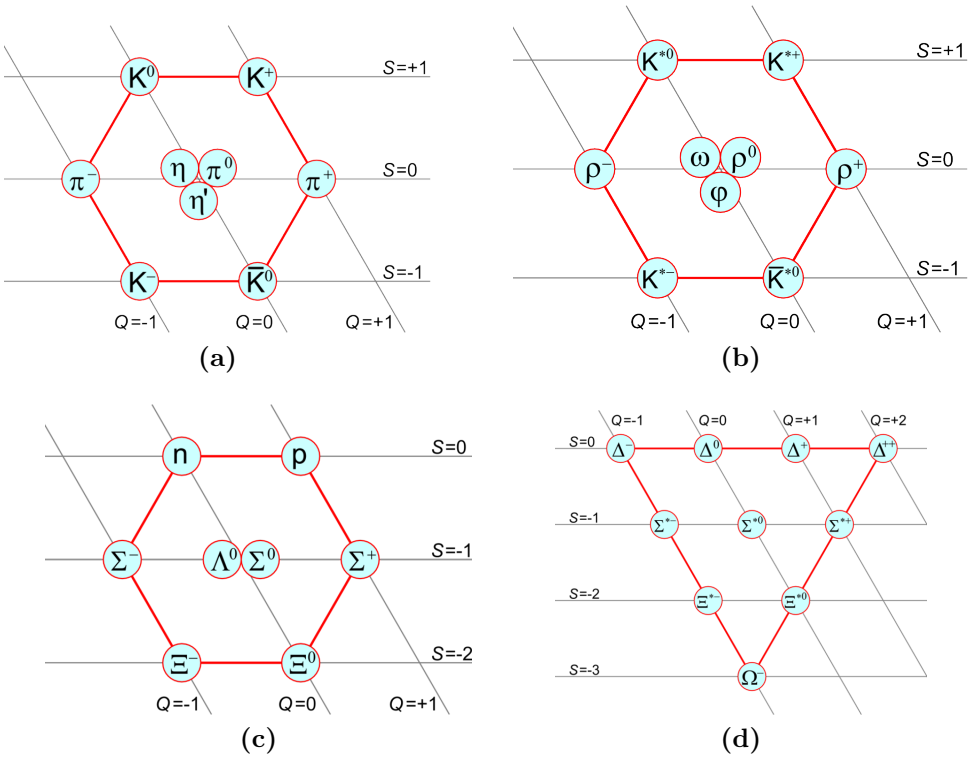

Figure 1.3: Eightfold classification of Mesons and Baryons. Mesons are classified as spin 0 and spin 1 shown in panels (a) and (b). In panels (c) and (d), baryons with spin 1/2 and spin 3/2 are shown [3] [4].

by taking into account three lightest quarks (u, d, s) in SU(3) symmetry. All baryons are classified into ground state octet ($J^p = \frac{1}{2}^+$) and decuplet ($J^p = \frac{3}{2}^+$). Similarly mesons form two nonets - one is spin 0 ($J^p = 0^-$) and other is spin 1($J^p = 1^-$). Figure 1.3 shows the baryon and meson multiplets.

1.2.1 Strange Hyperons

Strange hyperons are special types of baryons which contain at least one strange quark, but no charm, bottom or top quark. Strange hyperons, being fermions, obey Fermi-Dirac Statistics. They all interact via strong force and decay through weak interaction. Some of the strange hyperons are Λ, Σ, Ξ as shown in Figure 1.3 and tabulated with their properties in Table 1.1.

Strange hyperon production in $\bar{p}p$ system gives important information about the strangeness production. Strangeness production is governed by

Hyperon	Quarks	Mass [MeV/c^2]	$c\tau$ [cm]	Main decay
Λ	uds	1116	7.89	$p\pi^-$
Σ^+	uus	1189	2.4	$p\pi^0$
Σ^0	uds	1193	2.2×10^{-9}	$\Lambda\gamma$
Σ^-	dds	1197	2.4	$n\pi^-$
Ξ^0	uss	1315	8.7	$\Lambda\pi^0$
Ξ^-	dss	1321	4.9	$\Lambda\pi^-$
Ω^-	sss	1672	2.5	ΛK^-

Table 1.1: Properties of strange hyperons.

the mass of the strange quark ($m_s \approx 100MeV$) which is very near to QCD cutoff ($\Lambda_{QCD} \approx 200MeV$) as shown in Figure 1.2. In this QCD regime, perturbative QCD can not be implemented because coupling is so strong that one can not use quarks and gluons as relevant degrees of freedom. Therefore, production of strange hyperon study will shed light about the relevant degrees of freedom in the intermediate region of QCD.

1.3 $\overline{\text{P}}$ANDA Physics Program

$\overline{\text{P}}$ANDA (anti**P**roton **AN**nihilations at **DA**rmstadt) is one of the experiments of the FAIR (**F**acility for **A**ntiproton and **I**on **R**esearch) Facility in Darmstadt, Germany. $\overline{\text{P}}$ANDA aims to study interactions between antiproton beam and fixed target proton (or nuclei) in the momentum range of 1.5 - 15 GeV/c using the HESR (**H**igh **E**nergy **S**torage **R**ing). Energy range of $\overline{\text{P}}$ANDA will allow to study the non-perturbative and overlap region of perturbative and non-perturbative regime of the strong interaction. Following subsections describe the main physics motivations of the $\overline{\text{P}}$ANDA experiment [5].

1.3.1 Charmonium Spectroscopy

One of the main physics goals of $\overline{\text{P}}$ANDA is to explore all the charmonium states as predicted by the lattice QCD as shown in Figure 1.4. Charmonium can be directly formed in $\bar{p}p$ annihilations through the coherent annihilation of the three quarks in the proton and three antiquarks in an-

tiproton. Charmonium is a bound state of c and $\bar{c}$ like positronium which is the bound state of electron and positron. Both charmonium and positronium are the combined states of particle and anti-particle. So we expect charmonium will throw light on the strong interaction as positronium has revealed a lot about electromagnetic interaction. There are huge discrepancies among different experiments concerning the width and mass of the charmonium states. $\overline{\text{P}}$ANDA is capable of measuring the same with high precision.

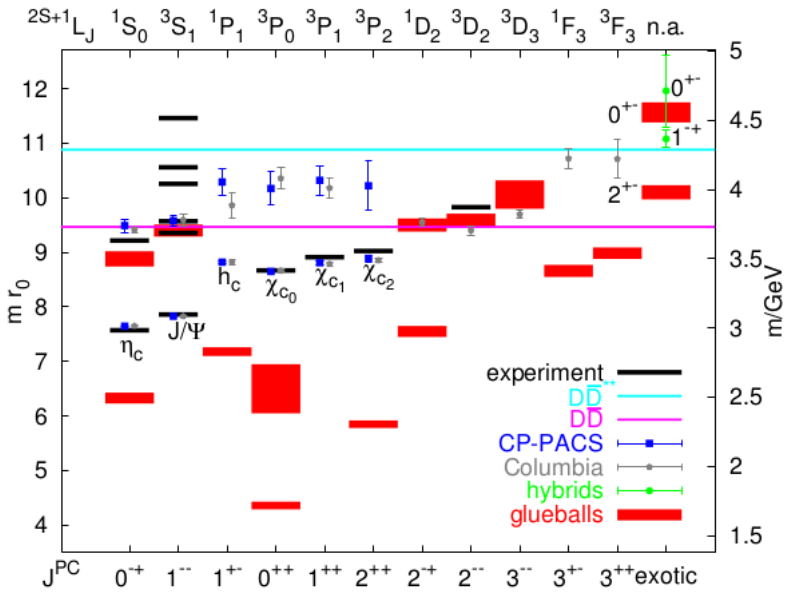

Figure 1.4: LQCD predictions for the charmonium. Figure is adopted from Ref. [5].

1.3.2 Open Charm spectroscopy

Open charm is a meson which contains one light quark (u, d, s) and one charm quark. It is named as open charm because charm quantum number (c) is not equals to zero. Open charm is similar like hydrogen atom which is a combination of light electron and the heavy nucleus. Open charm can give hints to a better understanding of the strong interaction like the way hydrogen has contributed to the electromagnetic force. $\overline{\text{P}}$ANDA has plan to study spectrum of D and D_s mesons with high precision and precise measurement of width.

1.3.3 Search for Gluonic Excitations

One challenge in hadron physics is to look for gluonic excitation states - glueball and hybrid. Glueball is the gluonic excitation without any valence quark and hybrid is a combination of quarks ($q\bar{q}$) and excited gluons. Lattice QCD predicts mass spectrum of glueballs as shown in Figure 1.5. $\overline{\text{P}}$ANDA is expecting to search most of the states because proton and antiproton annihilation creates ideal environment for gluonic states and also most of them lies within the $\overline{\text{P}}$ANDA energy range. If glueball exists, there will be an opportunity to know the strong force directly and their study will reveal structure of the QCD vacuum.

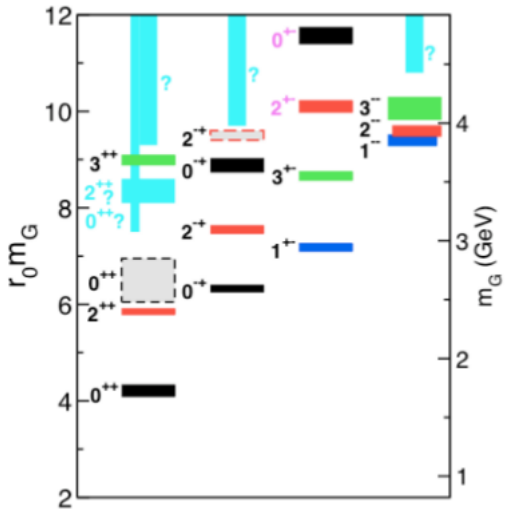

Figure 1.5: The LQCD glueball spectrum in pure SU(3) gauge theory. Figure is adopted from Ref. [5].

1.3.4 Hypernuclear Physics

Hypernuclei are the nuclei in which one or more nucleons are replaced by hyperons. Strangeness can be part of the nuclei in this method. Hyperon inside the hypernuclei can be excited to the higher state and used as a good probe to know the nuclear structure. Advantage of hypernuclei is that decay length of the hyperon is very long as it decays through weak interactions. So spectroscopic methods can be used for its study. Another advantage is that it is not restricted by the Pauli exclusion principle because

of its strangeness.

1.3.5 Study of Hadrons in Nuclear Matter

Study of medium modifications of hadrons in a hadronic matter is investigated in the light quark sector. It helps to understand the origin of hadron masses in the context of spontaneous chiral symmetry breaking in QCD and its partial restoration in a hadronic environment. This study can be extended in both charm sector (open and hidden) due to high intensity antiprotons up to 15 GeV/c.

1.3.6 Electromagnetic Processes

$\overline{\text{P}}$ANDA will be able to investigate the structure of the nucleon using electromagnetic processes. For instance, Deeply Virtual Compton Scattering (DVCS) and the process $pp \rightarrow e^+e$ will allow the determination of the electromagnetic form factors of the protons in the timelike region over an extended q^2 region.

1.4 Present Status of Hyperon Physics

The $\bar{p}p \rightarrow \Lambda\bar{\Lambda} \rightarrow p\bar{p}\pi^+\pi^-$ hyperon channel has been investigated by the PS185 experiment at LEAR antiproton facility from threshold production (1.436 GeV/c) up to 2 GeV/c [6], which was the maximum momentum of the LEAR experimental facility. The high statistics data samples from PS185 comprises 40k completely reconstructed $\bar{p}p \rightarrow \Lambda\bar{\Lambda} \rightarrow p\bar{p}\pi^+\pi^-$ events [7]. The data above 2 GeV/c are governed by low statistics data of bubble chamber experiments and no data are available above 7 GeV/c. Corresponding bubble chamber experiments have, at most, a few hundred complete events [8]. There is another experiment at 6 GeV/c with comparable statistics to PS185 [9], but normally only one hyperon could be reconstructed from the events. Therefore it was not possible to do spin correlation study. Total experimentally measured cross section for the $\bar{p}p \rightarrow Y\bar{Y}$ hyperon reaction channels are summarised in Figure 1.6 .

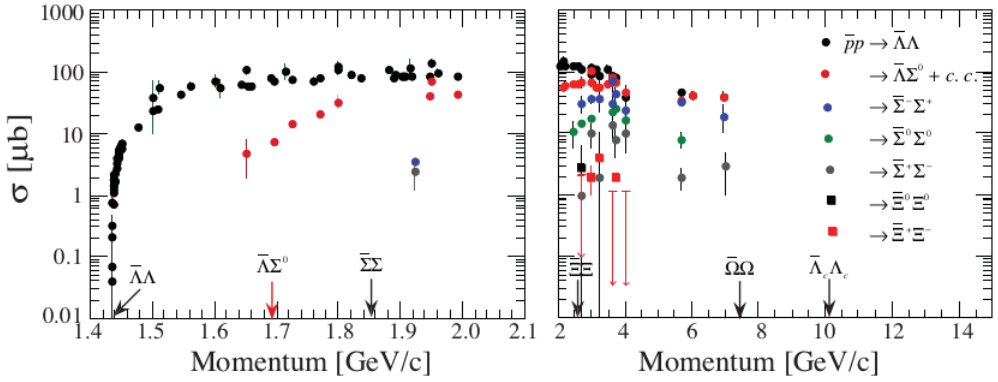

Figure 1.6: Total cross sections for the $\bar{p}p \to \bar{Y}Y$ reaction in the momentum range of the HESR. Figure is adopted from Ref. [5].

1.5 Hyperon Physics in $\overline{\text{P}}$ANDA

All strange hyperons, as well as single charmed hyperons are energetically accessible in $\bar{p}p$ collisions at HESR. A systematic investigation of these reactions will bring new information on single and multiple strangeness production and its dependence on spin observables. This is particularly essential above 2 GeV/c, where practically nothing is known about the differential distributions and spin observables. The large amount of observables accessible and high statistics $\overline{\text{P}}$ANDA data will allow to complete that. Thus it will be possible to study relevant quantum numbers, coupling constants and possibly find new resonances.

Hyperons decay through weak interaction. So, they have longer lifetime and consequently a larger displacement of the secondary vertex and decay exhibit an angular asymmetry due to parity non-conserving nature of this reaction. This angular asymmetry enables the polarizations of the hyperons in the final state and their spin correlations can be determined. These spin observables, along with the differential cross-sections, constitute a complete data set that sheds light on the strength, range and spin dynamics of the strong interaction [5].

CP violation of hyperon could be another study in $\overline{\text{P}}$ANDA. CP violation can answer the matter-antimatter mystery of the universe. Angular distribution of the hyperon decay products can be studied as an observable

of CP violation. However, this study is only feasible with very high beam luminosity and this is not possible at the initial phase of experiment. Experimentally CP violation in mesons are already measured, however, there are no data available for baryon, specially for hyperons [10].

1.5.1 Concept of Lambda Disks Detector

It is very important to increase the reconstruction efficiency of Λ and $\bar{\Lambda}$ particles to include different studies related to hyperon physics in $\overline{\text{P}}$ANDA. Study and reconstruction capability of other hyperon pairs are also dependent on the reconstruction efficiency of Lambda hyperon as other hyperons also decay through Lambda hyperons as shown in Table 1.1. Hence, a detailed understanding of the reconstruction and identification of Λ or $\bar{\Lambda}$ particles in $\overline{\text{P}}$ANDA detector is very important for many aspects of the $\overline{\text{P}}$ANDA physics programme. The reconstruction of the Λ decay products (mostly from $\Lambda \to p\pi^+$ and $\bar{\Lambda} \to p\pi$) differs from ordinary charged particle reconstruction in $\overline{\text{P}}$ANDA as the charged particles do not come from the interaction point.

We have introduced two layers of double sided silicon strip sensors as Lambda Disks Detector in a large detector free volume between MVD (Micro Vertex Detector) and GEM (Gas Electron Multipliers) to increase the reconstruction efficiency of Λ and $\bar{\Lambda}$. One can understand that the implementation of Lambda Disks detector can enrich the hyperon physics. Cross-section of $\Lambda\bar{\Lambda}$ below 2 GeV/c which is published by PS185 will be confirmed, we can expect data with high statistics between 2 to 7 GeV/c and also $\overline{\text{P}}$ANDA has the opportunity to provide first data above 7 GeV/c. Therefore, in this thesis we have done different studies to explore the possibilities of including the Lambda Disks Detector in $\overline{\text{P}}$ANDA experiment.

Chapter 2

Experimental Facility

In this chapter, we discuss the Facility for Antiproton and Ion Research (FAIR), the upcoming international research facility at Darmstadt, Germany to answer the fundamental questions like, evolution of the universe, structure of matter and its building blocks. In particular, the antiProton ANnihilations at DArmstadt ($\overline{\text{P}}$ANDA) with various detector systems is discussed which are used for the simulation studies of Lambda Disks Detector.

2.1 The Facility For Antiproton and Ion Research

The **F**acility for **A**ntiproton and **I**on **R**esearch (FAIR) is a new international facility for the research with the antiproton and ions. It is an upgradation to the existing GSI experimental facility to investigate the answers of many fundamental questions in hadron physics which are basically unanswered till now. A schematic view of FAIR complex in GSI is shown in Figure 2.1. The existing GSI facility contains the **UNI**versal **L**inear **AC**celerator (UNILAC), the **E**xperimental **S**torage **R**ing (ESR) and the heavy ion synchrotron (SIS18). The upgraded GSI facility with a new proton Linear Accelerator (p-LINAC) will serve as pre-accelerator and injector for two main accelerators of FAIR, which are SIS100 and SIS300. SIS100 is fast cycled synchrotron of 100 Tm maximum bending power and 1080 m circumference, which is five times the circumference of existing SIS18. SIS300 is another fast synchrotron surroundings to SIS100 with the circumference of 1100m. The existing SIS18 with the new proton linac as

injector will be used to boost the proton energy to 2 GeV for the injection into the sychrotron SIS100. The synchrotron SIS100 is used to accelerate protons to the antiproton production energy of 29 GeV. The accelerated protons, with an energy of 29 GeV, will produce antiprotons in inelastic collision with the target nucleus, which is made of either nickel, iridium or copper. Approximately, a bunch of protons containing 2.5×10^{13} primary protons are expected to produce 1×10^{8} antiprotons within the phase space acceptance of further separator or Collector Ring (CR). The produced antiprotons are then transferred for the precooling in the Collector Ring and then cooled antiprotons will be transferred to accumulate to Recycled Experimental Storage Ring (RESR), which will come only later while experiment is operated with very high luminosity. Then they are injected to the **H**igh **E**nergy **S**torage **R**ing (HESR), where the $\overline{\text{P}}$ANDA experiment will be located [11]. SIS300 will deliver high energy ion beams for studies related to ultra-relativistic heavy ion collisions.

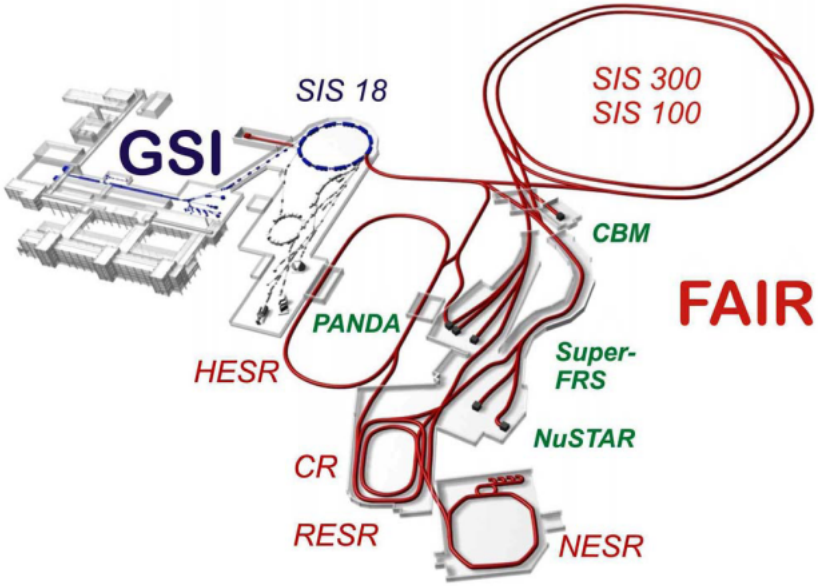

Figure 2.1: Schematic overview of FAIR Complex with the GSI facility [12].

The accelerators of FAIR will have specific feature over the existing facilities:

- Beam intensity increased by a factor of 100 to 1000 for primary and 10000 for secondary beams

- Beam energy will increase by a factor 30 for heavy ions
- Beam variety offered by FAIR will have a variety of beam lines, from antiprotons to protons, to uranium and radioactive ions
- Availability of cooled antiproton and ion beams will improve the beam precision
- Full accelerator will perform parallel operation for up to four different, independent experiments and experimental programs

These features of FAIR will make it a first rate facility for experiments in particle, nuclear, atomic, plasma and applied physics [13].

2.1.1 High Energy Storage Ring

The High Energy Storage Ring (HESR) is dedicated to supply the $\overline{\text{P}}$ANDA experiment with high quality antiproton beams in a momentum range from 1.5 GeV/c to 15 GeV/c. The $\overline{\text{P}}$ANDA will be placed inside the HESR as shown in the Figure 2.2. The 3 GeV antiprotons produced at the production target are fed to the High Energy Storage Ring, which act both as a storage ring and as an accelerator. The HESR prepares the final beam used for $\overline{\text{P}}$ANDA with momenta between 1.5 GeV/c and 15 GeV/c depending on the physics requirements. HESR can be operated in two modes:

In high luminosity Mode, the highest luminosity of $2{\times}10^{32}$ $\text{cm}^{-2}\text{s}^{-1}$ can be achieved with the antiproton of 15 GeV/c and a beam momentum resolution of $\delta p/p \sim 10^{-4}$ [14].

In high resolution mode, the highest luminosity of $2{\times}10^{31}$ $\text{cm}^{-2}\text{s}^{-1}$ can be achieved with the antiproton beam of 9 GeV/c and a beam momentum spread is nearly $\delta p/p \sim 10^{-5}$ [14].

2.1.2 Experimental Programs

The FAIR facility conducted several physics programs in parallel, covering four major scientific fields [16]. These are called four pillars of FAIR facility and named as:

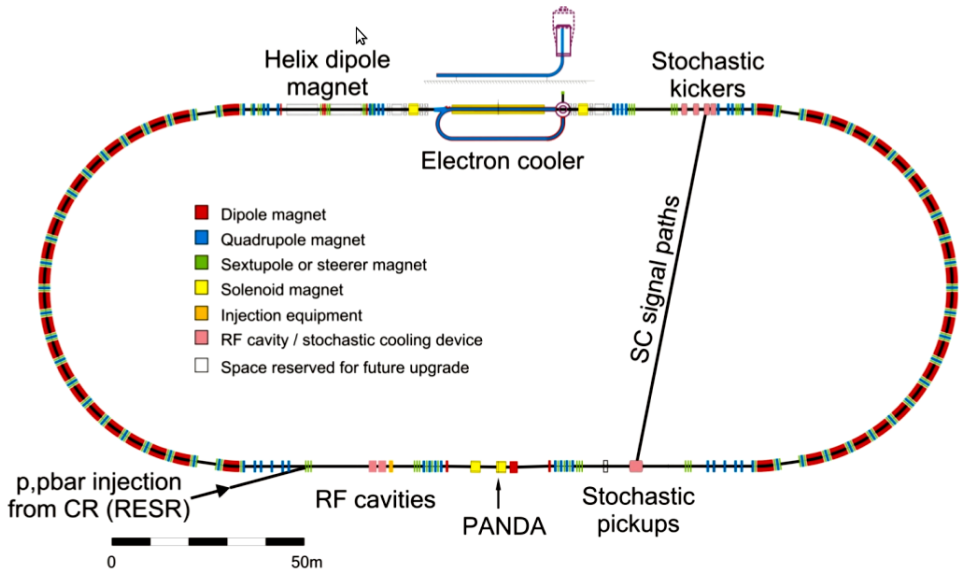

Figure 2.2: Schematic view of the HESR. Positions for injection, cooling devices and experimental installations are indicated. Figure is adopted from Ref. [15].

- Atomic, Plasma Physics and Applications (APPA)
- Compressed Baryonic Matter (CBM)
- NUclear STructure, Astrophysics and Reactions (NUSTAR)
- antiProton ANnnihilations at DArmstadt ($\overline{\text{P}}$ANDA)

2.1.2.1 APPA

Atomic and Plasma Physics, and Application is an umbrella organization, consisting of five independent research collaborations. It represents one of the four FAIR research pillars and comprises three research communities: biophysics and material science (BIOMAT), atomic physics (SPARC, FLAIR) and plasma physics (HEDgeHOB, WDM) [17].

BIOMAT The biophysics research has two main topics: space radiation effects on humans (astronauts) and spacecraft instrumentation (microelectronics); and particle therapy using high-energy protons and heavy ions for cancer and noncancer diseases. Research in material science is dedicated to heavy-ion induced modifications in solids under extreme conditions such

as short ion pulses, high fluences, and the simultaneous application of pressure and temperature. A multipurpose irradiation facility will be built and exploited by the BIOMAT collaboration consisting of international collaborations on heavy-ion biophysics (BIO) and material science (MAT).

SPARC The Stored Particle Atomic Physics Research Collaboration deals with the atomic physics with highly charged ions. The main focus is the investigation of the physics at strong, ultra-short electromagnetic fields including the fundamental interactions between electrons and heavy nuclei as well as on the experiments at the border between nuclear and atomic physics.

FLAIR The Facility for Low Energy Antiproton and Ion Research will direct its efforts towards the atomic and nuclear physics studies with low-energy antiprotons. The ultimate aim of the facility is the testing of the Charge Parity Time reversal(CPT) invariance and Quantum Electrodynamics (QED), atomic collisions and medical research as tumor therapy.

HEDgeHOB The High Energy Density Matter generated by Intense Heavy iOn Beams collaboration aims to study the physics of dense plasmas with highly compressed heavy-ion beam bunches in combination with a high-power laser will concentrate on studies of the phase diagram in the regime of strongly coupled plasma.

WDM The Warm Dense Matter collaboration studies the radiative properties of warm dense matter produced by intense heavy ion beams. Warm Dense Matter (WDM) refers to high-density finite-temperature regime where free and bound electrons become strongly correlated. It occurs when condensed matter reaches temperatures near and above the Fermi temperature.

2.1.2.2 CBM

The Compressed Baryonic Matter (CBM) experiment will be another major experiment at future FAIR facility in Darmstadt. It is a fix target experiment and the goal of the CBM scientific program is to investigate the QCD phase diagram in the region of high baryon densities using high-energy nucleus-nucleus collisions. The CBM experiment will try to find the answer of some basic questions like the search for the deconfinement and chiral phase transitions, possible location of critical point in QCD phase diagram [18].

2.1.2.3 NUSTAR

The NUSTAR stands for NUclear STructure, Astrophysics and Reactions. The NUSTAR collaboration will use the new accelerator facilities at FAIR for basic science with focus on the structure of atomic nuclei, nuclear astrophysics, and nuclear reactions. The NUSTAR is a set of several experiments experiments belonging different physics and focused on the use of beams of radioactive species separated and identified by the Superconducting FRagment Separator (Super-FRS), which is the central element of all NUSTAR experiments [19].

2.1.2.4 $\overline{\text{P}}$ANDA

The name $\overline{\text{P}}$ANDA itself is an acronym which stands for antiProton ANnihilations at DArmstadt. $\overline{\text{P}}$ANDA is a fix target experiment and one of the four major scientific pillars of FAIR at which the physics with antiprotons will be introduced. Antiprotons of beam momentum 1.5 GeV/c to 15 GeV/c hits with a fixed proton target to enable the various physics aspects at $\overline{\text{P}}$ANDA [20]. The detailed description of $\overline{\text{P}}$ANDA experiment along with the physics programs are given in next section.

2.2 The $\overline{\text{P}}$ANDA Experiment

The $\overline{\text{P}}$ANDA experiment is one of the key projects of the FAIR facility which is planned as part of the future FAIR facility at Darmstadt. The cooled antiproton beam with a momentum between 1.5 GeV/c and 15 GeV/c will be provided for the $\overline{\text{P}}$ANDA experiment in HESR. The $\overline{\text{P}}$ANDA experiment is divided in two parts, one is Target Spectrometer (TS) based on a superconducting solenoid magnet surrounding the interaction point and another is Forward Spectrometer (FS) based on a dipole magnets in order to achieve good momentum resolution. The $\overline{\text{P}}$ANDA detector setup is shown in Figure 2.3.

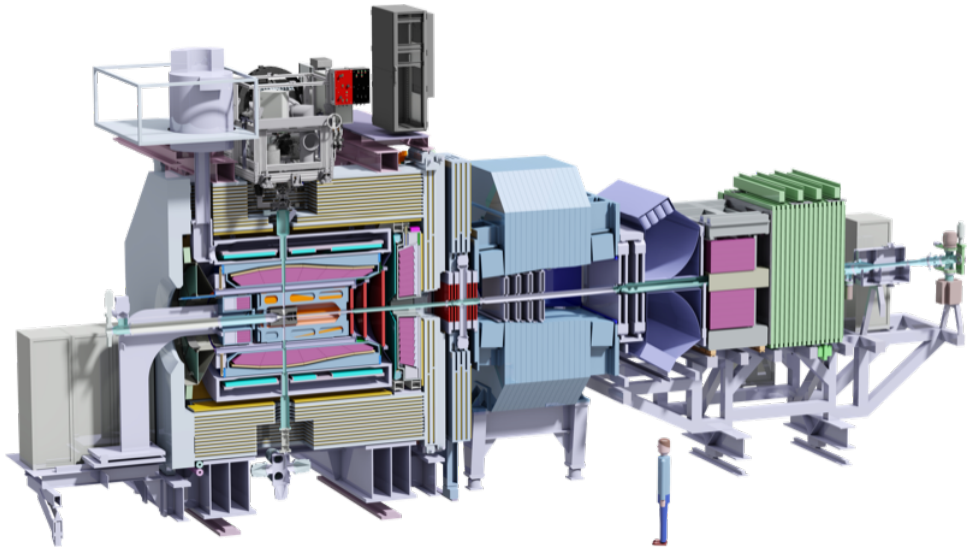

Figure 2.3: The $\overline{\text{P}}$ANDA detector setup [21].

2.2.1 Target Spectrometer

The Target Spectrometer (TS) surrounds the interaction point with the onion shell like shape of different sub-detectors. The target spectrometer consists of superconducting solenoidal magnet. It has a length of 2.5 m, a diameter of 1.9 m and an axial field of 2 T. The beam is directed through a narrow and thin pipe which intersects with a vertical pipe required for the injection of the target material. The target pipe crosses the whole spectrometer from top to bottom. The target spectrometer is made up of

the following components, which are shown in Figure 2.4.

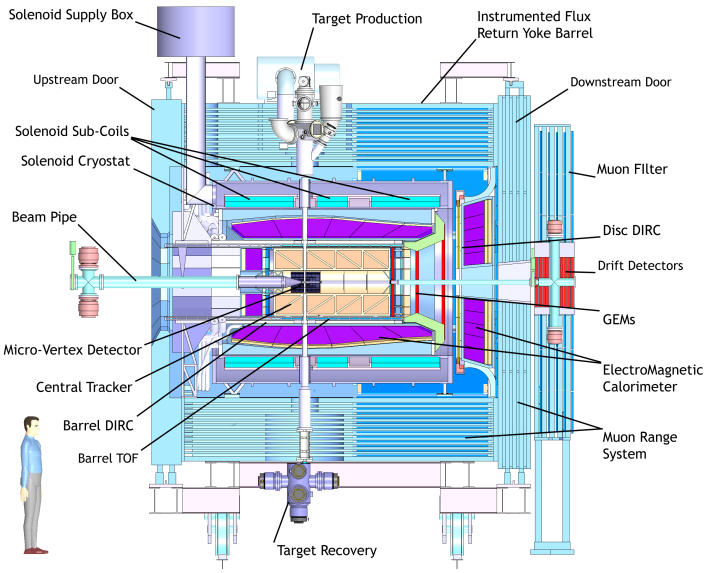

Figure 2.4: The Target Spectrometer of the $\overline{\text{P}}$ANDA detector [23].

2.2.1.1 Targets

Cluster-Jet target: Two types of targets are developed for the target of $\overline{\text{P}}$ANDA. A Cluster-Jet target is realized through the expansion of pre-cooled gas passing through nozzle with micron sized throat into vacuum. A supersonic stream of atoms or molecules are created while gas passing through the nozzle and the gas adiabatically cools down. The condensation of gas can take place under appropriate conditions, depending on the type of gas, which is shaped as nano-particles. These nano particles are called clusters. Cluster beams can travel over several meters of distance in vacuum without disturbance of the direction and have high densities [22].

Pellet target: Another solution is the Pellet Target, which is made up of a stream of frozen hydrogen micro-spheres which are crossing by the antiproton beam. This method has been already used in the WASA experiment at COSY. The lateral spread of the flow of spheres is of about 1 mm and each sphere is separated from the others by a distance of 0.5-5.0 mm. The development of this kind of target is now focused on the minimization of the variations of the luminosity. With this configuration a single sphere is

a target for many interaction until it has crossed the antiproton beam [22].

2.2.1.2 Solenoid Magnet

The magnetic field in the target spectrometer will be provided by a superconducting solenoid coil with an inner radius of 105 cm and a length of 2.8 m. The maximum magnetic field needs to be 2 T. In the conceptual design, superconducting solenoid with external iron return yoke has been chosen which allows to achieve a longitudinal field of 2 T and keeps enough space for the detectors surrounding the interaction point. All barrel detectors, except the muon chambers, will be hosted inside the warm bore of the solenoid cryostat. An overview of the solenoid with all the detectors is shown in Figure 2.5.

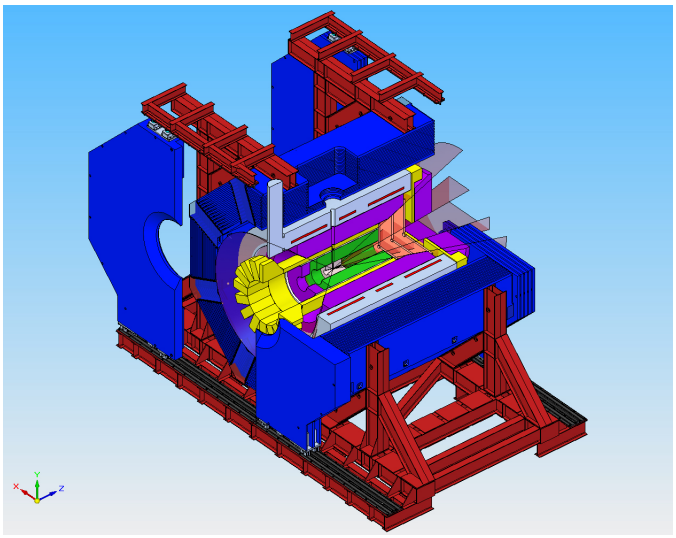

Figure 2.5: Overview of the Target Spectrometer showing the solenoid magnets. One quarter is cut on this view showing the cryostat, coil, and inner detectors [23].

2.2.1.3 Tracking Detectors

Particles produced in collisions normally travel in straight lines, but in the presence of a magnetic field their paths become curved. Tracking detectors reveal the paths of electrically charged particles as they pass through and interact with detector material. A short introduction of $\overline{\text{P}}$ANDA tracking detectors is presented here.

Micro Vertex Detector (MVD): This is the innermost detector of $\overline{\text{P}}$ANDA and it is placed close to the interaction point inside the target spectrometer. Its main purpose is high precision charged particle tracking and particle identification based on the energy loss in the detector material. The CAD geometry view is shown in Figure 2.6.

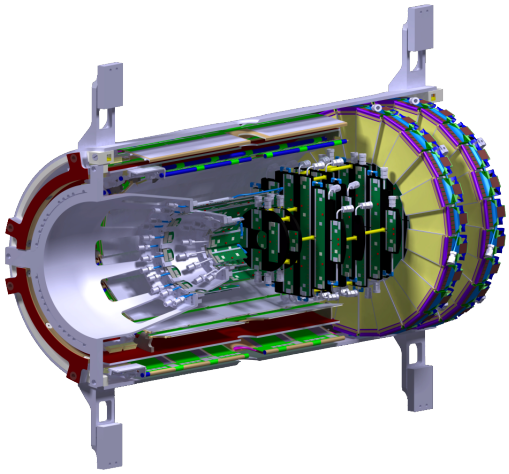

Figure 2.6: The Micro Vertex Detector (MVD) of the Target Spectrometer surrounding the beam and target pipes as seen from downstream [24].

The MVD delivers 3D hit information close to interaction point which is important to determine origin of particle tracks and to improve the momentum resolution. Also, MVD has the capability to reconstruct secondary decays of short lived particles in displaced vertices other then the primary reaction point. Since this is the innermost detector the flux of particles will be maximum, therefore the detector is designed to deal with high rates and to have the necessary radiation hardness. The detector will be equipped with both silicon pixel and silicon strip sensors. It consists of silicon sensors in four barrel layers and six forward disks. The outer radius of the MVD is kept to 15 cm due to limitation of space occupied by the surrounding detector. Its extent along the beam axis is about $\pm$ 23 cm with respect to the interaction point. The inner two barrel layers will use silicon pixel sensors while the outer two barrel layers will use double sided silicon strip sensors [24].

Lambda Disks Detector (LDD): Lambda disks are the two additional disks to MVD. As a starting geometry of Lambda disks, these are fully made of double sided silicon strip sensor. In the basic design, the outer ring has been kept similar to the outermost layers of MVD forward disks and inner layer has been designed using silicon strip sensors. The LDD detector is an additional detector next to MVD to improve the reconstruction of delayed decay vertices of particles which are having longer decay lengths. The detailed description of Lambda Disks Detector is given in next chapter.

Straw Tube Tracker (STT): The Straw Tube Tracker is the central tracker of the experiment and will consist of aluminized mylar tubes called straws .The straw tubes are to be arranged in planar layers which are mounted in a hexagonal shape around the MVD as shown in Figure 2.7 . The gas used to fill the tubes of the STT will be a mixture of Ar and CO_2,

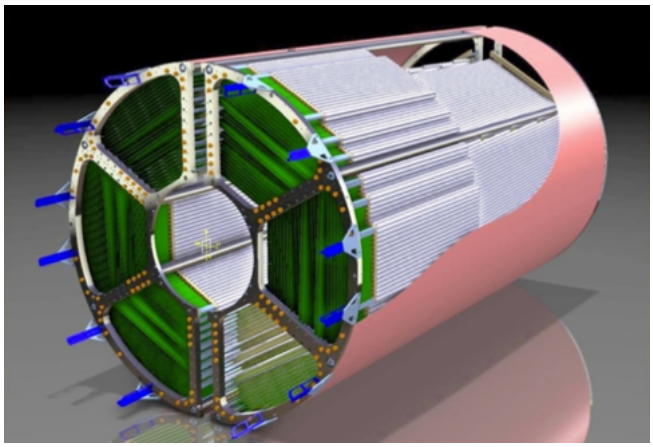

Figure 2.7: The Straw Tracker Tube of the Target Spectrometer [25].

where CO_2 works as a quencher. The STT consists of 27 layers of 150 cm long tubes. Most of the layers are parallel to the beam axis while 8 skew layers are positioned with a stereo angle of $\pm\ 2.9^0$ with respect to the other tubes. In total 4636 straw tubes are assembled to build the STT. All straw tubes have a diameter of 10 mm and made of a 27 cm thick Mylar foil. Each straw tube is formed with a single anode wire in the center which is made of 20μm thick gold plated tungsten. The drift time in each tube allows to measure a radial distance from the anodic wire. This results in

a position resolution in the transverse plane (xy plane) better than 150 μm. The longitudinal coordinate parallel to z axis is determined matching the hits measured by the skew layers. This allows to reach a longitudinal position resolution of about 3 mm [25].

Gas Electron Multipliers (GEMs): Gas Electron Multipliers detector is consisting three disks as shown in Figure 2.8 and these will be positioned respectively 1.1, 1.4 and 1.9 m downstream from the interaction point to cover polar angles below 22^0 [24]. A disk consists of two planes, each of them foreseeing two projections. Each disk will then have four projections, which allow to resolve ambiguities when several hits are measured on one plane. All the three disks have an internal radius of 2.5 cm, while the external radii grow proceeding along the beam axis. The first disk has an external radius of 45 cm, the second one is 56 cm and the last one is 74 cm.

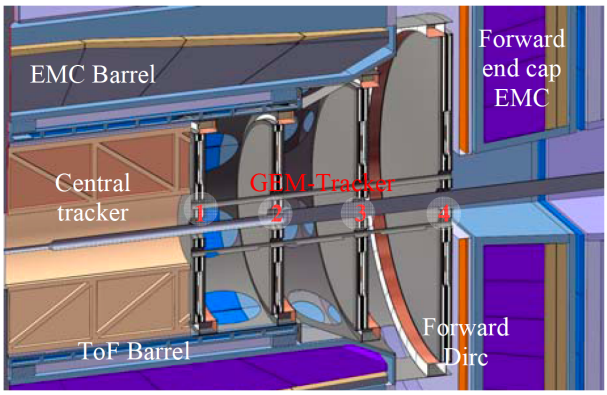

Figure 2.8: The Gas Electron Multiplier of the Target Spectrometer [26].

2.2.1.4 Particle Identification Detectors

Cherenkov Detector: Particle identification (PID) detectors use a range of techniques to find a particle's identity. When a charged particle travels faster than light through a given medium, it emits cherenkov radiation at an angle that depends on its velocity. The particle's velocity can be calculated from this angle. Velocity can then be combined with a measure of the particles momentum to determine its mass, and therefore its identity. $\overline{\text{P}}$ANDA have DIRC and TOF as a cherenkov detectors in target spectrom-

eter are listed here as a PID detectors.

Detector for Internally Reflected Cherenkov (DIRC): Charged particles in a medium with refractive index n, propagating with velocity $\beta = v/c > 1/n$ emit radiation at an angle $\cos(\theta_c) = 1/\mathrm{n}(\omega)\ \beta$. Thus, the mass of the detected particle can be determined by combining the velocity information determined from θ_c with the momentum information from the tracking detector. Due to the strong variation of the typical particle momentum with polar angle, particle identification is achieved using two systems of cherenkov detectors in the target spectrometer. DIRC detector will be used at two different positions within the the target spectrometer. A barrel shaped DIRC surrounds STT and will cover the polar angle range from 22^0 to 140^0. A disk DIRC in forward direction covers a polar angle range from 5^0 to 22^0 in vertical direction [29].

Time of Flight Detector (TOF): If the particle travels the distance (d) to reach to the detector, then time (t) taken by the particle is given as;

$$t = \frac{d}{v} = \frac{dc}{\beta}$$

where β is velocity of particle. Since momentum of particle is given by $p = mv = m_0\beta vc$, where m_0 is rest mass of the particle. If we know momentum and time of flight then we can perform particle identification. For the PID of slow charged particle, a TOF detector is placed in the target spectrometer. The TOF barrel allow the detection probability for $\bar{\Xi}$ by a factor up to 1000 by detecting slow kaon decay products [28].

A scintillator tile barrel will be placed just outside the barrel DIRC volume, and will be used for the PID of slow particles emitted at large polar angles. This detector will consist of 5,760 scintillator tiles, each with a size of $28.5 \times 28.5mm^2$. All tiles will be read out individually by two silicon photo-multipliers per tile. It will provide a fast signal with a time resolution of about 100 ps [29].

Electro Magnetic Calorimeters (EMC): A calorimeter measures the particle energy loses as it passing through. It is used to stop or absorb most of the particles, forcing them to deposit their energy within the detector. The electromagnetic calorimeters (EMC) will be used at $\overline{\text{P}}$ANDA to measure neutral particles and leptons. The EMC can also complete the particle identification information provided by the DIRC and the TOF detectors. This contribution will be especially powerful in distinguishing electrons from charged pions. The EMC is composed of three parts and shown in Figure 2.9.

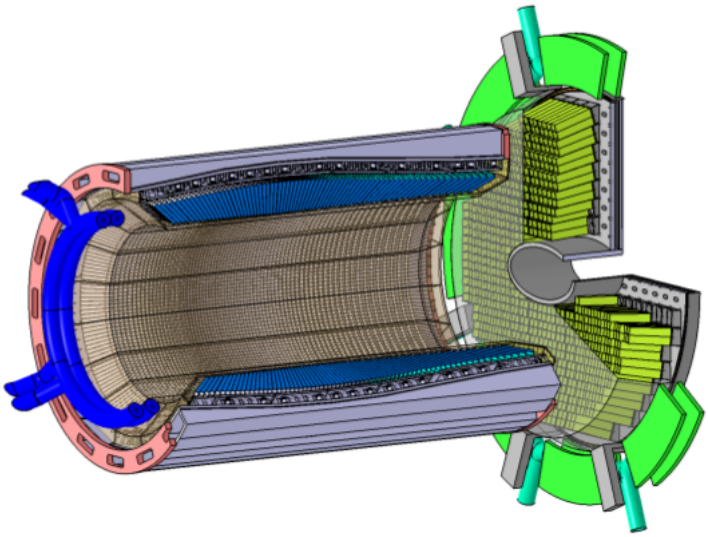

Figure 2.9: The Electro Magnetic Calorimeter of the Target Spectrometer [27].

The barrel calorimeter which covers the region around the TOF tiles with an inner radius of 57 cm. It consists of 11360 crystal read outs with radiation hard avalanche photo diodes. The forward end cap is composed of 3600 crystals, which are read out with vacuum photo-triodes. Both for the barrel and for the forward end cap tapered crystals will be used. The position and the direction of each crystal have been optimized in order to point toward the region around the primary vertex, where most of the particles will come from. In order to cover large polar angle up to 170^0 a backward end cap consisting of 592 parallelepiped crystals will be positioned upstream from the end of the barrel calorimeter [27].

Muon Detectors (MDT): The muon detector is the most external detector of the target spectrometer. It makes use of Mini Drift Tubes (MDT), which are drift tubes with a central anodic wire. The detector is composed of two main parts: the barrel and the forward end cap. A bi-layer composed of two consecutive detector planes is positioned before the first yoke layer. It is aimed to help the back propagation of muon tracks toward the primary interaction point and to facilitate the overall muon tracking. Downstream from the end cap a muon filter is positioned, which is mechanically identical to the end cap. The filter has a dual purpose: it improves the detection of muons at intermediate angles since it increases the thickness of the available absorbers and at the same time it shields the solenoidal magnetic field allowing a better separation between the target and the forward spectrometers [30].

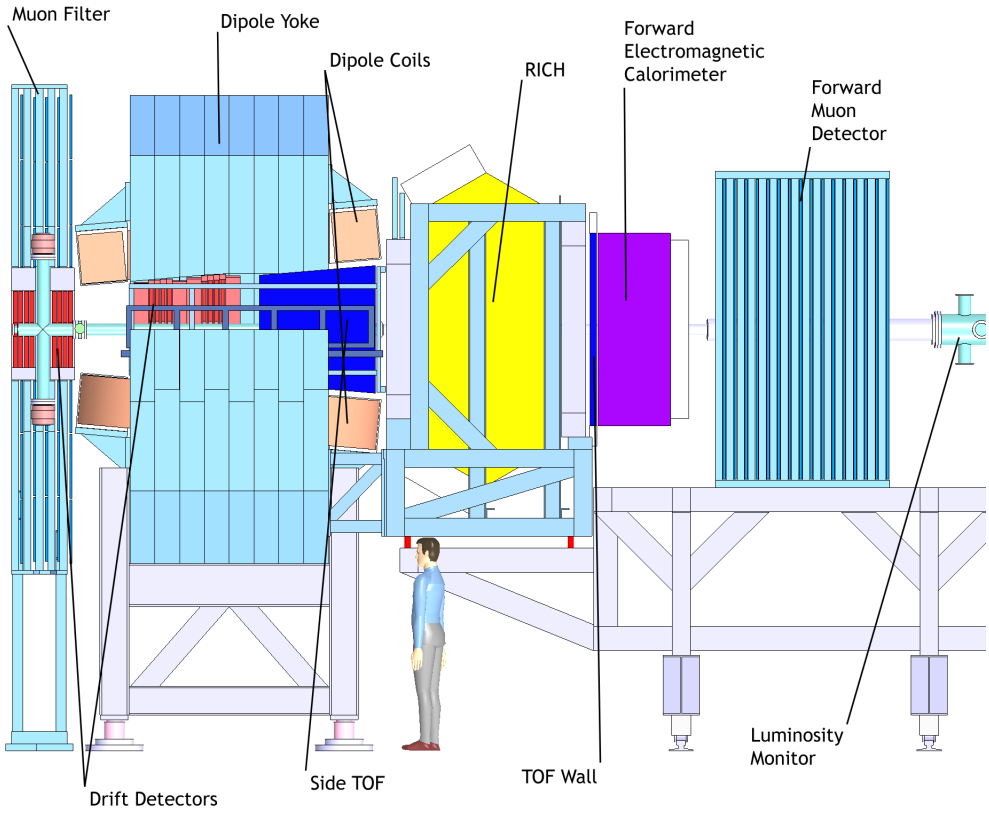

Figure 2.10: The Forward Spectrometer of $\overline{\text{P}}$ANDA detector [29].

2.2.2 Forward Spectrometer

The Forward Spectrometer (FS) shown in Figure 2.10 will be used to measure particles with polar angles below 5^0 in the vertical direction and 10^0 in the horizontal plane. Both charged and neutral particles will be measured with trackers, a calorimeter, muon detectors and detectors suited for particle identification [29].

Dipole Magnet: The forward spectrometer is based on the dipole magnet which will allow to analyze high momentum charged particles. This magnet will provide a 2 Tm bending power which corresponds to a deflection of approximately 2^0 for the 15 GeV/c beam which will be compensated by magnets positioned downstream. A longer dipole would be easier to build and cheaper to run, but the angular acceptance of the following detectors would be sensibly reduced with increasing distances. On the other side a short dipole with such a wide transverse opening would require intense fields. The current design of dipole is 2.5 m long in the beam direction started from 3.5 m downstream.

Forward Tracking System (FTS): The FTS will consist of six tracking stations. Two placed before the magnet, two within the magnet and two behind the magnet. This arrangement will allow to track particles with highest momenta as well as low momentum particles. Each station will contain four double layers of straw tubes of which two will be oriented vertically and the other two double layers will be rotated by $\pm 5^0$ with respect to the vertical straw tubes [5].

Ring Imaging CHerenkov detector (RICH): The RICH will measure the Cherenkov light cone directly without internal reflection. The RICH will have two radiators of different refractive indices, silica aerogel and C_4F_{10} gas. A lightweight mirror will focus the cherenkov light on an array of photo-tubes placed outside the active volume. To enable the π/K

and K/p separation also at the very high momentum a RICH is proposed for $\overline{\text{P}}$ANDA forward spectrometer [5].

Forward TOF: A slabs made of plastic scintillator and read out on both side ends will serve as Time of Flight stop counter placed at about 7m from the target. The relative time of flight between two charged tracks reaching to this TOF and another similar detector placed inside dipole magnet will be measured in the experiment [5].

Forward EMC: A Shashlyk-type calorimeter with high resolution and efficiency will be employed to detect the photons and electron in the Forward spectrometer.The detection is based on lead-scintillator sandwiches read out with wavelength shifting fibres passing through the block and coupled to photo-multipliers [5].

Forward Muon Detectors: To enable the muon measurements in very forward part, a further tracking system consisting absorber layers and rectangular drift tubes is designed. Froward muon detector will allow to discriminate of pions to muons [5].

Luminosity Detector: The luminosity at $\overline{\text{P}}$ANDA is determine by the elastic scattering of the antiproton beam with the protons of the target. Due to the presence of the beam pipe and strong solenoidal magnetic filed it is not possible to measure the soft recoiling protons at polar angles close to 90^0 . It is anyway sufficient to measure the elastic scattering in the region of interference between the coulombian and the nuclear contribution in order to deduce the absolute luminosity. This can be done at $\overline{\text{P}}$ANDA measuring at the end of the spectrometer the high momentum antiprotons which undergo a small angle elastic scattering. The luminosity detector will be therefore positioned in the most forward part of the $\overline{\text{P}}$ANDA experiment at 10 m from the interaction point. Four sensor planes will be placed in vacuum to minimize the effect of multiple scattering on the antiprotons

before they reach the luminosity detector [5].

2.2.3 Data Acquisition (DAQ):

In $\overline{\text{P}}$ANDA, a data acquisition concept is being developed and will follow a novel scheme for acquisition and processing of detector data. A subset of specially instrumented detectors is used to evaluate a first level trigger condition. For the accepted events, the full information of all detectors is then transported to the next higher trigger level or to storage. The available time for the first level decision is usually limited by the buffering capabilities of the front-end electronics. Furthermore, the hard-wired detector connectivity severely constrains both the complexity and the flexibility of the possible trigger schemes [5].

Chapter 3

Lambda Disks Detector

This chapter gives the detailed description of Lambda Disks Detector. The Lambda Disks Detector (LDD) consists of two disks forward to innermost sub-detector Micro Vertex Detector (MVD) and it is seen as an upgrade option to the existing $\overline{\text{P}}$ANDA setup. It is located at distance of 40 cm and 60 cm in the forward direction from the interaction point for the studies belonging to this thesis. In the following sections, the main aspects of LDD are highlighted. Also, the basic detector layout and conceptual design are summarized. Further, the radiation length studies are included which are made to optimize material budget for the Lambda Disks. Finally, efforts are discussed towards the mechanical design of this detector and estimation of its components.

3.1 Detector Tasks and Requirements

The main task of the Lambda Disks Detector is the measurement of secondary decay vertices of long lived particles. These particles with delayed vertex are mesons and hyperons with charm and strange quark content. A better track reconstruction is required to identify Λ hyperons through their delayed decay vertex. Four track points are needed to have a good reconstruction of a track. Particles with a large decay length are traveling outside the Micro Vertex Detector (MVD), which surrounds the interaction region and due to unavailability of tracking detector forward to MVD, these particles do not register required number of track points. Therefore, two additional forward disks are considered to obtain at least four track points.

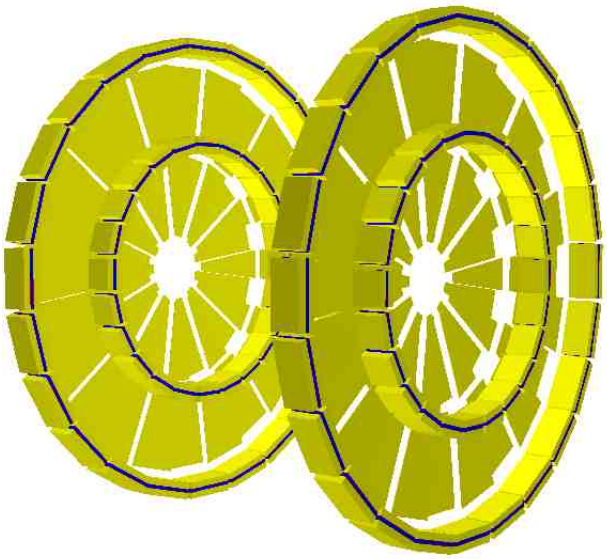

Figure 3.1: A picture of the two additional Lambda Disks.

A minimization of the required material for LDD is very important because a very high material load would affect all backward and forward detector components. Detection of low momentum particles is necessary for $\overline{\text{P}}$ANDA physics program. These small momentum particles may loose their energy due to scattering by interacting with this material.

Another requirement is the radiation hardness of the detector. All the components of detector must bear with sufficient radiation dose. The requested radiation tolerance in terms of the expected total ionizing dose (TID) is in the order of 10^{14} n_{eq} cm^{-2} assuming a 50% duty cycle in the 10 years lifetime of $\overline{\text{P}}$ANDA [32]. However, this study is not included in this thesis.

3.2 Basic Detector Layout

The Lambda Disks Detector contains two disks as these are shown in Figure 3.1. The lower and upper limits for this detector positions are defined between z = 23 cm to 110 cm along the beam axis utilizing the gap until the forward GEM tracking station started from MVD. The maximum ra-

dius of disk is kept 15 cm which is same as last two MVD disk layers. The schematic picture of LDD detector layers with MVD detector is shown in Figure 3.2. The conceptual design of these additional disks is similar to that of the strip disks used for the central MVD.

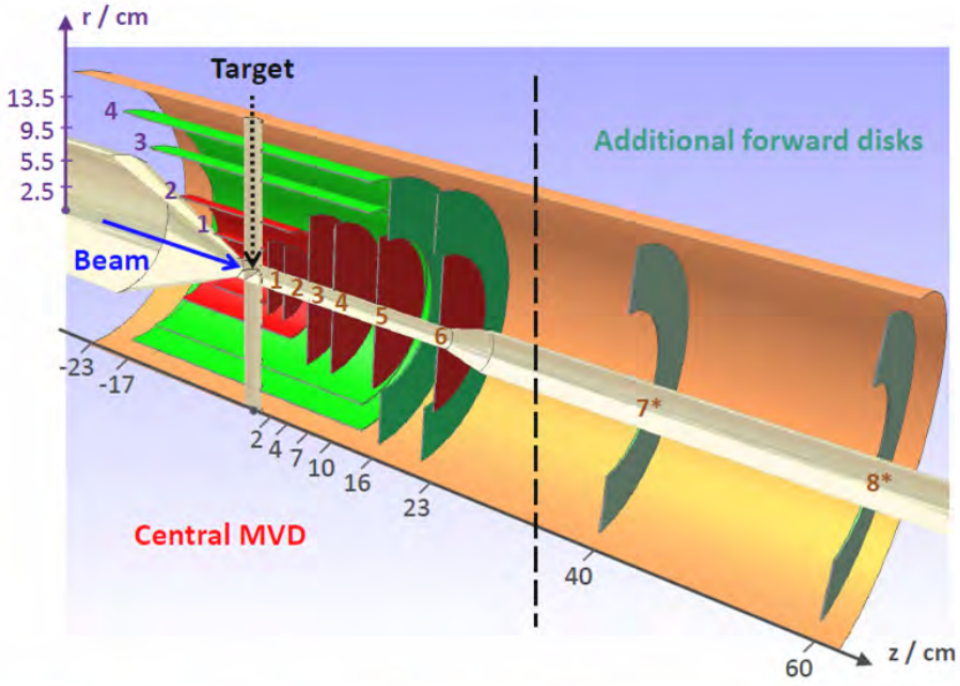

Figure 3.2: Basic layout of LDD as the two additional disks in the forward direction. The additional forward disks (labelled 7 and 8) are based on the conceptual design of the outer MVD strip disks. Figure is adopted from Ref. [31].

The MVD is innermost tracking detector of $\overline{\text{P}}$ANDA detector setup and in forward direction, it consists of six disk layers enabling a measurement at small polar angle between 3^0 to 40^0. First four are pixel disks and two outer most disks are made up of pixel as well as strip sensors. First two pixel disks are inside the outer pixel barrel layer and located at 2 cm and 4 cm close to interaction region. After two small pixel disks there are four disks layer in downstream direction. While the first two of them are positioned inside the strip barrel layers, the ones further downstream are extended by two mixed disks. Further to MVD disk layers, two additional disks named as LDD are placed which are purely made up of strip sensors. The solid angle coverage of LDD with the adjacent MVD is shown in Figure 3.3.

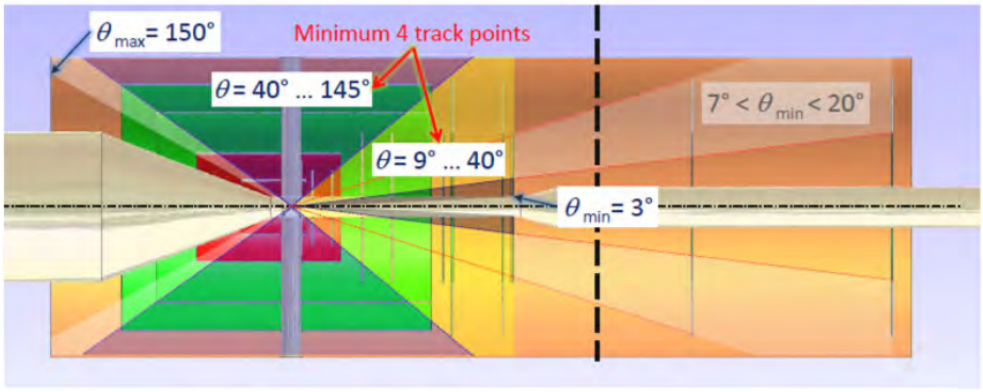

Figure 3.3: Diagram for solid angle coverage. The MVD covers polar angle (θ) from 3^0 to 150^0. Two additional LDD layers contribute to solid angle coverage from 3^0 to 20^0. Figure are taken from Ref. [31].

Lambda Disks Detector covers angular coverage between 3^0 to 20^0.

3.3 Conceptual Design

The conceptual design of the LDD is based on the silicon detector technology. Silicon detectors are known for their fast response and had an immense impact on the field of high energy physics. They can be produced in very big quantity and used to provide high particle tracking information. An introduction to silicon detectors with basic principles and applications are given in following subsections.

3.3.1 Silicon Sensors

A silicon detector is basically known as solid state ionization chamber and takes advantage of special electronic structure of semiconductor. The silicon detector is commonly used as an active element of vertex detection system in high energy physics. The properties of silicon can be determine by introducing impurities in it. In a pure semiconductor, the number of holes equals to number of electrons in conduction band. This balance of holes and electrons can be changed by introducing a small amount of impurity atoms having one more or one less electron in their outer atomic shell. It is in practice to use impurities and control them by doping. If

impurity is pentavalent, then there will be an extra electron in the crystal. Thus, semiconductor in which electrons are majority charge carriers are called n-type semiconductor. If impurity is trivalent with one less valence electron, there will not be enough electron to fill valence band. Then there is an excess of hole in the crystal and semiconductors are called p-type semiconductors. Both the case are shown in Figure 3.4.

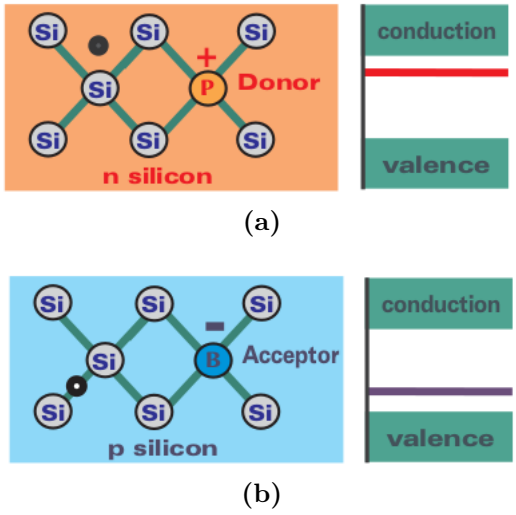

Figure 3.4: An illustration of n-type and p-type semiconductors are shown in panels (a) and (b) respectively. Figure is adopted from Ref. [33]

3.3.1.1 p-n junction

p-n junction is formed by contacting n-type and p-type semiconductor material. The n-type region has a high electron concentration and the p-type a high hole concentration, so electrons diffuse from the n-type side to the p-type side. Similarly, holes flow by diffusion from the p-type side to the n-type side. This diffusion process will continue until the concentration of electrons and holes on the both sides are not same. When the electrons and holes move to the other side of the junction, they leave behind exposed charges on dopant atom. On the n-type side, positive ion are exposed. On the p-type side, negative ion are exposed. An electric field E forms between the positive ion in the n-type material and negative ion in the p-type material. This region is called the depletion region since the electric field sweeps free carriers out, hence the region is depleted of free carriers. A p-n junc-

tion with no external bias voltage represents an equilibrium between carrier generation, recombination, diffusion and drift in the presence of the electric field in the depletion region [34]. In reverse bias a voltage is applied across the device such that the electric field at the junction increases. The higher electric field in the depletion region decreases the probability that carriers can diffuse from one side of the junction to the other, hence the diffusion current decreases. As in forward bias, the drift current is limited by the number of minority carriers on either side of the p-n junction and is relatively unchanged by the increased electric field. p-n junction mechanism with forward and reverse bias are illustrated in Figure 3.5.

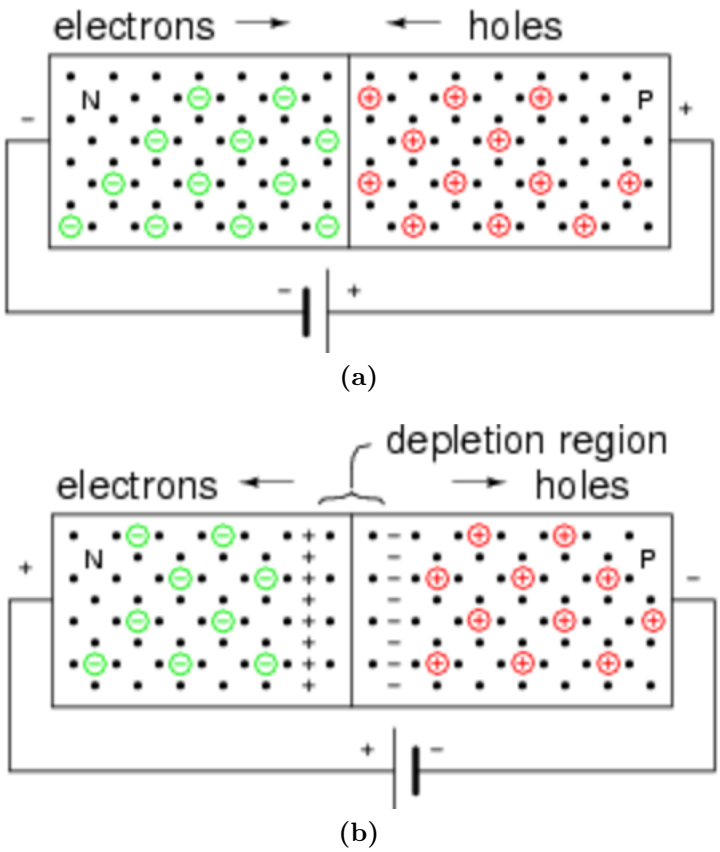

Figure 3.5: An illustration of p-n junction in forward bias and reverse bias are shown in panels (a) and (b) respectively.

$\overline{\text{P}}$ANDA experiment uses silicon strip sensors for the Lambda Disks Detector. The silicon strip detector is discussed in the following section.

3.3.2 Silicon Strip Sensors

The silicon bulk is lightly n^- doped and the junction is formed by highly doped p^+ strips. Each strip forms a p-n junction. The backplane is highly n^+ doped in the same manner. In the bulk between the two electrodes an electric field is present due the applied voltage. Because the detector is operated at reverse bias, no current flows except for a very low leakage current. However, if an ionizing particle traverses the detector, an equal number of free electrons and holes is generated. The electric field forces the charges to travel to the electrodes. The number of electron hole pairs depends on the energy of the particle and on the material it passes through. All tracking detectors are used the free charges resulting from the ionization of a passing charge particle through matter. Minimum Ionizing Particles (MIPs) have the lowest possible energy loss described by Bethe-Bloch-Formula in Equation 3.1. All measured charged particles are minimum ionizing in High Energy Physics.

$$-\frac{dE}{dx} = 2\pi N_a r_e^2 m_e c^2 \rho \frac{Z}{A}\frac{z^2}{\beta^2}\left[\ln\left(\frac{2m_e\gamma^2 v^2 W_{max}}{I^2}\right) - 2\beta^2 - \delta - 2\frac{C}{Z}\right] \quad (3.1)$$

where

N_a: Avogadro's number

m_e: mass of electron

$r_e(= e^2/m_e)$: classical electron radius

Z: atomic number of the absorbing material

A: atomic weight of the absorbing material

$\gamma = 1/\sqrt{1-\beta^2}$

I: mean excitation potential

W_{max}: maximum energy transfer in a single collision

δ: density correction

C: shell correction

c: speed of light

$\overline{\text{P}}$ANDA Lambda Disks Detector exploits the double-sided silicon

strip detectors which are explained in subsection 3.5.1

3.4 Material Budget Studies for Lambda Disks Detector

A detailed study of the introduced material budget and estimation of effective radiation length of LDD is required as described in section 3.1. The radiation length of a material is the mean length which is needed to reduce the energy of an electron by the factor $1/e$. It is a specific property of each material and will depend on atomic number (Z) and atomic mass (A) of the material.

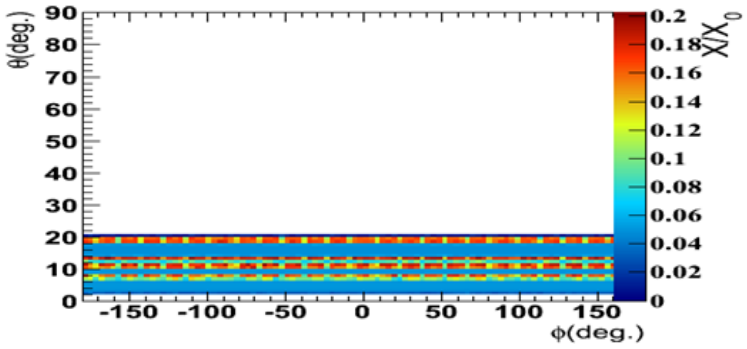

(a)

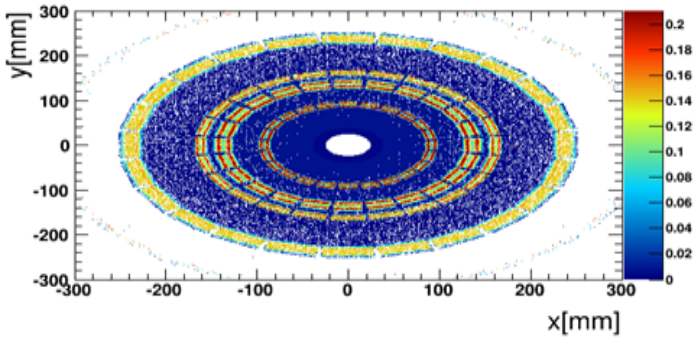

(b)

Figure 3.6: Fractional radiation length of Lambda Disks Detector in $\theta - \phi$ and $x - y$ coordinates are shown in panels (a) and (b) respectively.

The radiation length (X_0) can be approximated by the following analytical formula:

$$X_0 = \frac{716.4A}{Z(Z+1)ln\frac{287}{Z}} \quad [g.cm^{-2}]$$

If we have a detector component with a number of different materials, we can also estimate the combined radiation length. Then the impact of introduced material can be described by a fractional radiation length, X/X_0 which is given by following formula:

$$X/X_0 = \sum_j \frac{\rho_j \cdot L_j}{X_{0_j}}, \tag{3.2}$$

where X_{0_j} and ρ_j are the specific radiation length and the density of the material defined for the volume j, respectively, and L_j corresponds to the traversed path length therein. The material budget which corresponds to each component will be given in percent if X/X_0 is less than one or in multiples of X_0 if greater than and equals to one.

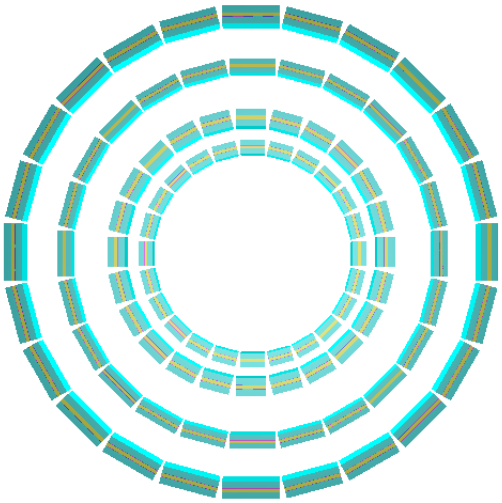

Figure 3.7: A picture of support structure of Lambda Disks.

In the present studies, the current version of the LDD (LambdaDisksSeparatedSupport) geometry is used which have silicon sensor in two ring and support made by carbon. Detector simulations is performed within the PandaRoot simulation framework by propagating a virtual particle called "geantino" with GEANT4 transport code. The geantino particle does not experience any physical interactions and for each geantino

the effective path lengths in all traversed components are calculated. The fractional radiation length (X/X_0) is then calculated based on component material of the LDD. Figures 3.6a and 3.6b show the estimated fractional radiation length of the LDD in $\theta - \phi$ and $x - y$ maps, respectively. In Figure 3.6b, the radiation length of ring sensors of both Disks indicated by blue color and for the support structure depicted by the circles of yellow color. A picture of support structure for Lambda Disks Detector is shown in Figure 3.7. It is observed from the radiation length maps that the fractional radiation length of Lambda Disks Detector is 20% of X_0.

3.5 Mechanical Design and Servicing for Lambda Disks Detector

To place Lambda Disks Detector with the $\overline{\text{P}}$ANDA detector setup, it is necessary to realize that how much space is available as well as needed for two disks along with its routing. We have done Computer Aided Designing (CAD) of each of the Lambda Disks as well as of their routing parts so that we can get an estimate of how much space is required for integrating disks after MVD. We have used CATIA 5.0 software to make design of these disks. Before moving towards the designing of CAD model of Lambda Disks, let us have a look on Double Sided Silicon Strip Sensor (DSSD) which are used to form outer and inner ring of both the disks. This work is done with the help of B.Tech project student at Indian Institute of Technology Indore.

3.5.1 Double Sided Micro Strip Trapezoidal Silicon Sensor

The Lambda Disks Detector utilizes double sided micro strip sensors of the trapezoidal shape as strips on both sides, which provides the 2D information of the particle traversing the detector. Also these strip sensor allows precise point reconstruction with less detector channels compared to pixel detector. The dimensions of Lambda Disks geometry are kept same as

the last two mixed disks of MVD. Therefore, outer ring of Lambda Disks is dimensionally same as designed for MVD. The geometry for the outer ring sensor is shown in Figure 3.8 and design parameters are tabulated in Table 3.1.

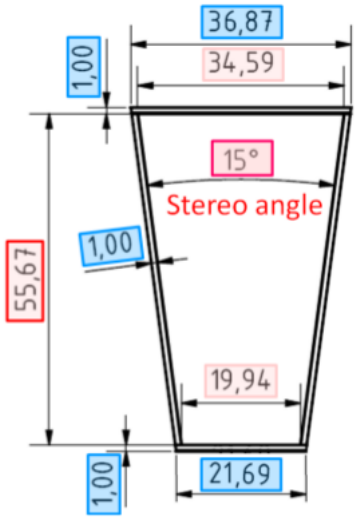

Figure 3.8: Geometry of trapezoidal shape DSSD for outer ring of LDD [24].

Both sides of the trapezoidal silicon strip sensors for outer ring of the Lambda Disks have 512 strips with a pitch of 67.5 μm. Strips run parallel to one of the edges of the trapezoid. Thus, those on the opposite side get shorter when approaching the sensor edge. Each sensor has a stereo angle of 15^0 between the two long edges and the sensor thickness is 285 μm.

Strip pitch	67.5μm
Strip orientaion	$\parallel$ to sensor edge
Number of strips	512/side
Stereo angle	15^0
Sensor height	57.67 mm
Total area	1688 mm^2
Active area	89.9%

Table 3.1: Design parameters of outer ring of LDD.

Inner ring requires a sensor of different dimensions, which is designed depending upon the radius of inner ring and other constraints. Inner ring of the disks have 768 strips per side with a pitch of 45 μm. Each sensor of inner ring has a stereo angle of 25.138^0 with sensor height of 46 mm.

The geometry for the inner ring sensor is shown in Figure 3.9 and design parameters are tabulated in Table 3.2.

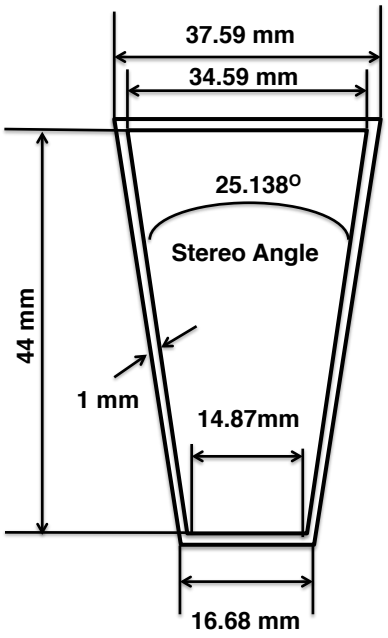

Figure 3.9: Geometry of trapezoidal shape double sided silicon strip sensors used for inner ring of LDD.

Strip pitch	45μm
Strip orientaion	$\parallel$ to sensor edge
Number of strips	768/side
Stereo angle	25.138^0
Sensor height	46 mm
Total area	1236.66 mm^2
Active area	88.17%

Table 3.2: Design parameters of inner ring of LDD.

3.5.2 CAD Model of Lambda Disks Detector

To start with we did analysis of full CAD model of MVD and central detector system in the CATIA software. After analysing we found that there is an empty space available after MVD, which has a total length of 60 cm, where two Lambda disks can easily be placed but then major

concern is for routing part since cables have to be taken out of the detector and there is hardly any left over space. Based upon above analysis we have designed outer ring of Lambda disks as shown in Figure 3.10.

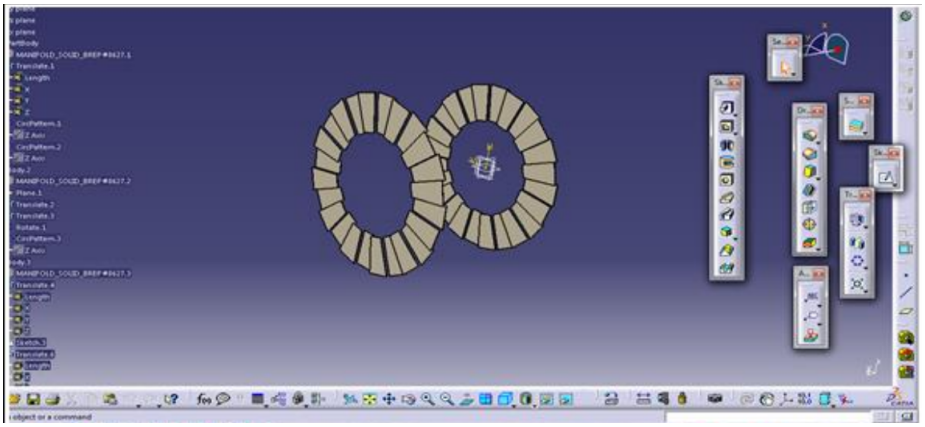

Figure 3.10: CAD design for outer ring of LDD.

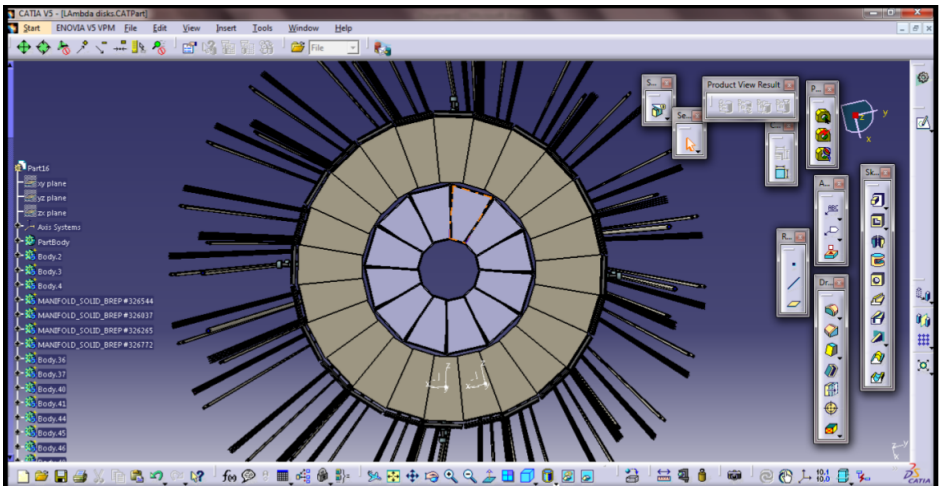

Figure 3.11: CAD design for Inner and Outer ring of LDD.

Radius of outer ring of Lambda disks is 13.5 cm, kept same as of two outer disks of MVD. The radius for inner ring obviously will be less and to cover as much area as possible designed the dimension of sensor which should be used for inner ring of Lambda Disks as already shown in Figure 3.9. The CAD model of Lambda Disks with inner and outer ring as well as some routing is shown in Figure 3.11. Next concern is to make a required estimate for various cables. It is important to estimate how many number of cables will be required for Lambda Disks Detector.

3.5.3 Routing for Lambda Disks Detector

A special feature of the $\overline{\text{P}}$ANDA experiment comes from the trigger less DAQ, that requires a very high output bandwidth because to the continuous flux of data that cannot exploit the de-randomisation coming from an external trigger at a lower rate. Besides, since at present the only way out from the MVD is in the backward region, the cabling becomes a serious issue because of the amount of material needed to take out all the data from the sensitive volume. Following are categories of cables that will be required for the Lambda Disks and its read out electronics:

- Power supply for sensors (HV lines)
- Power supply for Front end electronics (LV lines)
- Data cables from sensor
- Cooling pipe for readout chip

The number of various cables which is required for two Lambda Disks are listed bellow:

- Two power supply line per sensor (one HV line and One ground line)
- Four LV power lines for FE electronics (PASTA chips for each sensor)
- One cooling pipe per six sensor

For the Lambda disks, it is planned to use Module Data Concentrator (MDC) and GigaBit Transceiver (GBT) setup, since it will reduce the number of different pair lines to 4 per sensor, it would have been 24 per sensor otherwise. There are 4 LV lines required per sensor, which implies 4 DC-DC converter are required for each sensor. About number of GBTs required, we assumed it to be 1 per sensor right now. For MDC, one power supply and one supply for ground. Number of PAnda STrip ASIC (PASTA) chips required can be calculated as follows, since one PASTA chip has 128

readout channels, and wedge sensor used in Lambda Disks has 768 strips, therefore, on one side of sensor six PASTA chips are required, i.e. 12 for both sides of sensor. Based on the above conclusions, we have summarized all the quantities in Tables 3.3 and 3.4, which show the type and dimension, which can be used for these cables. These data have been taken from MVD Technical Design Report. Also Figure 3.12 shows the CAD model of complete Lambda Disks with all types of routing.

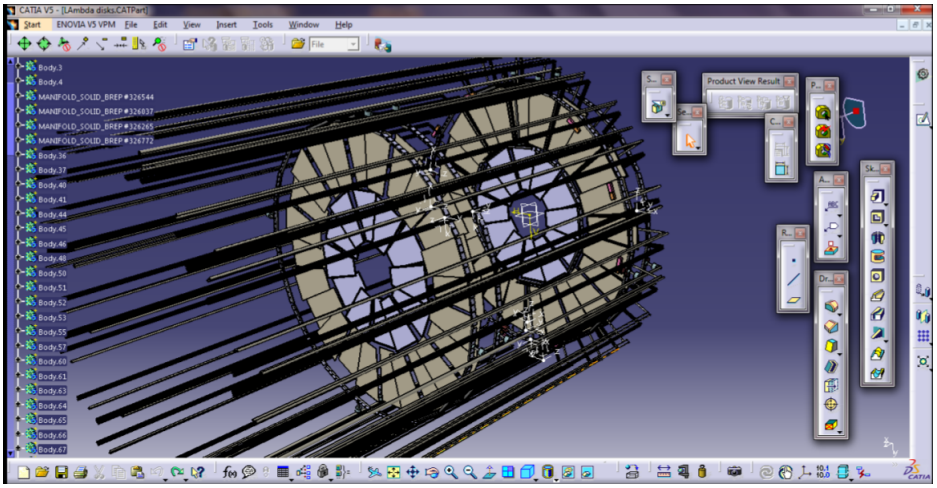

Figure 3.12: Complete CAD model of Lambda Disks with routing.

Lambda Disks	Sensor (num.)	PASTA chip	Cooling pipe	HV cable	MDC cable	FE cable	DC-DC converter	GBTs (num.)
Outer ring	48	576	8	96	96	192	192	48
Inner ring	24	288	4	48	48	96	96	24
Total	72	864	12	144	144	288	288	72

Table 3.3: Estimation of components for the Lambda Disks [35].

Routing Component	Type	Diameter Size (mm)
Sensor Supply	Cable (HV)	0.5
FE Lines	Cable (LV)	0.25
Cooling	Pipe	1.5

Table 3.4: Types and dimensions of cables [35].

3.5.4 Final Design of Lambda Disks Detector

We have decided to take all cables in forward direction till junction between central part and forward part of $\overline{\text{P}}$ANDA detector and then take it back parallel to STT. The final design of Lambda Disks and zoomed pictures are shown in Figures 3.13 and 3.14 respectively.

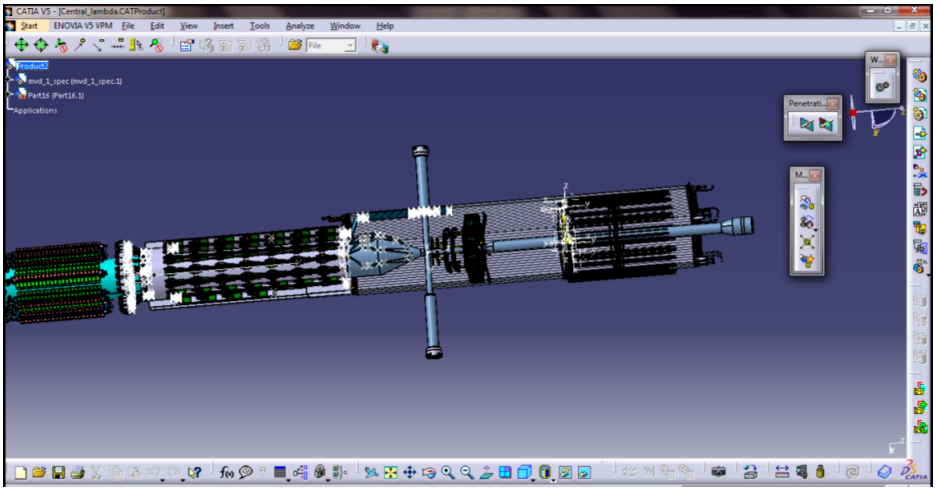

Figure 3.13: CAD design for Inner and Outer ring of LDD.

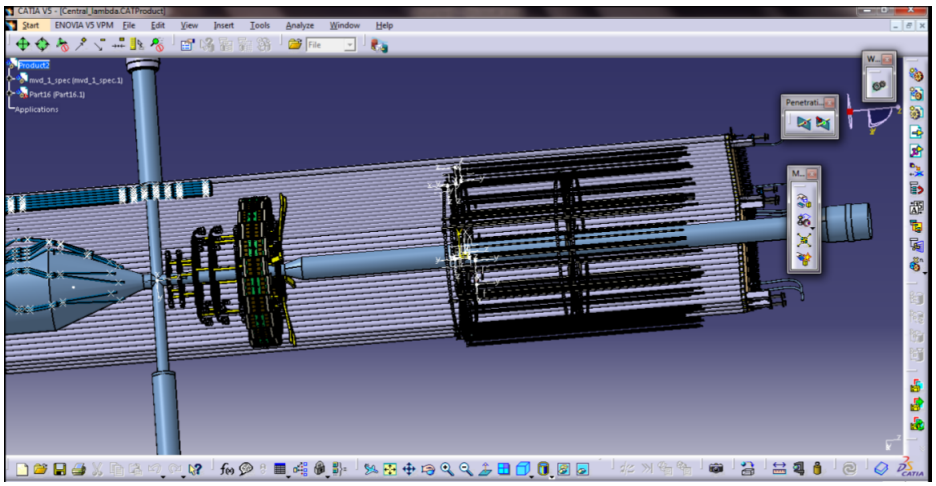

Figure 3.14: CAD design for Inner and Outer ring of LDD [35].

Chapter 4

Simulation of Hadronic Decay Reactions

The Lambda Disks Detector of the $\overline{\text{P}}$ANDA experiment is designed for improvement of the reconstruction efficiency and mass resolution of hyperons having long lifetime. In this chapter, simulation of $\bar{p}p \rightarrow \Lambda\bar{\Lambda}$ hyperonic benchmark channel with the sequencial decays $\Lambda \rightarrow p\pi^-$ and $\bar{\Lambda} \rightarrow \bar{p}\pi^+$ is done at two different beam momenta to do feasibility study for the $\overline{\text{P}}$ANDA Lambda Disks Detector. Addition of a new detector should not affect reconstruction capability of existing $\overline{\text{P}}$ANDA detector setup. Therefore, simulations of two mesonic channels $\bar{p}p \rightarrow D^{*+}D^{*-} \rightarrow D^0\pi^+\bar{D}^0\pi^-$ and $\bar{p}p \rightarrow J/\psi\pi^+\pi^-$ are performed in presence of Lambda Disks Detector to study the effect of this detector on the reconstruction of these channels.

4.1 The Simulation Framework

Each detector for any High Energy Physics (HEP) experiment requires a detailed simulation studies before the hardware development as these are very expensive to built. Particle physics community already developed many advanced level software programs for the simulation. To take advantage from these software programs, combined efforts have been made to develop FairRoot framework, which provides all core functionalities for running simulations to several experiments at the future FAIR facility. PandaRoot is the software to simulate the $\overline{\text{P}}$ANDA detector. In the following sections FairRoot and PandaRoot are described.

4.1.1 FairRoot

The FairRoot software has been developed to provide a computing structure for the future FAIR experiments as $\overline{\text{P}}$ANDA, CBM, NUSTAR etc [36]. It is based on the CERN ROOT package [37] and manages as the interfaces with simulation, tasks, parameter database, input and output. Detector simulation is organized by the Virtual Monte Carlo, which permits to use transport models Geant3 [38] or Geant4 [39] with the geometry definition and detector code.

4.1.2 PandaRoot

PandaRoot is an official simulation framework for $\overline{\text{P}}$ANDA full simulation, reconstruction and analysis. This is an offline software to perform the simulation, digitization, reconstruction, particle identification and analysis for the hadronic decay channels of user's interest [40]. The schematic of simulation chain with PandaRoot is shown in Figure 4.1.

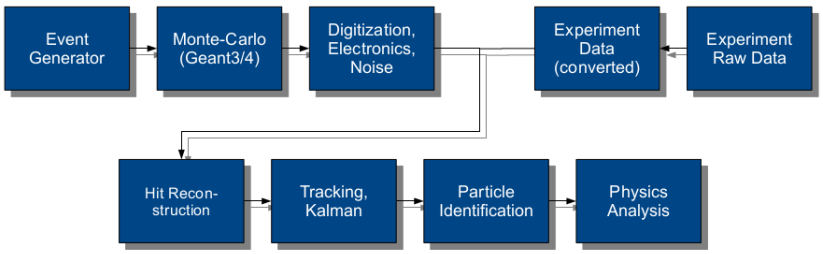

Figure 4.1: Schematic of simulation chain in PandaRoot Framework [41].

4.1.2.1 Event Generators

Event generators are software programs that generate high-energy particle physics events of our interest [42]. The output from an event generator contains the information of position and momentum of the final state particles, which have been created at the interaction point. Several event generators are available for the simulation with PandaRoot framework. For the particle decay of our interest, different event generators can be used for different

objectives.

EvtGenDirect is a single channel generator. User can specify decay chain of interest for the simulation through this software program. Many decay models for well known particles are present as modifying the distributions of momentum and angles depending on defined parameters. We can simulate the particular decay channel by providing its branching ratio. In order to have particles with uniform distributions in some variables, one has to use the PndBoxGenerator. With the Box Generator, it is possible to generate one particle randomly inside the detector. The user can define the multiplicity and momentum range for the particles which are being generated.

DPMGen simulates elastic and inelastic $\bar{p}p$ reactions with the Dual Parton Model (DPM) [43]. This event generator is used for background reactions in the $\overline{\text{P}}$ANDA detector setup.

PandaRoot is also capable to use Pythia event generator which can be used to produce signal and background events.

The Ultrarelativistic Quantum Molecular Dynamics model (UrQMD) [44] produces particle distributions for the reactions of antiprotons with heavy nuclei. The generated events of our interest from the event generators are the inputs for the full simulation process. The full simulation process has five steps:

4.1.2.2 Physics Simulation

Simulation is the first step in the whole process. The generated particles from the event generators propagate through all detector materials in presence of magnetic field. Geometry and the definition of active elements of each sub-detector have been defined inside the simulation framework. The generated particles are transported through these active volumes of sub-detectors facing different physical processes such as scattering, energy loss by ionization, Bremsstrahlung and Cherenkov emission etc. The properties of these particles are recorded by Monte Carlo data structure like tracking detectors keep information of the position and total energy loss for each

particle in a volume, cherenkov detectors store information of position, direction and velocity of charged particles and electromagnetic calorimeter records energy loss information.

4.1.2.3 Digitization

A collection of hits is given as output from the previous step, consisting of the intersection points and energy losses of all particles in the individual sub-detectors. This information is then used as input for the next step, which is the digitisation. This step models the signals from the individual sub-detectors and the processing of these in the front end electronics. The aim is to produce a detector output as similar as possible to real experimental data, so that the same reconstruction code can be used for the simulations and future experimental data by exchanging the digitisation output with real detector output. Actually, digitization task takes the created Monte Carlo hit points and divides the deposited energy according to entry and exit points of the sensitive element of the corresponding detector. Physical effects like electron drift is considered. Electronic readout is implemented.

4.1.2.4 Reconstruction

This step is used to reconstruct the tracks of particles based on the digitization step results. Particle reconstruction in PandaRoot proceeds through two steps. One is track finding and another is track fitting. In track finding, reconstructed hits from different detectors and detector layers are combined to possible tracks from particles. Track fitting finds fitted track parameter and can perform extrapolations of these parameters. The track finder algorithms are different for each sub-detector and track fitting is done by GENFIT package [45] based on kalman filter technique [46] using GEANE [47].

4.1.2.5 Particle Identification

Particle identification is the process of using information left by a particle while passing through a particle detector to identify the type of particle. The identification is first performed for each sub-detector individually. In general, there are just five particle types (p, K, π, μ, e) which live long enough to generate signals in the sensitive layers of the detector. Every sub-detector has a momentum range for each particle species in which it can contribute to the particle identification. The probability that a track is related to certain particle type is calculated from each individual sub-detector by estimating probability density function for each particle hypothesis. This function reflects the probability of a given particle being of a certain kind.

4.1.2.6 Physics Analysis

At the end of the simulation chain, the last step is the analysis of reconstructed physics events. The physics analysis is based on four momentum, positions and the identity of the reconstructed particles. Particle combination, selection and manipulation tools are provided by Rho package [48] within PandaRoot framework.

4.2 Simulation of the $\bar{p}p \rightarrow \Lambda\bar{\Lambda}$ Hyperon Channel

We are using this channel as an essential tool to understand reconstruction capability of the Lambda Disks Detector for Λ hyperons close to production threshold (1.436 GeV/c) and above. It is important to study lifetime as well as kinematics of produced hyperons to optimize the reconstruction performance and design parameters of the Lambda Disks Detector. The reconstruction of the Λ hyperons from their daughter particles specially from $\bar{\Lambda}$ to $\bar{p}\pi^+$ and Λ to $p\pi^-$ differs as daughter charged particles of these hyperons do not originate from the interaction point due to their large

decay length [5]. Hence, a detailed understanding of the reconstruction and identification of $\bar{\Lambda}$ or Λ particles in $\overline{\text{P}}$ANDA detector is very important for many aspects of the $\overline{\text{P}}$ANDA hyperon physics program.

The reaction $\bar{p}p \rightarrow \Lambda\bar{\Lambda} \rightarrow p\bar{p}\pi^+\pi^-$ is simulated and reconstructed at an incoming antiproton beam momentum of 1.8 GeV/c and 4.0 GeV/c. The schematic illustration of this reaction is shown in Figure 4.2. We have selected 1.8 GeV/c beam momentum which is near the threshold and another one at 4 GeV/c to compare the performance of the detector with increasing beam momentum. At both beam momenta, 5×10^5 $\Lambda\bar{\Lambda}$ events are analyzed. The EvtGenDirect [49] event generator is used for the generation of $\Lambda\bar{\Lambda}$ events. EvtGenDirect provides two different decay models for this decay i.e. LambdaLambdaBar and LambdaLambdaBarHE. The LambdaLambdaBar model is used for event simulation based on experimental angular distribution which is described by 8^{th} order Legendre polynomials as suggested in Ref. [50] for the beam momentum at 1.8 GeV/c. The LambdaLambdaBarHE decay model is used which is also based on an angular distribution parametrization using a momentum dependent exponential function [51] and simulated at beam momentum of 4.0 GeV/c.

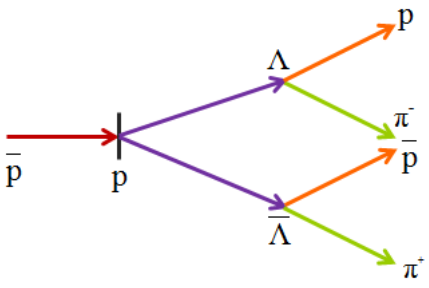

Figure 4.2: Schematic illustration of $\bar{p}p \rightarrow \Lambda\bar{\Lambda} \rightarrow p\bar{p}\pi^+\pi^-$.

Simulation studies like angular distributions of final state particles, momentum correlations of produced hyperons and their daughter particles, decay lengths, simulation of decay vertex positions are performed. Hit count studies, position and momentum resolution are studied with and without the Lambda Disks Detector. Moreover, track reconstruction efficiency and mass resolution in presence of LDD are evaluated at both beam

momenta. The above said studies are discussed in detail in the following sections.

4.2.1 Angular Distribution of Final State Particles from Produced Hyperons

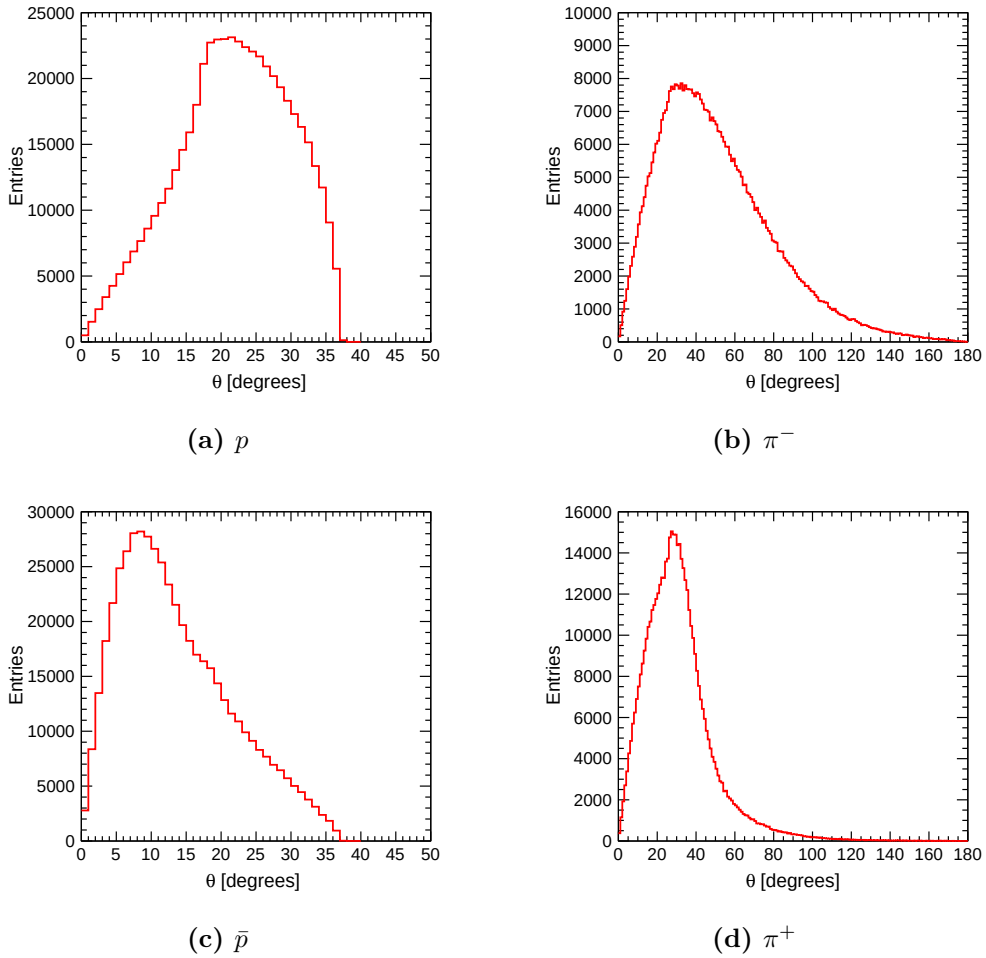

(a) p **(b)** π^-

(c) $\bar{p}$ **(d)** π^+

Figure 4.3: Angular distribution of daughter particles of Λ are shown in panels (a) and (b), at beam momentum of 1.8 GeV/c. Similarly, it is shown for $\bar{\Lambda}$ in panels (c) and (d). Here polar angle θ is considered in lab frame of reference.

Lambda (Λ) hyperons are reconstructed from their daughter particles (p, π^-, $\bar{p}$, π^+). An absolute understanding is necessary about the direction of these particles inside the target spectrometer and to determine exact design parameters of the detector. Therefore, it is important to figure out angular distributions of daughter particles. The angular distribution of all

final state particles in lab frame using their Monte Carlo information are shown in Figure 4.3. At lower beam momentum, proton and antiproton are travels up to 40^0 and pions (π^- and π^+) distributed throughout the whole angular range. Similarly, at higher beam momentum of 4.0 GeV/c, the angular distribution of daughter particles are extracted to direction of produced hyperons inside the target spectrometer. Figure 4.4 shows the angular distributions of daughter particles p and π^- from Λ and $\bar{p}$ and π^+ from $\bar{\Lambda}$. It is concluded from the angular distribution results that $\bar{\Lambda}$ is more forward boosted in comparison with Λ at both beam momenta as well as at increasing beam momentum.

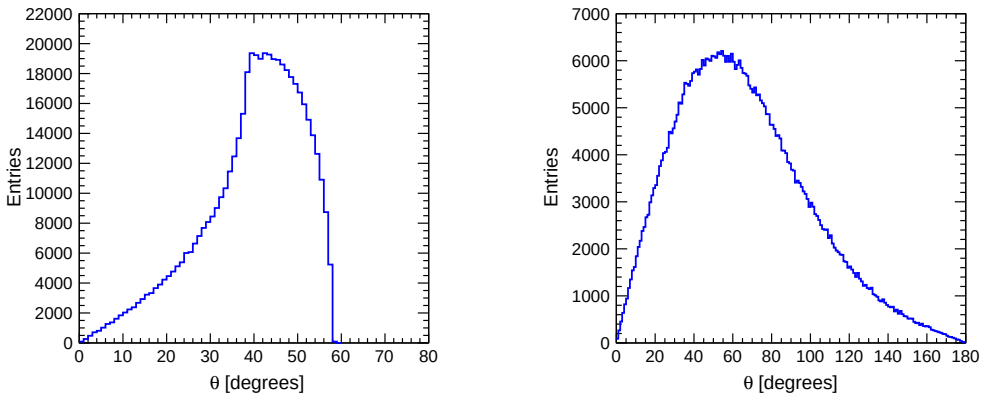

(a) p **(b)** π^-

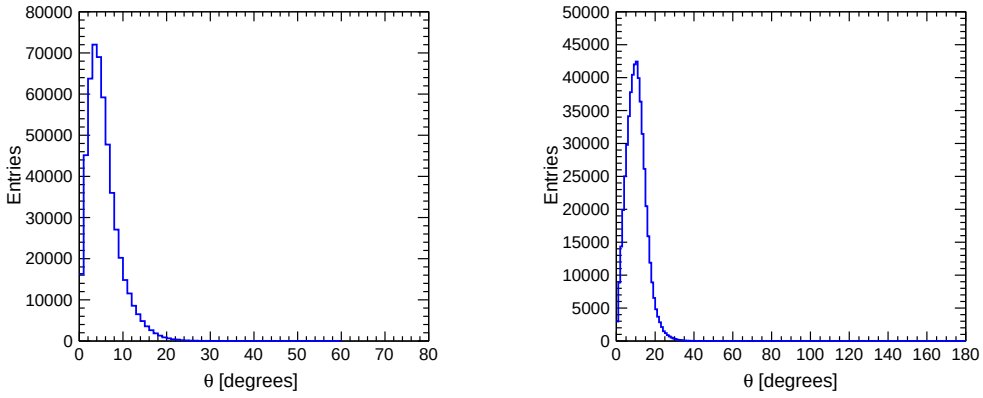

(c) $\bar{p}$ **(d)** π^+

Figure 4.4: Angular distribution of daughter particles of Λ are shown in panels (a) and (b) at beam momentum of 4.0 GeV/c. Similarly, it is shown for $\bar{\Lambda}$ in panels (c) and (d). Here polar angle θ is considered in lab frame of reference.

4.2.2 Momentum Correlations of Λ and $\bar{\Lambda}$ Hyperons and their Decay Products

The reaction $\bar{p}p \rightarrow \Lambda\bar{\Lambda}$ is endothermic with negative Q value since Λ hyperon mass are larger than proton mass. Thats why, momenta of the final state hyperons are smaller than the momenta of the initial state $\bar{p}$ and p in the center of mass system, especially near threshold and the lab momentum vectors of the hyperons are constrained to form ellipse around the beam direction after the boost to the lab frame. This is illustrated in Figure 4.5 for the Λ hyperons. It is evident from the Figure panels that transverse momentum is small compared to longitudinal momentum due to effect of boost along the beam direction. Exactly at production threshold of this reaction, this would result that transverse momentum is zero and longitudinal momentum becomes half of the incoming beam momentum.

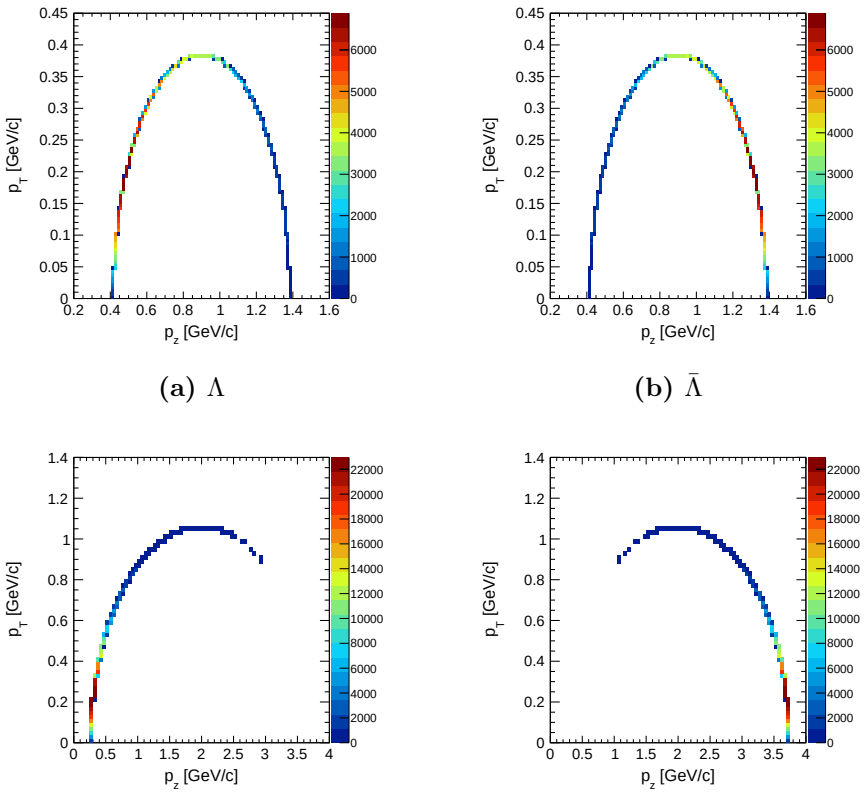

(a) Λ **(b)** $\bar{\Lambda}$

(c) Λ **(d)** $\bar{\Lambda}$

Figure 4.5: Transverse momentum (p_T) versus longitudinal momentum (p_z) for Λ and $\bar{\Lambda}$ hyperons at 1.8 GeV/c are shown in panels (a) and (b). Panels (c) and (d) are shown at 4.0 GeV/c beam momentum.

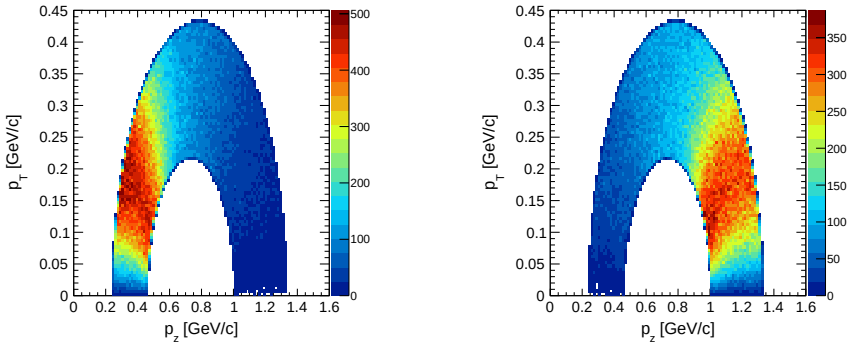

(a) p **(b)** $\bar{p}$

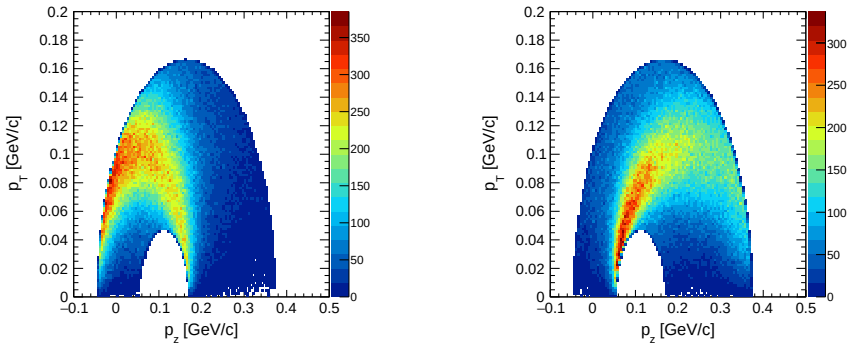

(c) π^- **(d)** π^+

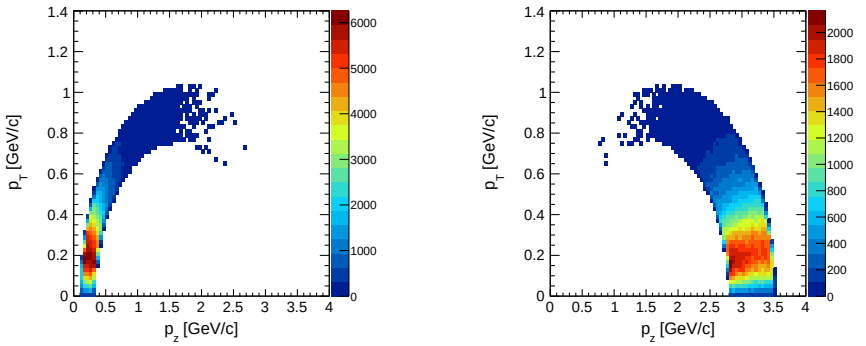

(e) p **(f)** $\bar{p}$

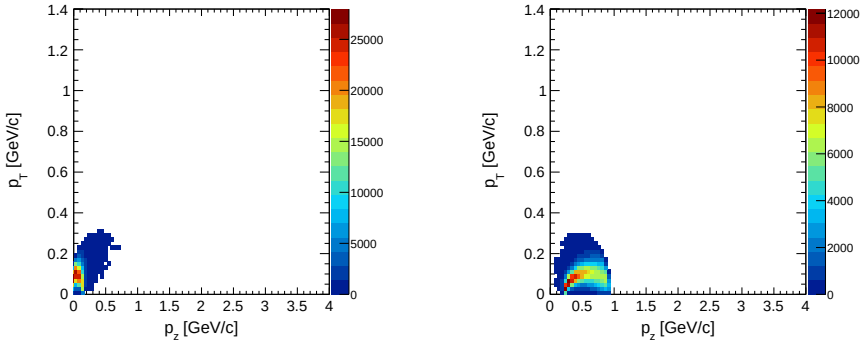

(g) π^- **(h)** π^+

Figure 4.6: Transverse momentum (p_T) versus longitudinal momentum (p_z) are shown for p, $\bar{p}$, π^-, π^+ in panels (a) (b) (c) and (d), at 1.8 GeV/c, respectively. Similarly, it is shown in panels (e) (f) (g) and (h) at 4.0 GeV/c beam momentum.

In Figure 4.6, kinematics of daughter particles in p_T-p_z momentum space are shown at both beam momenta. The daughter particles of the Λ and $\bar{\Lambda}$ are also forward boosted. However, p and $\bar{p}$ are more forward boosted compared to pions at both the beam momenta.

4.2.3 Study of Λ and $\bar{\Lambda}$ Hyperons Decay Length

Hyperons decay through weak interaction, therefore, they have long lifetime of the order of 10^{-10} sec. Decay length of Λ hyperons are studied to know the average distance they travel before the decay. The decay length of Λ hyperons are defined as the average distance between the production vertex and the decay vertex. Generally, decay of particles is defined by the following equation:

$$N(t) = N_0 e^{-\lambda t}$$

, where λ is the decay constant and t is the proper time of the particle. The average lifetime τ of a particle is defined by $\frac{1}{\lambda}$. τ is multiplied by c to calculate the decay length of a particle. The proper time (t) of particle is calculated by the following formula:

$$t = L \times \frac{M}{P} = \frac{L}{\beta\gamma},$$

where L is the length from production vertex. M and P are mass and momentum of the produced hyperons.

The proper time distribution is fitted with exponential function and slope of the distribution is extracted to calculate the average lifetime of decay particle which is shown in Figure 4.7. The average lifetime time (τ) is equivalent to decay length of particle in natural units. There is a discrepency in the calculated decay length with the PDG value [$c\tau = 7.89$ cm] [54]. Table 4.1 shows the estimated decay length value of Λ hyperons at both beam momenta.

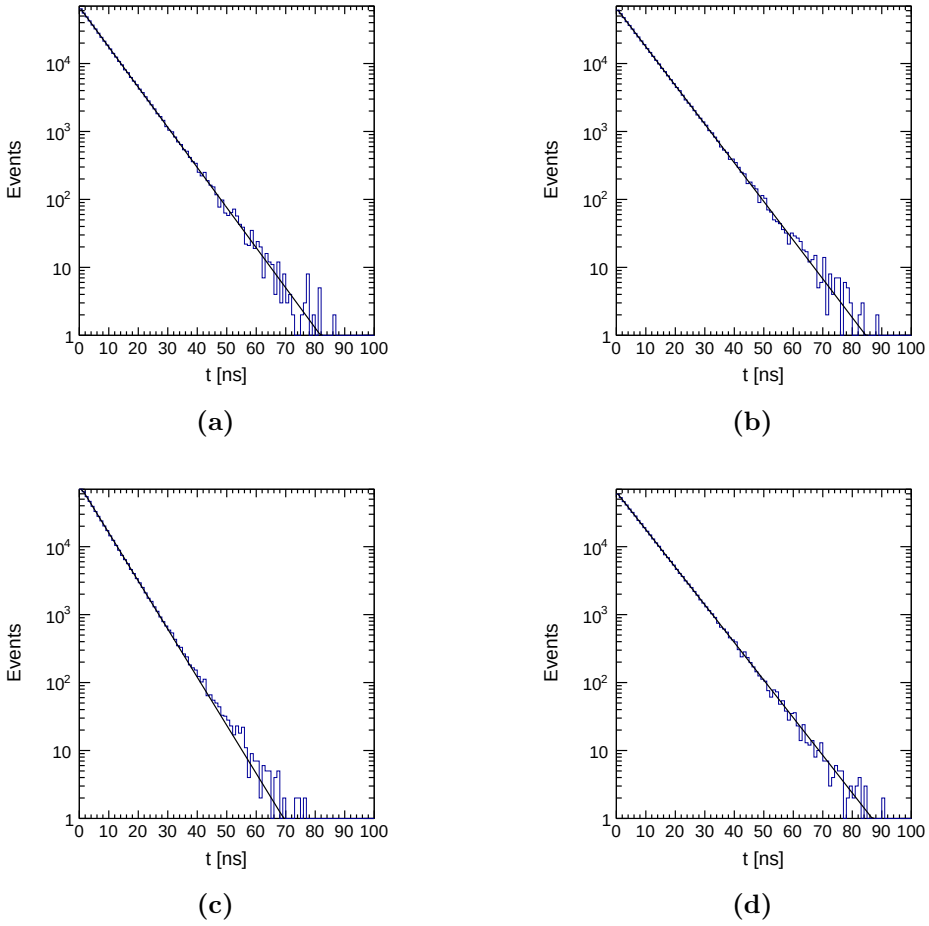

Figure 4.7: Proper time distribution of Λ and $\bar{\Lambda}$ particles at beam momentum 1.8 GeV/c are shown in panels (a) and (b) and at beam momentum of 4.0 GeV/c are shown in panels (c) and (d).

4.2.4 Position of Secondary Decay Vertex

Hyperons should decay before the detector volume and hence they are reconstructed through their decay particles. In this particular study, two layers of the Lambda Disks Detector are placed at 40 cm and 60 cm from the interaction point. The decay vertex position of the hyperons is calculated from their daughter particles. Radial (R) versus longitudinal (Z) components of decay vertex position for Λ and $\bar{\Lambda}$ are shown in Figure 4.8 at both incoming beam momenta. The simulation at incoming beam momentum 1.8 GeV/c shows that 99.85% of Λ and 99.03% of $\bar{\Lambda}$ decay before the first layer and 99.98% of Λ and 99.89% of $\bar{\Lambda}$ decay before the second layer of Lambda Disks Detector.

p_{beam} **(GeV/c)**	$c\tau_{\Lambda}$ **(cm)**	$c\tau_{\bar{\Lambda}}$ **(cm)**
1.8	7.3475 ± 0.0000	7.6277 ± 0.0015
4.0	6.1312 ± 0.0012	7.8492 ± 0.0015

Table 4.1: Decay length ($c\tau$) of Λ and $\bar{\Lambda}$. Errors are less than 0.002 cm.

Similarly, 99.97% of Λ and 79.17% of $\bar{\Lambda}$ decay before the first layer and 99.99% of Λ and 90.46% of $\bar{\Lambda}$ decay before the second layer of Lambda Disks Detector. In this study, most of the events decay before the Lambda Disks Detector at 1.8 GeV/c. However, at beam momentum of 4.0 GeV/c, we observe that 20% and 10% $\bar{\Lambda}$ events decay after first and second layer of Lambda Disks Detector, respectively. Therefore, it gives us a scope to place the Lambda Disks Detector at different positions as the decay vertex varies with incoming beam momentum.

4.2.5 Hit Count Study with and without the Lambda Disks Detector

A high spatial coverage with a sufficient number of track points inside the tracking detector is needed to achieve the required tracking performance. At least four track points are required for the reconstruction of a track from tracking algorithm. The central detection system of $\overline{\text{P}}$ANDA detector has STT and MVD in barrel part and forward part is covered by six forward disks of MVD. The LDD will add two more disk layers in polar angle range from 3^0 to 20^0. Therefore, the hit counts are studied for final state particles from the reaction $\bar{p}p \rightarrow \Lambda\bar{\Lambda}$ without and with LDD to see the effect of these additional disks. Figure 4.9 shows $\theta - \phi$ distribution of average number of hits from final state particles (p, $\bar{p}$, π^+, π^-) without LDD at beam momentum 1.8 GeV/c. Figure 4.10 show the same after the addition of LDD. Figures 4.11 and 4.12 shows the same study without and with LDD at beam momentum of 4 GeV/c, respectively. We observe that average number of hit points per track for all final state particles are increased in the angular interval of 3^0 to 20^0 covered by the Lambda Disks Detector at beam momentum 1.8 GeV/c. At high beam momentum

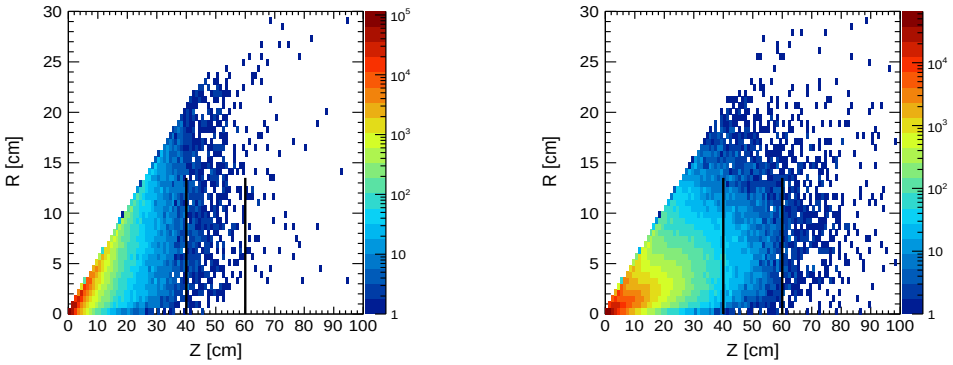

(a) Λ **(b)** $\bar{\Lambda}$

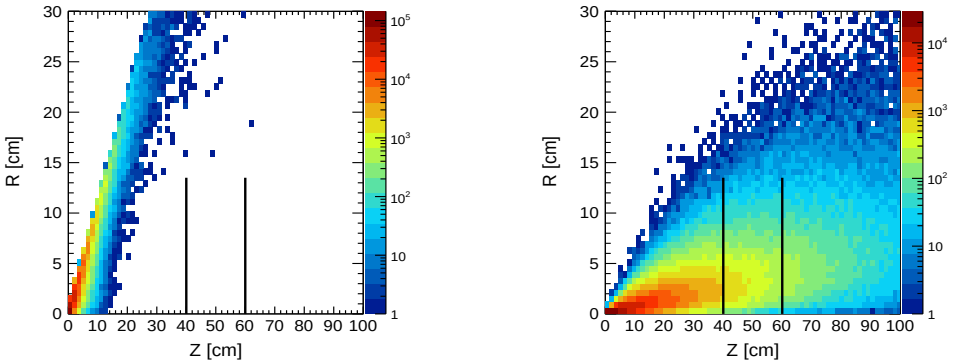

(c) Λ **(d)** $\bar{\Lambda}$

Figure 4.8: Radial (R) versus longitudinal (Z) decay vertex position of Λ and $\bar{\Lambda}$ at beam momentum of 1.8 GeV/c are shown in panels (a) and (b). In panels (c) and (d) are shown at 4.0 GeV/c. The vertical black lines at 40 cm and 60 cm from the interaction point indicate the position of Lambda Disks Detector.

4 GeV/c, it is observed that the number of hit points for all final state particles are increased after adding Lambda Disks Detector except proton. The hit counts for the final state particles p, $\bar{p}$, π^+, π^- with and without Lambda Disks are clearly shown in Figure 4.13 at both beam momenta. In Figure 4.13 (a), it appears that for protons, four hits start around 5^0 and remain almost same throughout the full angular range. Similarly, π^+ and π^- register more than six hits, starting from 3^0 throughout the full angular range of the Lambda Disks Detector. Above a polar angle of 20^0, the effect of the Micro Vertex Detector forward disk can be observed. Hit counts for all particles increase after adding the Lambda Disks Detector to the $\overline{\text{P}}$ANDA detector setup.

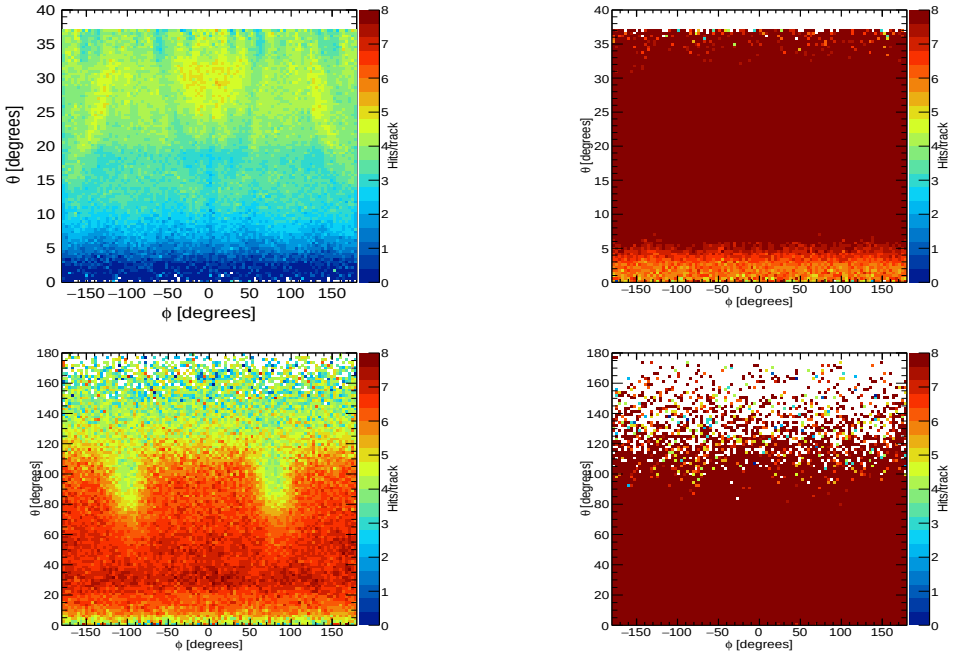

Figure 4.9: Average number of hits per track for all daughter particles (p, $\bar{p}$, π^-, π^+) without Lambda Disks Detector at beam momentum of 1.8 GeV/c. x and y axes indicate the azimuthal (ϕ) and polar (θ) angle coverage for different detectors, respectively.

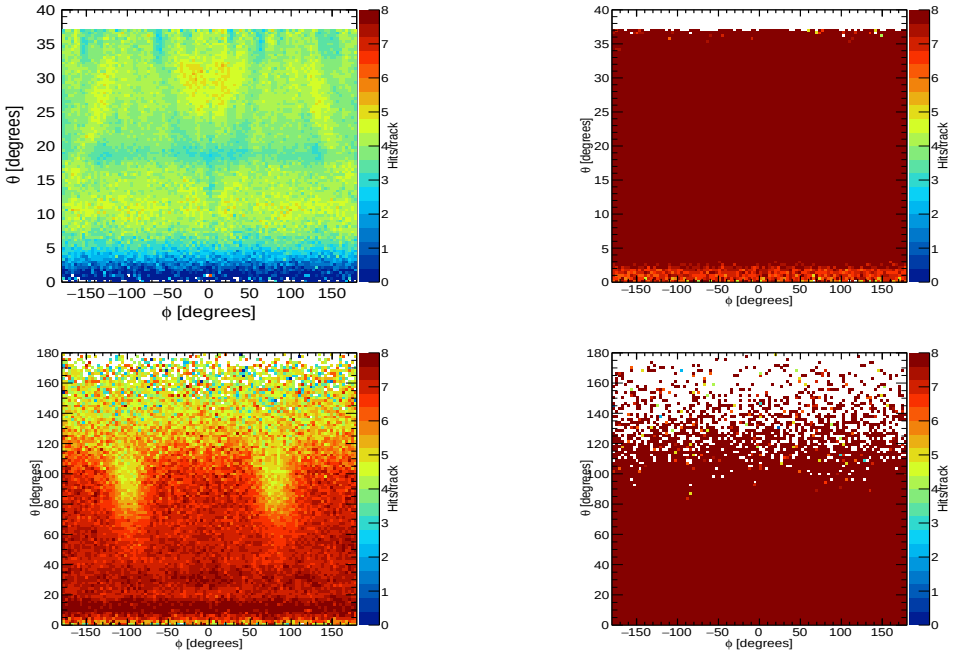

Figure 4.10: Average number of hits per track for all daughter particles (p, $\bar{p}$, π^-, π^+) with Lambda Disks Detector at beam momentum of 1.8 GeV/c. x and y axes indicate the azimuthal (ϕ) and polar (θ) angle coverage for different detectors, respectively.

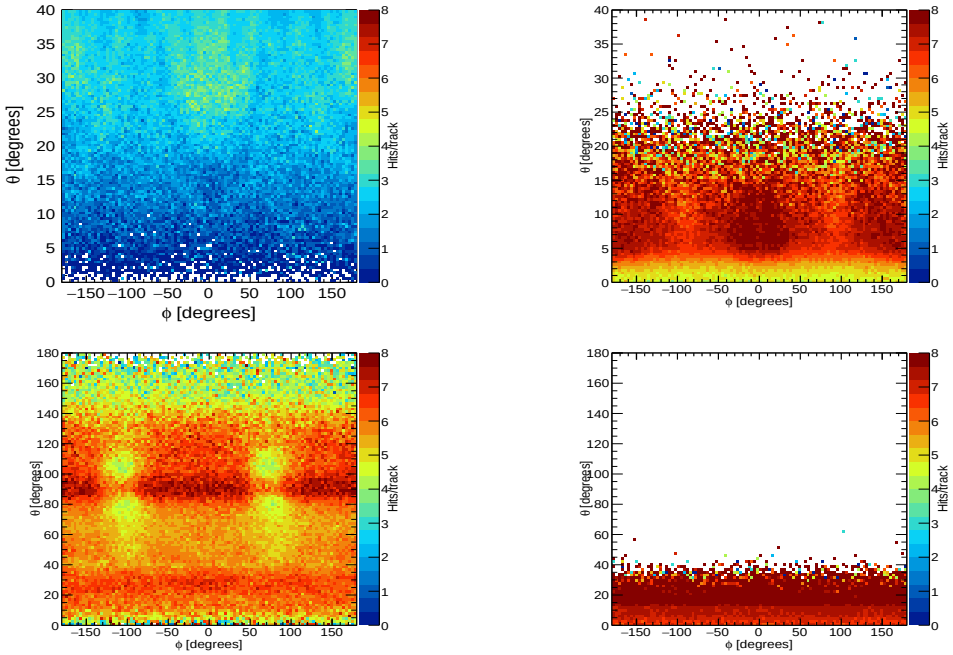

Figure 4.11: Average number of hits per track for all daughter particles (p, $\bar{p}$, π^-, π^+) without Lambda Disks Detector at beam momentum of 4.0 GeV/c. x and y axes indicate the azimuthal (ϕ) and polar (θ) angle coverage for different detectors, respectively.

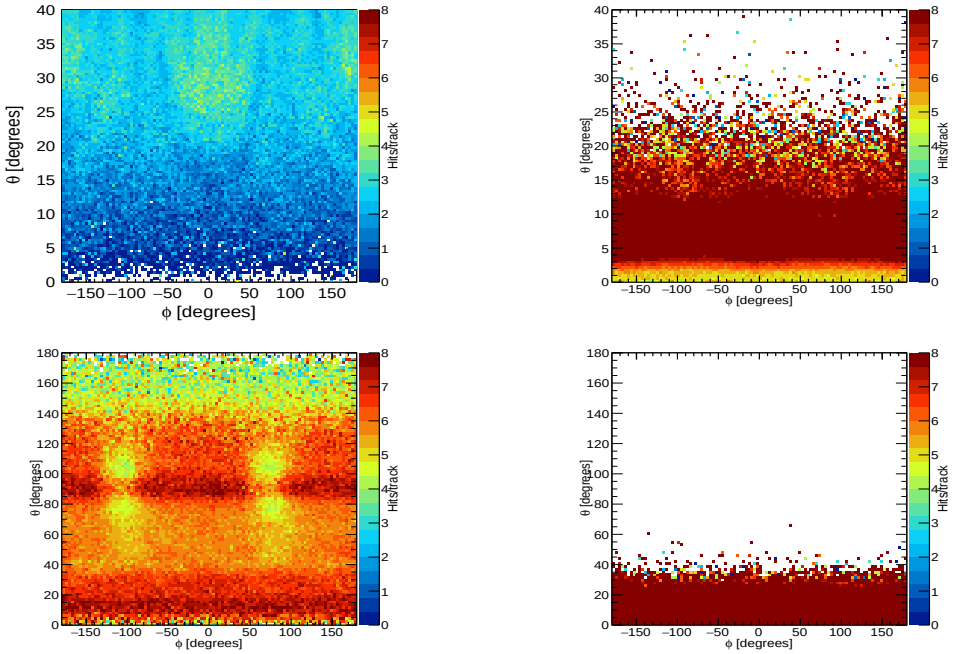

Figure 4.12: Average number of hits per track for all daughter particles (p, $\bar{p}$, π^-, π^+) with Lambda Disks Detector at beam momentum of 4.0 GeV/c. x and y axes indicate the azimuthal (ϕ) and polar (θ) angle coverage for different detectors, respectively.

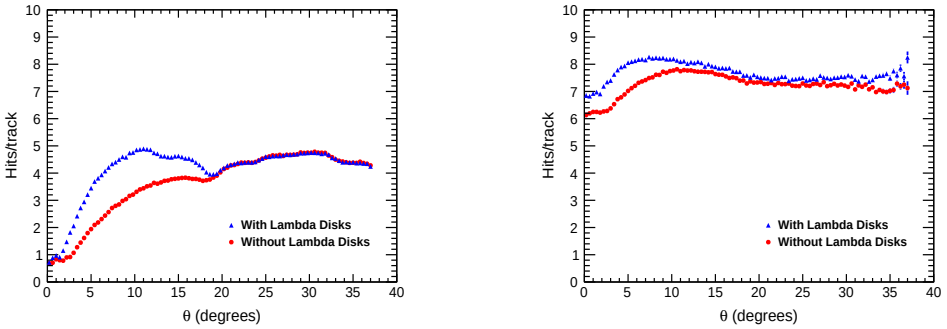

(a) p **(b)** $\bar{p}$

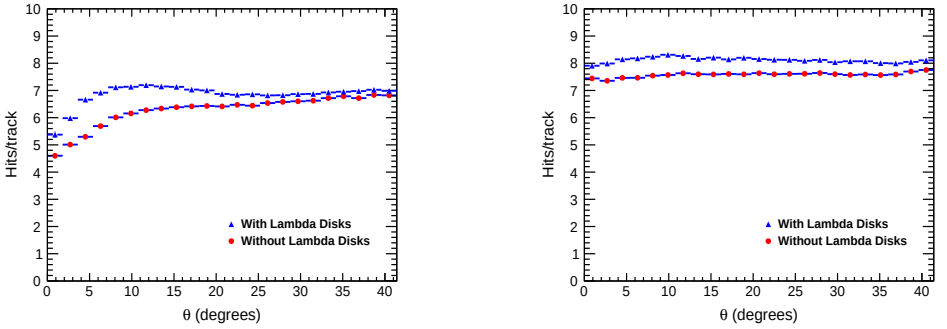

(c) π^- **(d)** π^+

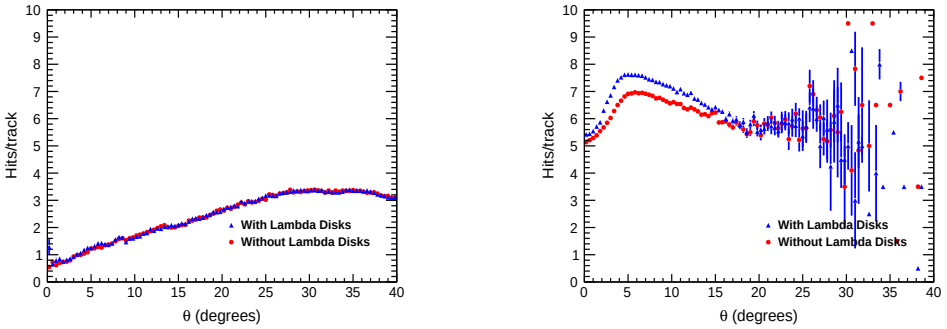

(e) p **(f)** $\bar{p}$

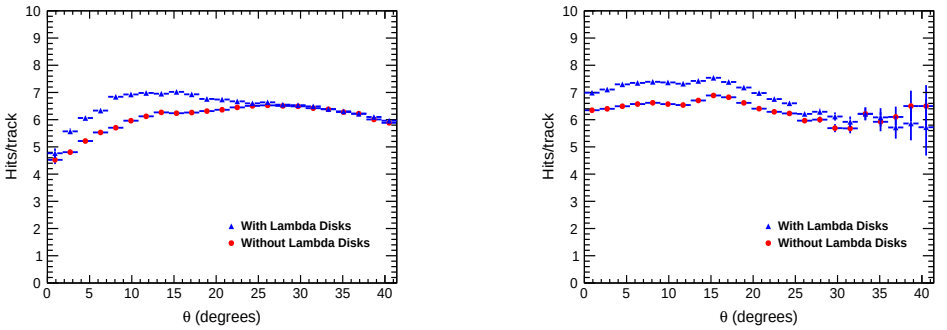

(g) π^- **(h)** π^+

Figure 4.13: Average number of hits per track vs polar angle (θ) for all final state particles (p, $\bar{p}$, π^-, π^+) at beam momentum of 1.8 GeV/c are shown in panels (a), (b), (c) and (d), respectively. Similarly, it is shown at 4 GeV/c in panels (e), (f), (g) and (h), respectively.

Most important is the effect for protons in regions below 20^0 at 1.8 GeV/c, due to the Lambda Disks Detector, the number of hit points per track rises above four which allows individual tracking of the particle. However, at high beam momentum (4 GeV/c), this effect for proton is no more there. At higher beam momenta of 4.0 GeV/c, antiprotons are getting boost in comparison to protons and this effect can be observed in Figure 4.13 (e). Antiprotons have more than six hits throughout the angular coverage of the Lambda Disks Detector. Similarly, π^+ and π^- register more than six and seven hits after adding Lambda Disks to $\overline{\text{P}}$ANDA detector setup.

4.2.6 Event Reconstruction and Particle Identification Criteria

The "ideal track finder" algorithm and "ideal particle identification" are used to find the tracks from secondary decay vertices as algorithm for secondary tracking are still under development within the PandaRoot framework. The ideal track finder used the concept to match hits from STT to MC tracks and adding MVD and GEM hits afterwords. Ideal particle identification means that a candidate is associated to its Monte Carlo true PID. The ideal particle identification algorithm sets the particle probability by the Monte Carlo truth value.

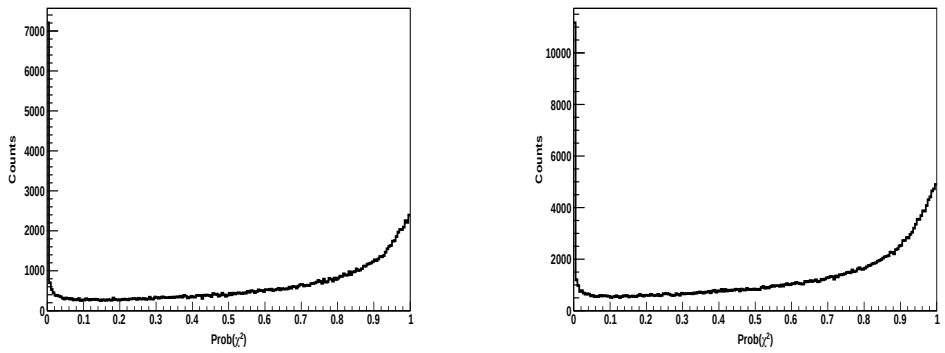

Figure 4.14: χ^2 - probability distribution of Λ and $\bar{\Lambda}$ are shown after applying PndKinVtxFitter fitter.

Λ and $\bar{\Lambda}$ events are reconstructed by combining their daughter par-

ticles. All p and π^- are combined event-wise to get the Λ particles and all $\bar{p}$ and π^+ are combined to get the $\bar{\Lambda}$ particle. A vertex-fitter named as PndKinVtxFitter [55] is applied to find a common vertex for both Λ and $\bar{\Lambda}$ particle tracks. The PndKinVtxFitter is basically intended to find a common origin or vertex for several charged particles. In this fitting approach it also finds the improved 4-vectors of all involved particles under the constraint of a common origin. Figure 4.14 shows the probability distributions for Λ and $\bar{\Lambda}$ after applying kinematic vertex fitter. There is a rise in upper end of the spectra because the error parameters in the covariance matrix in the vertex fitter is not proper. However, we have selected events in which χ^2 probability for both Λ and $\bar{\Lambda}$ are greater than 0.01.

4.2.7 Invariant Mass Distribution

The combination of four momentum of p and π^- gives four momentum of Λ while the combination of four momentum of $\bar{p}$ and π^+ gives four momentum of $\bar{\Lambda}$ hyperon. The invariant mass of Λ particles is 1.115 GeV/c^2. The invariant mass distributions of Λ and $\bar{\Lambda}$ hyperons are shown in Figures 4.15 and 4.16 without and with Lambda Disks Detector at incoming beam momentum of 1.8 GeV/c and 4.0 GeV/c.

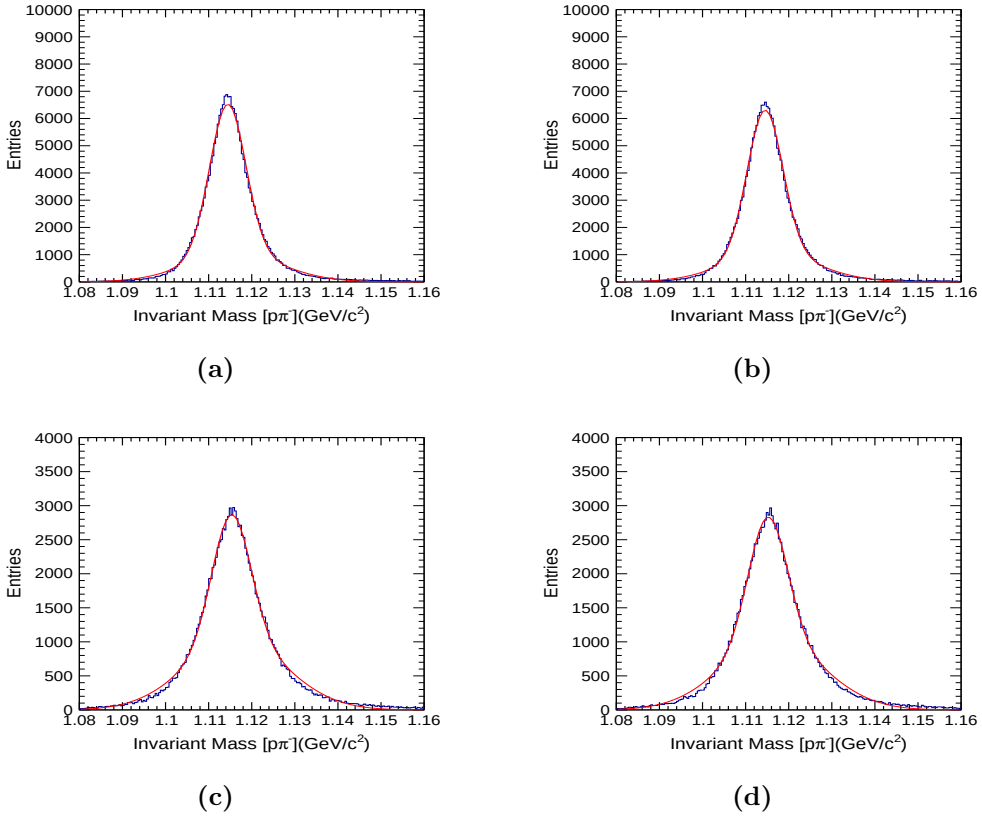

Figure 4.15: Invariant mass of Λ at beam momentum 1.8 GeV/c are shown in panels (a) and (b) without and with Lambda Disks Detector. In panels (c) and (d), similar distributions are shown for Λ at beam momentum 4.0 GeV/c.

A double Gaussian function is used to fit the mass distribution of Λ and $\bar{\Lambda}$ because the combinatorial background also looks like a Gaussian shape. The mean and sigma (σ) of the distribution without and with Lambda Disks Detector are tabulated in Tables 4.2 and 4.3, respectively. The combinatorial background rises due to wrong combinations of daughter particles.

The reconstructed invariant masses of Λ and $\bar{\Lambda}$ hyperons after applying kinematic fit are shown in Figures 4.17 and 4.18 without and with Lambda Disks Detector. A double Gaussian function is fitted to the mass distribution after applying PndKinVtxFitter vertex fitter. The mean values and σ of the distributions after vertex fitting without and with Lambda Disks Detector are tabulated in Tables 4.2 and 4.3, respectively.

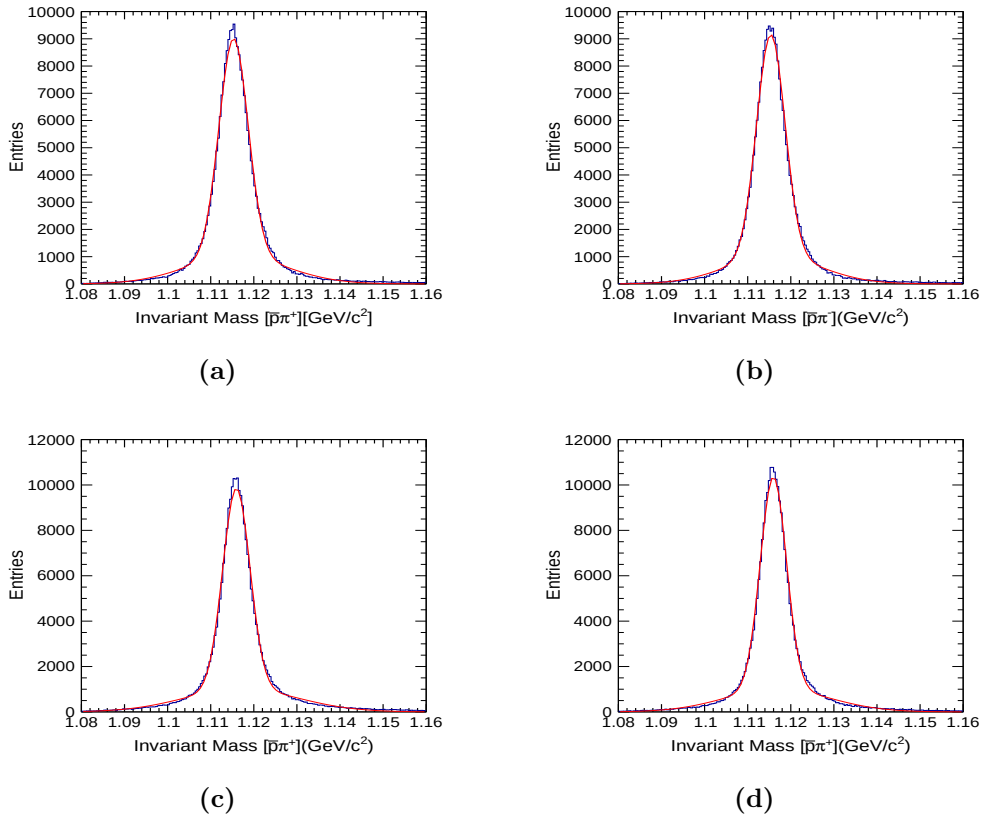

Figure 4.16: Invariant mass of $\bar{\Lambda}$ at beam momentum 1.8 GeV/c are shown in panels (a) and (b) without and with Lambda Disks Detector. In (c) and (d), similar distributions are shown for $\bar{\Lambda}$ at beam momentum 4.0 GeV/c.

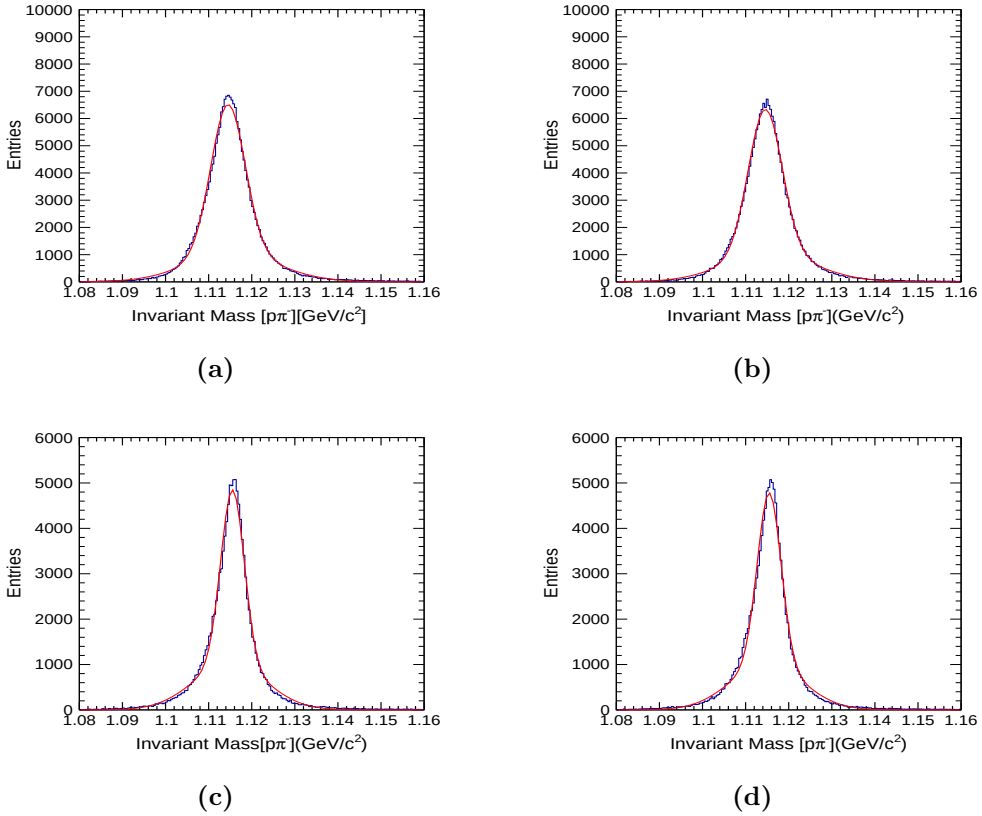

Figure 4.17: Invariant mass of Λ after kinematic vertex fitting at beam momentum 1.8 GeV/c are shown in panels (a) and (b) without and with Lambda Disks Detector. In panels (c) and (d), similar distributions are shown for Λ at beam momentum 4.0 GeV/c.

$\mathbf{P}_{beam}$ **[GeV/c]**	**Particle**	**Mean** [GeV/c^2]	σ [GeV/c^2]
1.8	Λ	1.114	0.004
	$\bar{\Lambda}$	1.115	0.003
4.0	Λ	1.115	0.004
	$\bar{\Lambda}$	1.116	0.003
		After Kinematic Vertex Fitting	
1.8	Λ	1.114	0.004
	$\bar{\Lambda}$	1.115	0.003
4.0	Λ	1.116	0.003
	$\bar{\Lambda}$	1.116	0.002

Table 4.2: Reconstructed invariant mass of Λ and $\bar{\Lambda}$ without the LDD at two different beam momenta. Errors are less than 1 MeV/c^2.

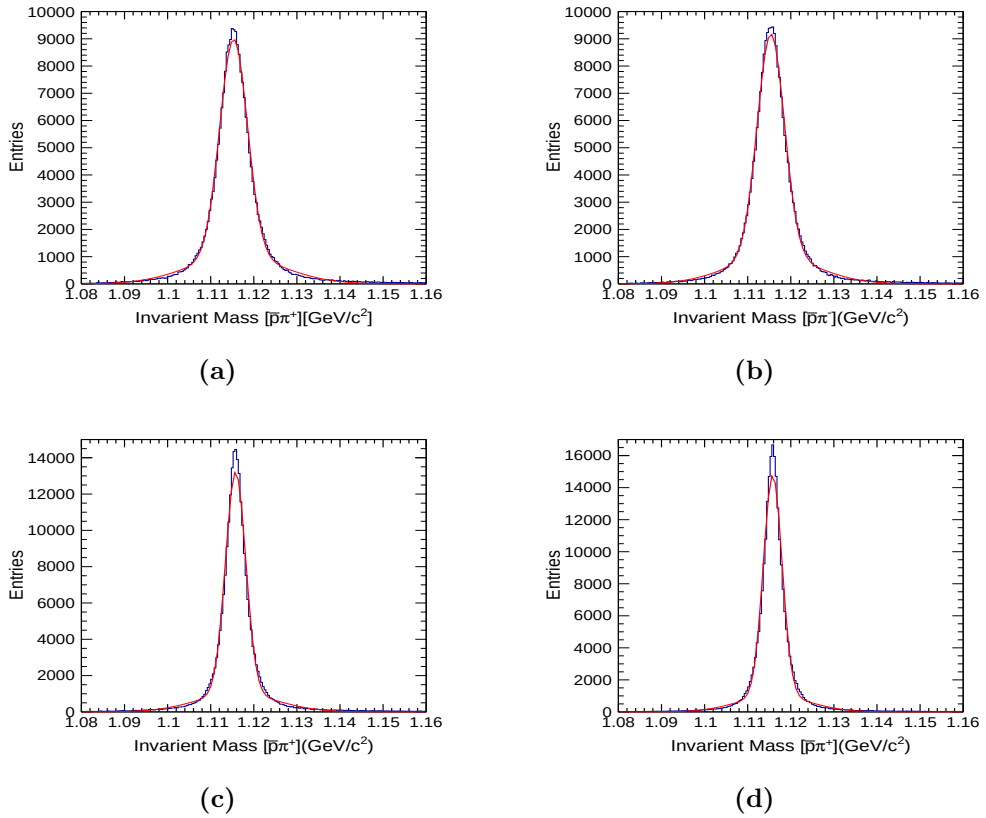

Figure 4.18: Invariant mass of $\bar{\Lambda}$ after kinematic vertex fitting at beam momentum 1.8 GeV/c are shown in panels (a) and (b) without and with Lambda Disks Detector. In panels (c) and (d), similar distributions are shown for $\bar{\Lambda}$ at beam momentum 4.0 GeV/c.

$\mathbf{P}_{beam}$ **[GeV/c]**	**Particle**	**Mean** [GeV/c^2]	σ [GeV/c^2]
1.8	Λ	1.115	0.004
	$\bar{\Lambda}$	1.115	0.003
4.0	Λ	1.115	0.005
	$\bar{\Lambda}$	1.116	0.003
		After Kinematic Vertex Fitting	
1.8	Λ	1.115	0.004
	$\bar{\Lambda}$	1.115	0.003
4.0	Λ	1.116	0.003
	$\bar{\Lambda}$	1.116	0.002

Table 4.3: Reconstructed invariant mass of Λ and $\bar{\Lambda}$ with the LDD at two different beam momenta. Errors are less than 1 MeV/c^2.

It is observed from the results that mass resolutions of Λ and $\bar{\Lambda}$ hy-

perons are not affected after adding the Lambda Disks Detector to $\overline{\text{P}}$ANDA detector setup with available tracking algorithms.

4.2.8 Secondary Vertex Resolution

A vertex fitter tries to find a common point of two tracks from where they have originated. For the decay of Λ and $\bar{\Lambda}$, the PndKinVtxFitter has been used to find the vertex of the p and π^- as well as $\bar{p}$ and π^+ tracks, respectively. Figures 4.19 and 4.20 show the vertex resolutions for Λ at two different beam momenta.

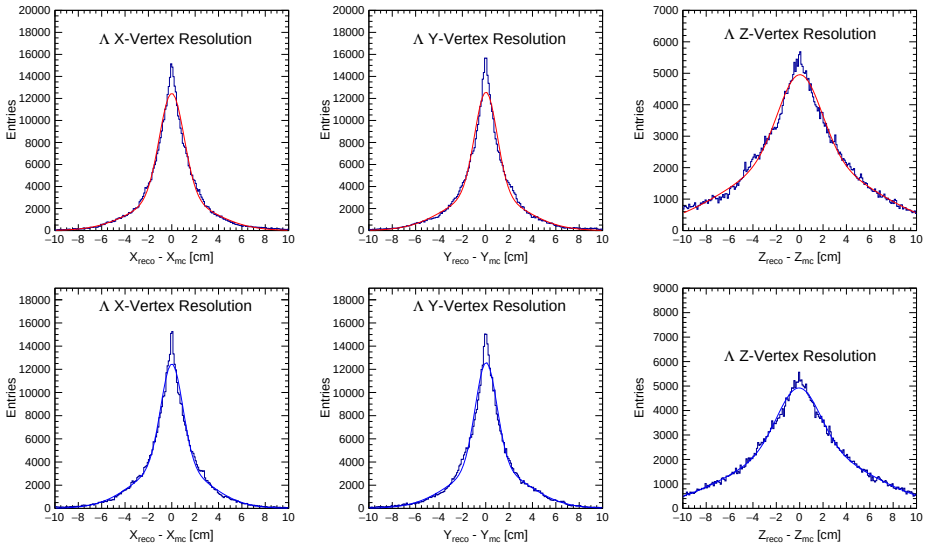

Figure 4.19: Vertex resolutions of Λ at an incoming beam momentum of 1.8 GeV/c without Lambda Disks (upper row) and with Lambda Disks (lower row).

$\bar{\Lambda}$ vertex resolutions are shown in Figures 4.21 and 4.22. The difference between the reconstructed value and the Monte Carlo truth value for the three position cartesian coordinates are calculated without and with Lambda Disks Detector and tabulated in Tables 4.4 and 4.5. The distributions are fitted with double Gaussian function and sigma values of fitted distributions are calculated. The vertex resolutions are not affected after the addition of Lambda Disks Detector to $\overline{\text{P}}$ANDA detector setup.

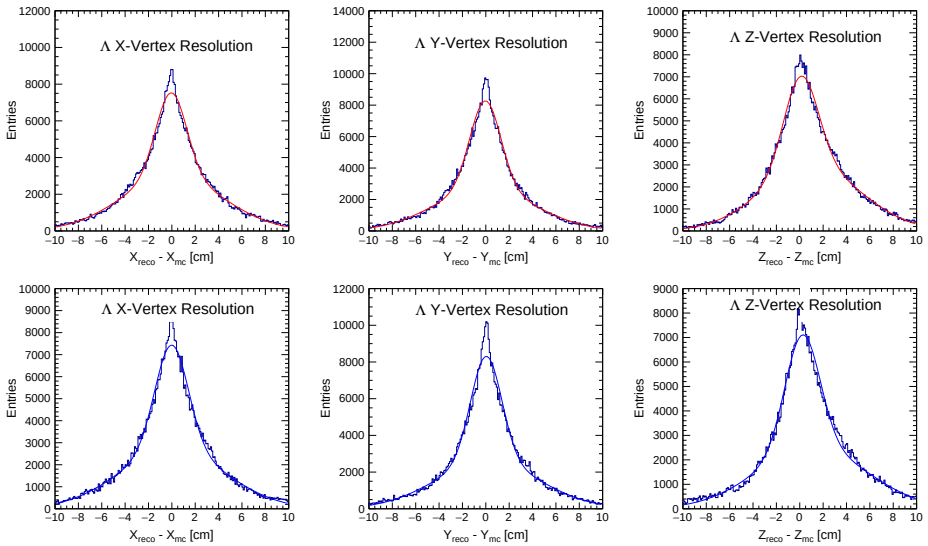

Figure 4.20: Vertex resolutions of Λ at an incoming beam momentum of 4.0 GeV/c without Lambda Disks (upper row) and with Lambda Disks (lower row).

p_{beam} (GeV/c)	Particle Type	σ[cm] $\lvert reco - mc \rvert_x$	σ[cm] $\lvert reco - mc \rvert_y$	σ[cm] $\lvert reco - mc \rvert_z$
1.8	Λ	1.045±0.005	0.951±0.006	1.847±0.022
	$\bar{\Lambda}$	0.972±0.004	1.036±0.005	1.920±0.040
4.0	Λ	1.311±0.011	1.314±0.008	1.468±0.012
	$\bar{\Lambda}$	1.305±0.007	1.044±0.005	2.245±0.350

Table 4.4: Vertex resolution for Λ and $\bar{\Lambda}$ hyperons at beam momentum of 1.8 GeV/c and 4.0 GeV/c without Lambda Disks Detector.

p_{beam} (GeV/c)	Particle Type	σ[cm] $\lvert reco - mc \rvert_x$	σ[cm] $\lvert reco - mc \rvert_y$	σ[cm] $\lvert reco - mc \rvert_z$
1.8	Λ	0.927±0.005	0.916±0.005	1.814±0.020
	$\bar{\Lambda}$	0.954±0.005	0.997±0.004	2.082±0.051
4.0	Λ	1.422±0.010	1.324±0.008	1.468±0.011
	$\bar{\Lambda}$	1.133±0.009	1.012±0.005	2.609±0.506

Table 4.5: Vertex resolution for Λ and $\bar{\Lambda}$ hyperons at beam momentum of 1.8 GeV/c and 4.0 GeV/c with Lambda Disks Detector.

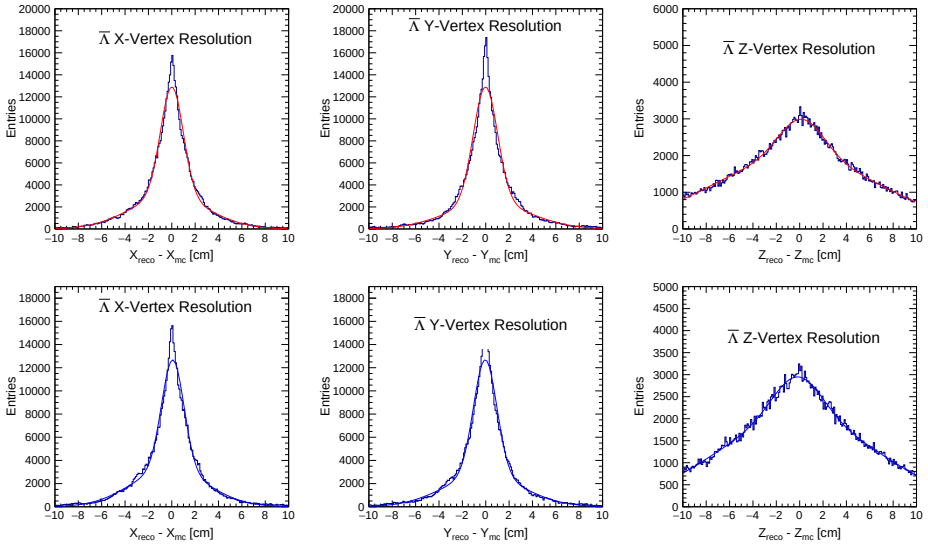

Figure 4.21: Vertex resolutions of $\bar{\Lambda}$ at an incoming beam momentum of 1.8 GeV/c without Lambda Disks (upper row) and with Lambda Disks (lower row).

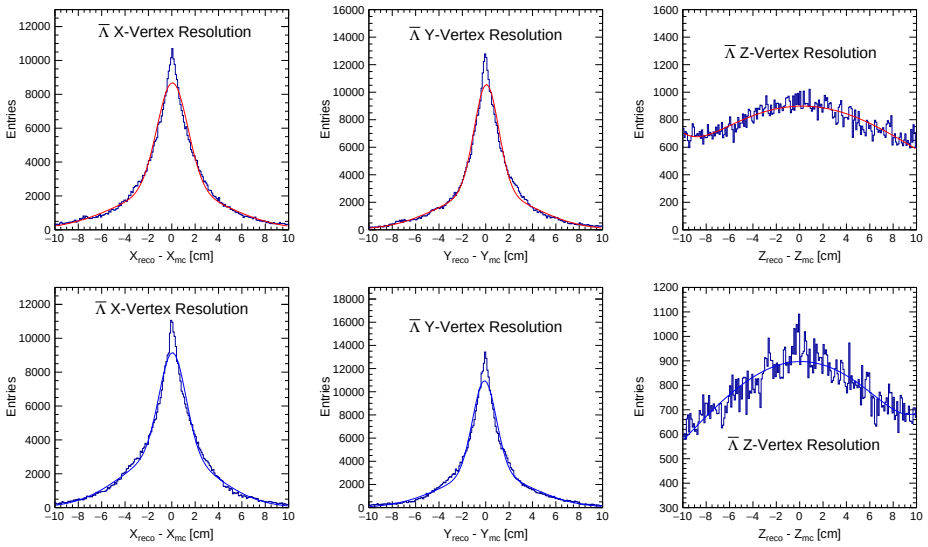

Figure 4.22: Vertex resolutions of $\bar{\Lambda}$ at an incoming beam momentum of 4.0 GeV/c without Lambda Disks (upper row) and with Lambda Disks (lower row).

4.2.9 Momentum Resolution

The momentum resolution of produced hyperons is calculated according to below equation:

$$\frac{\delta p}{p} = \frac{|p_{reco}| - |p_{mc}|}{|p_{mc}|}$$

and distributions are fitted by double Gaussian function. Figures 4.23 and 4.24 show the momentum distributions for Λ at two different beam momenta. Momentum resolutions of $\bar{\Lambda}$ are shown in Figures 4.25 and 4.26. The σ values for the fitted distribution are tabulated in Tables 4.6 and 4.7. We observe that addition of LDD spoils the momentum in the z direction but it remains unchanged in transverse direction.

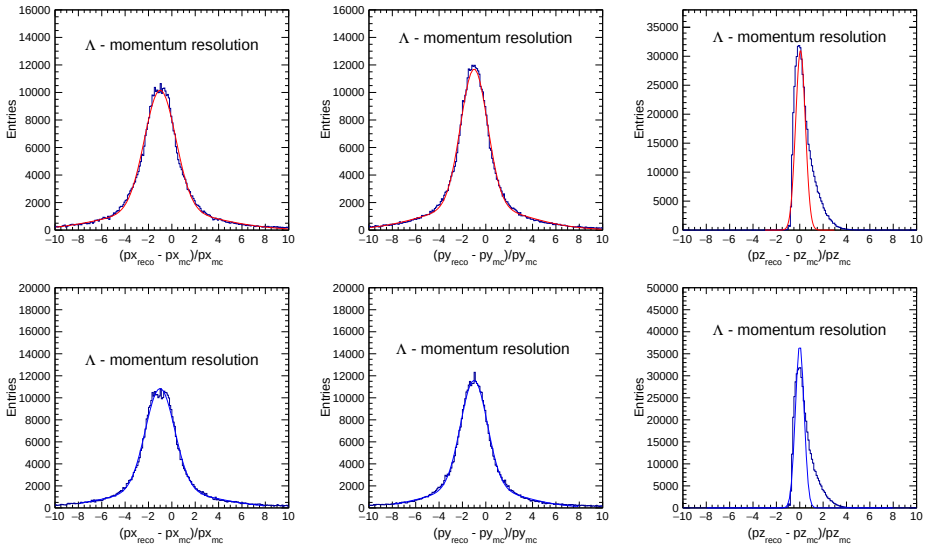

Figure 4.23: Momentum resolutions of Λ at an incoming beam momentum of 1.8 GeV/c without Lambda Disks (upper row) and with Lambda Disks (lower row).

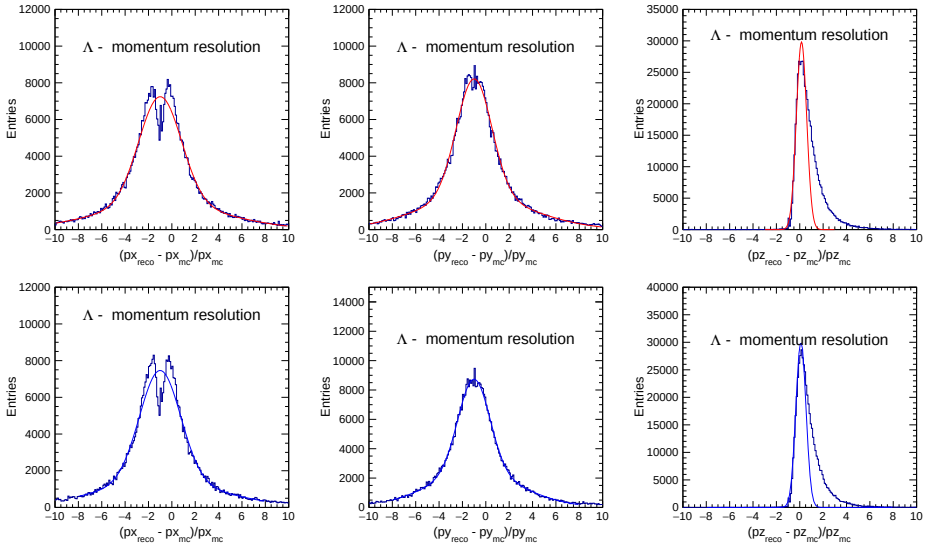

Figure 4.24: Momentum resolutions of Λ at an incoming beam momentum of 4.0 GeV/c without Lambda Disks (upper row) and with Lambda Disks (lower row).

p_{beam} (GeV/c)	Particle	$\sigma[\delta p_x/p_x]$	$\sigma[\delta p_y/p_y]$	$\sigma[\delta p_z/p_z]$
1.8	Λ	1.337±0.004	1.148±0.003	0.413±0.688
	$\bar{\Lambda}$	1.290±0.000	1.146±0.003	0.326±0.000
4.0	Λ	1.313±0.007	1.511±0.006	0.439±0.000
	$\bar{\Lambda}$	1.362±0.005	1.013±0.003	0.119±0.000

Table 4.6: Momentum resolution for Λ and $\bar{\Lambda}$ hyperons at beam momentum of 1.8 GeV/c and 4.0 GeV/c without Lambda Disks Detector.

p_{beam} (GeV/c)	Particle	$\sigma[\delta p_x/p_x]$	$\sigma[\delta p_y/p_y]$	$\sigma[\delta p_z/p_z]$
1.8	Λ	1.251±0.004	1.142±0.004	1.114±2.000
	$\bar{\Lambda}$	1.169±0.004	1.023±0.004	1.861±2.828
4.0	Λ	1.749±0.007	1.355±0.007	1.176±0.424
	$\bar{\Lambda}$	1.216±0.005	0.912±0.003	1.706±8.485

Table 4.7: Momentum resolution for Λ and $\bar{\Lambda}$ hyperons at beam momentum of 1.8 GeV/c and 4.0 GeV/c with Lambda Disks Detector.

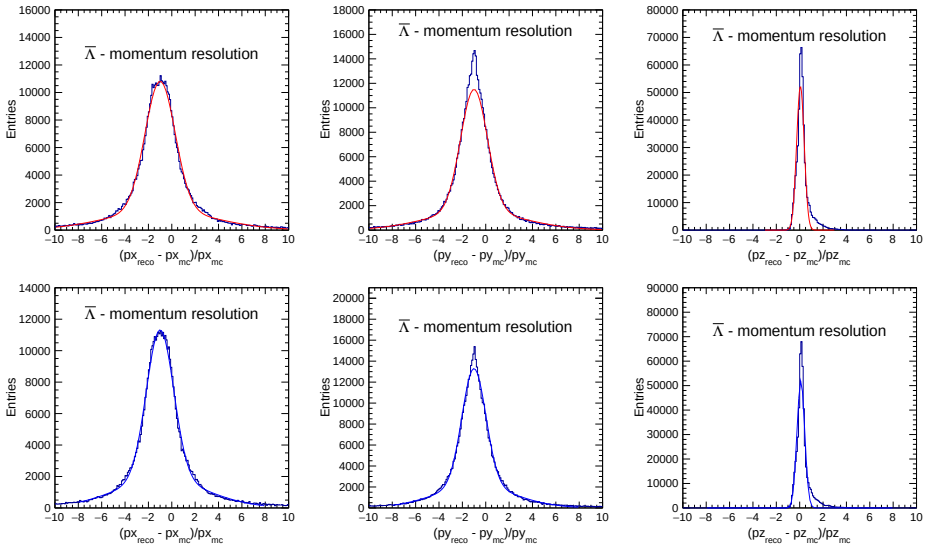

Figure 4.25: Momentum resolutions of $\bar{\Lambda}$ at an incoming beam momentum of 1.8 GeV/c without Lambda Disks (upper row) and with Lambda Disks (lower row).

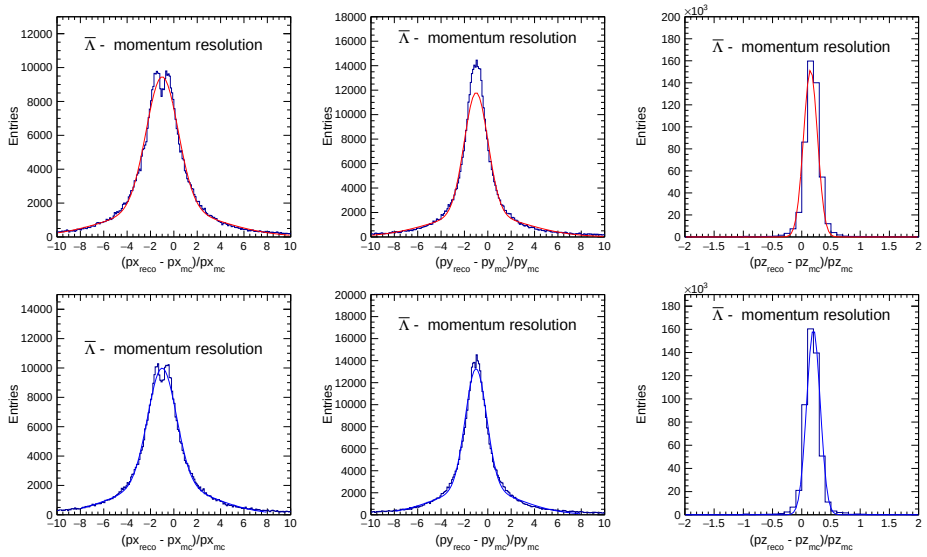

Figure 4.26: Momentum resolutions of $\bar{\Lambda}$ at an incoming beam momentum of 4.0 GeV/c without Lambda Disks (upper row) and with Lambda Disks (lower row).

4.2.10 Reconstruction Efficiency with and without Lambda Disks Detector

The reconstruction efficiency is defined as the overall ratio of the reconstructed events to the generated events. The reconstruction efficiency as a function of generated angle in lab frame of reference of Λ and $\bar{\Lambda}$ at two different beam momenta are studied as shown in Figures 4.27 and 4.28 . In each panel of the figure, we have drawn four plots, in which two are shown for reconstruction efficiency of Λ and $\bar{\Lambda}$ with and without Lambda Disks Detector and in other two are shown for reconstruction efficiency after applying kinematic fitting with and without Lambda Disks Detector. At low beam momentum 1.8 GeV/c, the average reconstruction efficiency for Λ and $\bar{\Lambda}$ with and without Lambda Disks Detector is 42% and 48% respectively. At high beam momentum 4 GeV/c, average reconstruction efficiency with and without Lambda Disks Detector is 25% and 52% for Λ and $\bar{\Lambda}$ respectively.

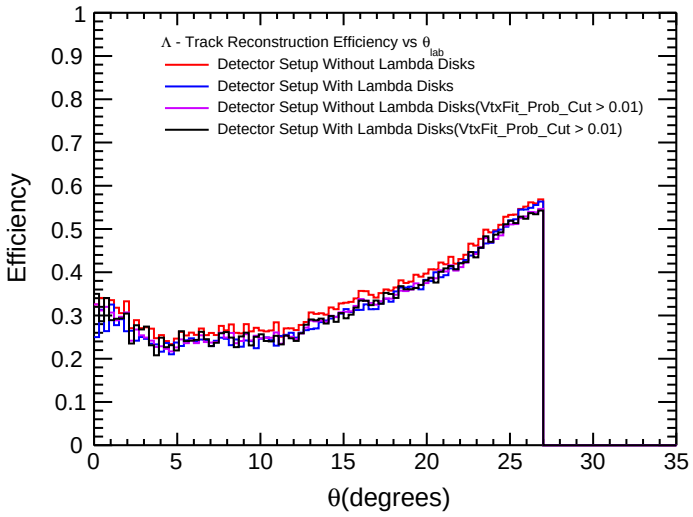

(a)

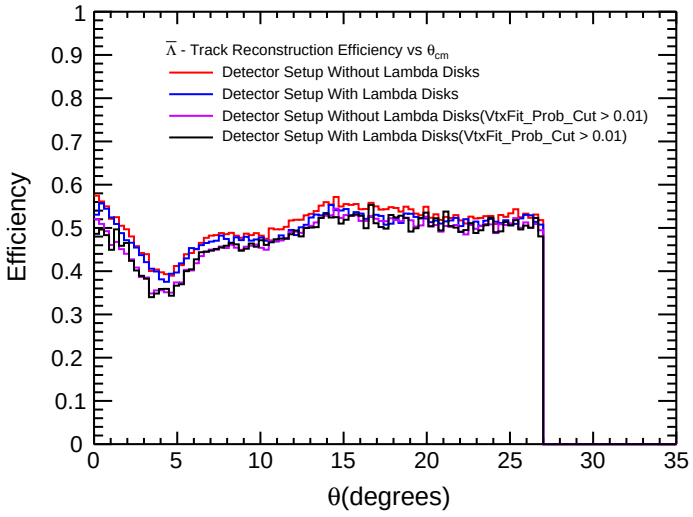

(b)

Figure 4.27: Reconstruction efficiencies of Λ and $\bar{\Lambda}$ at beam momentum 1.8 GeV/c with and without Lambda Disks are shown in panels (a) and (b).

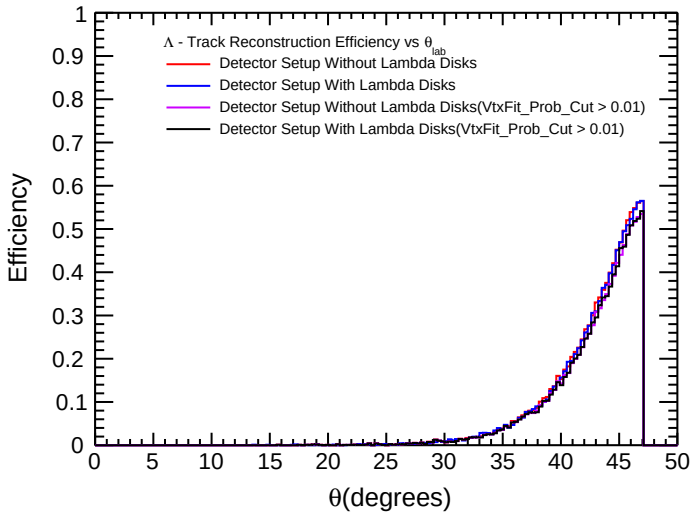

(a)

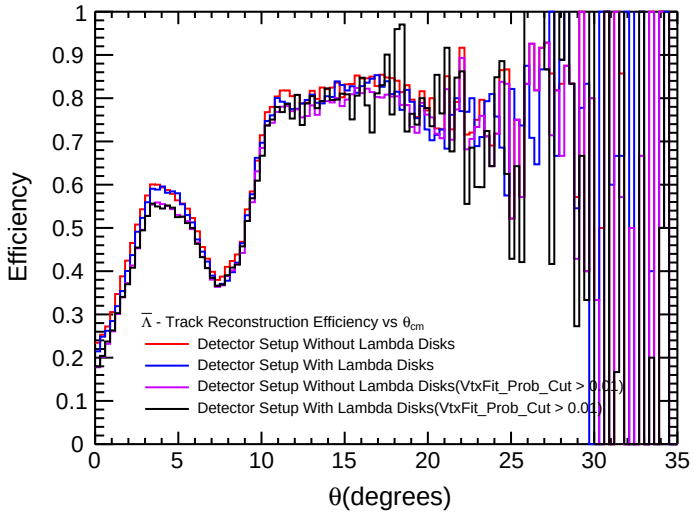

(b)

Figure 4.28: Reconstruction efficiencies of Λ and $\bar{\Lambda}$ at beam momentum 4 GeV/c with and without Lambda Disks are shown in panels (a) and (b).

So Λ reconstruction efficiency decreases and $\bar{\Lambda}$ efficiency increases with increase of beam momentum. Most of the Λ particles travel at larger angle and they are not directed in forward direction so overall reconstruction efficiency for Λ does not increase with increase of beam momentum. $\bar{\Lambda}$ is mostly forward boosted, therefore reconstruction efficiency increases with the increase of beam momentum. Overall $\Lambda\bar{\Lambda}$ reconstruction efficiency is estimated and found to be 28.5% and 20% at beam momentum of 1.8 GeV/c and 4.0 GeV/c, respectively.

4.3 Reconstruction of $\bar{p}p \rightarrow D^{*+}D^{*-}$ Benchmark Channel

The reaction channel $\bar{p}p \rightarrow D^{*+}D^{*-}$ is investigated at an incoming beam momentum of 8 GeV/c which is slightly above the production threshold (7.676 GeV/c). The D^{*+} decays into $D^0\pi^+$ and the D^0 meson again decays into decay pair K^- and π^+. Similarly, D^{*-} decays into $\bar{D^0}\pi^-$ and $\bar{D^0}$ meson further decays into K^+ and π^- as shown in Figure 4.29 as schematic of the reaction. This channel is well reconstructed with the existing central detection system of $\bar{\text{P}}$ANDA detector setup. We are doing reconstruction of this mesonic channel as its reconstruction performance should not be affected after the implementation of Lambda Disks Detector.

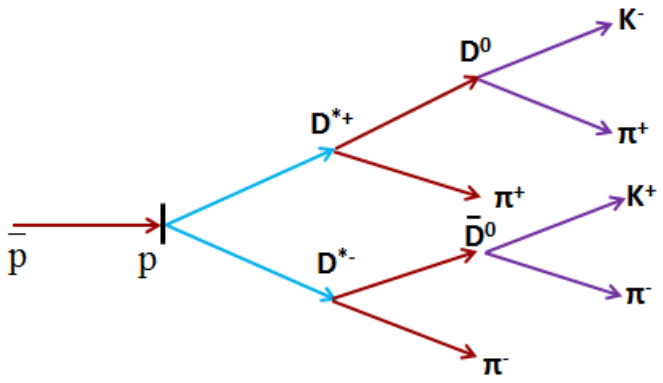

Figure 4.29: Reaction Schematics for the $\bar{p}p \rightarrow D^{*+}D^{*-}$ benchmark channel.

4.3.1 Simulation and Selection Criteria

The trunk version (Rev.No. 28437) of PandaRoot simulation software is used for the simulation and reconstruction of this channel which combines with fairsoft version of march 2015. The full detector setup with the Lambda Disks Detector is included in the full simulation. In the reconstruction also, the ideal track finder algorithm is used to find the tracks and followed by track fitting algorithm. Particle identification used ideal particle identification algorithms to identify charged particles.

4.3.2 Invariant Mass Distribution with and without Lambda Disks Detector

The invariant mass of D^* meson is reconstructed by combining their daughter candidates which is matching with PDG value ($M_{D^*} = 2.010$ GeV/c^2). Invariant mass of D^{*+} is calculated by combining the daughter candidates D^0 and π^+. For the invariant mass of D^{*-}, the daughters $\bar{D^0}$ and π^- are combined. All invariant mass distributions are fitted with double Gaussian function as signal and background both described well by Gaussian function. The invariant mass distributions for the D^* meson are shown in Figure 4.30. The width (σ) of fitted distribution is calculated and values are tabulated in Table 4.8.

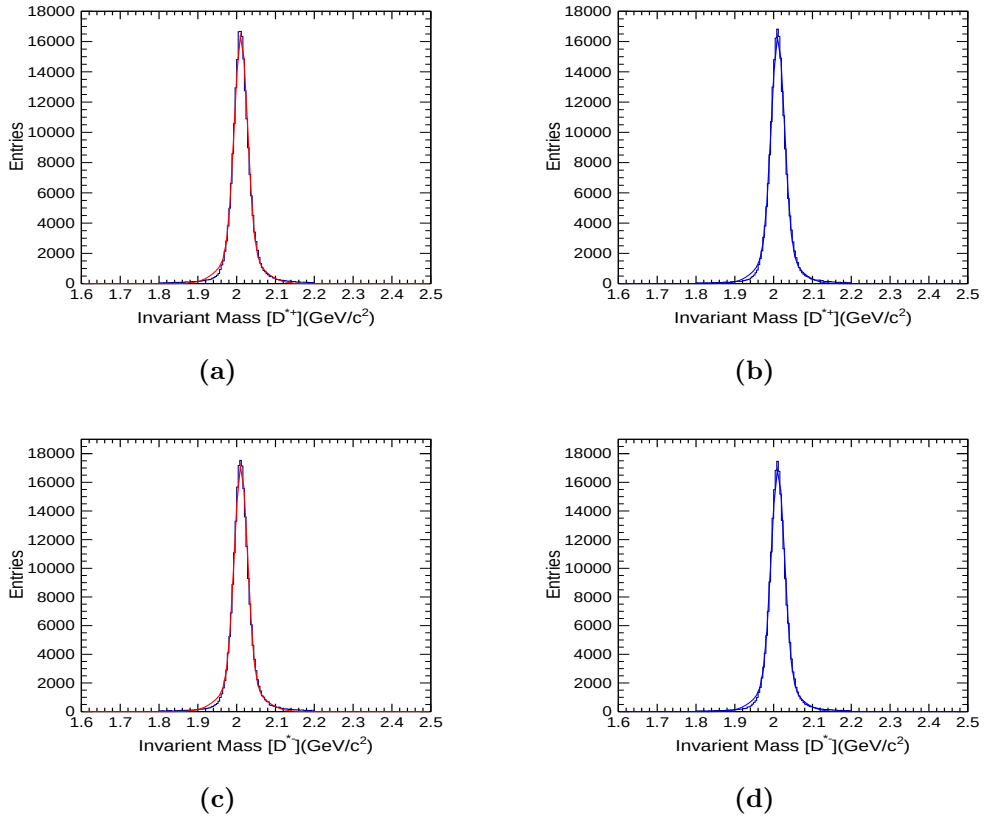

Figure 4.30: Invariant mass distributions of D^{*+} candidates in absence and presence of Lambda Disks Detector with $\overline{\text{P}}$ANDA setup at beam momentum 8 GeV/c are shown in (a) and (b) without and with Lambda Disks Detector. In (c) and (d), invariant mass of D^{*-} are shown without and with Lambda Disks Detector, respectively.

In the same way, the invariant mass of D^0 mesons are calculated. The invariant mass of D^0 meson is 1.864 GeV/c^2. Invariant mass of D^0 is reconstructed by combining K^- and π^+ as they are daughter particles. Similarly, invariant mass of $\bar{D}^0$ is reconstructed by their decay products K^+ and π^-. The invariant mass distributions are fitted with double Gaussian function and width of distribution is measured. The invariant mass distribution for D^0 meson is shown in Figure 4.31. The σ values of fitted distributions are tabulated in Table 4.8.

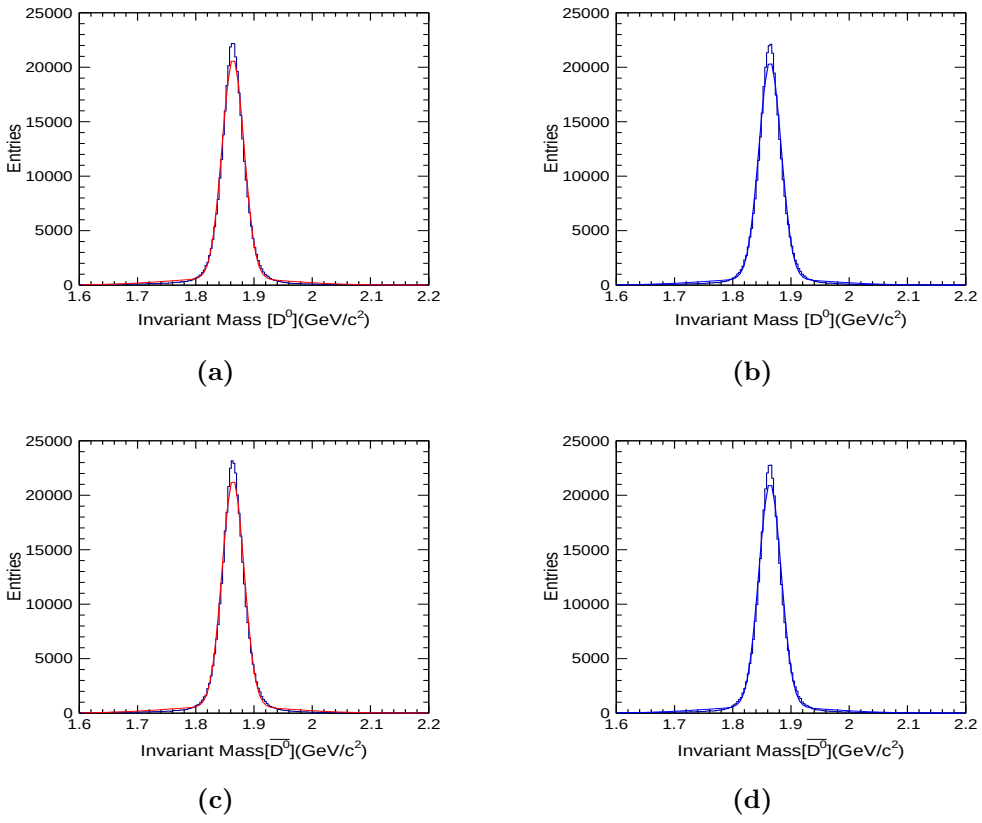

Figure 4.31: Invariant mass distributions of D^0 candidates in absence and presence of Lambda Disks Detector with $\overline{\text{P}}$ANDA setup at beam momentum 8 GeV/c are shown in (a) and (b) without and with Lambda Disks Detector. In (c) and (d), reconstructed invariant mass of $\bar{D}^0$ are shown without and with Lambda Disks Detector, respectively.

Detector Status	P_{beam} [GeV/c]	Particle	Mean [GeV/c^2]	σ [GeV/c^2]
w/o Lambda Disks	8	D^0	1.86	0.019
		$\bar{D}^0$	1.86	0.019
	8	D^{*+}	2.01	0.017
		D^{*-}	2.01	0.017
w/ Lambda Disks	8	D^0	1.86	0.019
		$\bar{D}^0$	1.86	0.019
	8	D^{*+}	2.01	0.017
		D^{*-}	2.01	0.017

Table 4.8: Reconstructed invariant mass without and with Lambda Disks Detector for produced mesons from $\bar{p}p \to D^{*+}D^{*-}$ channel.

4.3.3 Reconstruction Efficiency with and without Lambda Disks Detector

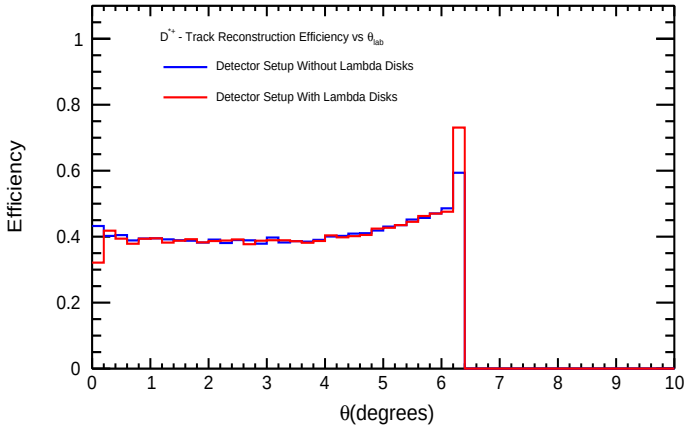

(a)

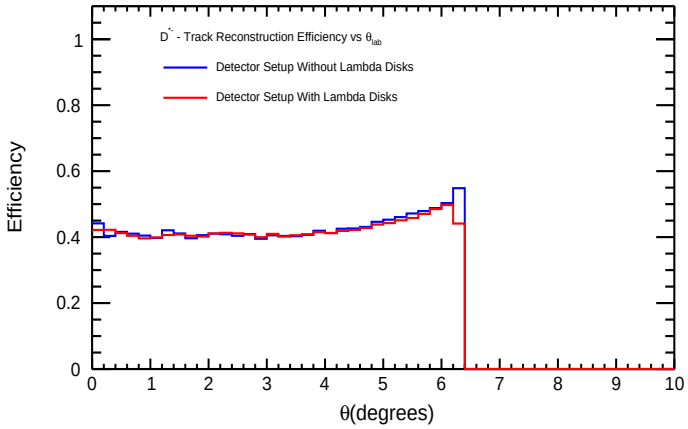

(b)

Figure 4.32: Reconstruction efficiencies of D^{*+} and D^{*-} mesons with and without Lambda Disks Detector at beam momentum of 8.0 GeV/c are shown in panels (a) and (b).

The track reconstruction efficiency is estimated and defined as given in subsection 4.2.10.

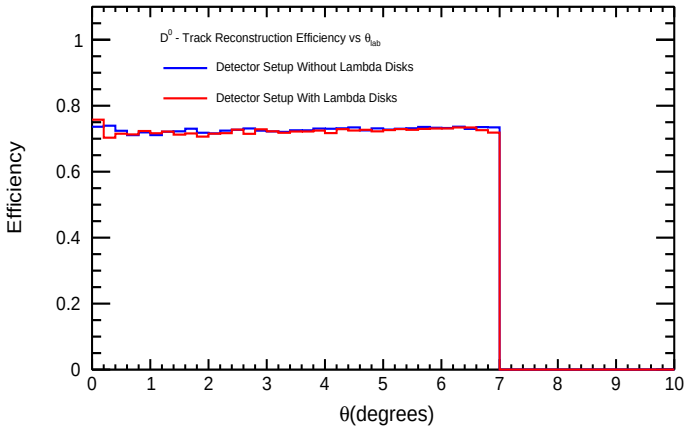

(a)

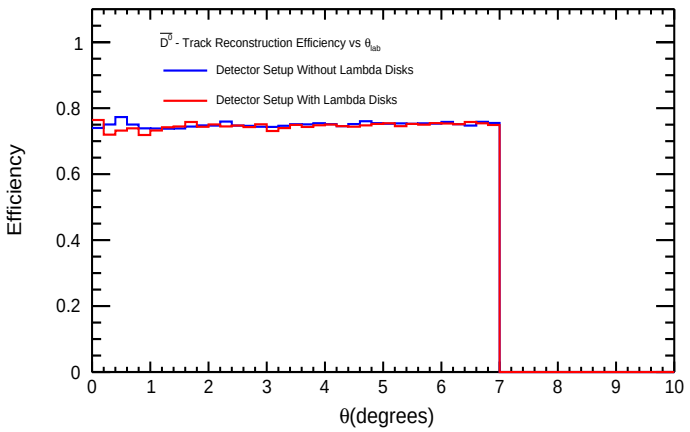

(b)

Figure 4.33: Reconstruction efficiencies of D^0 and $\bar{D}^0$ mesons with and without Lambda Disks Detector at beam momentum of 8.0 GeV/c are shown in panels (a) and (b).

Monte Carlo Truth match is performed to check whether reconstructed data resembles the original one created by the event generator. This match is important for the precise measurement of reconstruction efficiency and resolution. The final state particles from the $\bar{p}p \rightarrow D^{*+}D^{*-}$ reaction are taken and combined to reconstruct the D mesons for the efficiency calculation. The overall reconstruction efficiency is calculated for the produced mesons and are shown in the Figures 4.32 and 4.33 and values in percentage tabulated in Table 4.9.

In Figures 4.32a and 4.32b are shown the reconstruction efficiency for D^{*+} and D^{*-} meson, respectively. The overall reconstruction efficiency is same for these mesons with and without the Lambda Disks detector. In Figures 4.33a and 4.33b reconstruction efficiency are shown for the neutral D mesons and observed that the overall reconstruction efficiency is same in absence and presence of Lambda Disks Detector. It is concluded that the implementation of Lambda Disks Detector does not affect the reconstruction efficiency and resolution of the $\bar{p}p \to D^{*+}D^{*-}$ reaction.

$\mathbf{P}_{beam}$**[GeV/c]**	**Particle**	**Avg.Reco. Effi.[%]**
8.0	D^0	75
	$\bar{D}^0$	75
8.0	D^{*+}	40
	D^{*-}	40

Table 4.9: Overall reconstruction efficiency without and with Lambda Disks Detector for produced mesons from $\bar{p}p \to D^{*+}D^{*-}$ channel.

4.4 Reconstruction of $\bar{p}p \to J/\psi\pi^+\pi^-$ Benchmark Channel

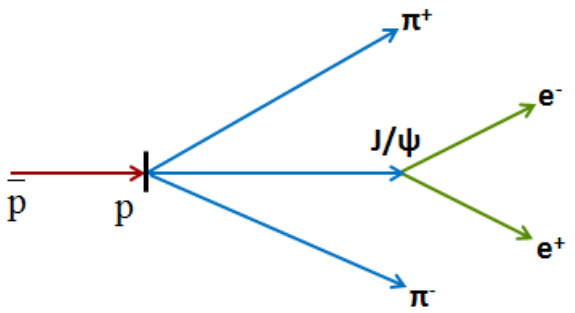

Figure 4.34: Reaction Schematics for the $\bar{p}p \to J/\psi\pi^+\pi^-$ benchmark channel.

Another channel $\bar{p}p \to J/\psi\pi^+\pi^-$ is investigated at an incoming beam momentum of 6 GeV/c which is just above the production threshold (5.135 GeV/c). The J/ψ decays into e^+ and e^- as shown in Figure 4.34 as a

schematics of this reaction. This channel is also well reconstructed with the existing central detection system of $\overline{\text{P}}$ANDA setup and very important for the charmonium sector of $\overline{\text{P}}$ANDA physics program. We are doing reconstruction of this mesonic channel to confirm whether reconstruction performance are either affected or not after the implementation of Lambda Disks Detector. The invariant mass resolution and reconstruction efficiency of J/ψ meson are estimated in order to do that.

4.4.1 Invariant Mass Distribution with and without Lambda Disks Detector

The invariant mass of J/ψ meson is reconstructed by combining their daughter candidates and it is good agreement with the PDG value (3.096 GeV/c^2). Invariant mass of J/ψ is calculated by combining the daughter candidates e^+ and e^-. The invariant mass distributions are fitted with double Gaussian function as signal and background both looks Gaussian in nature. The invariant mass distribution for the J/ψ meson is shown in Figure 4.35. The sigma (σ) of fitted distribution is calculated and values are tabulated in Table 4.10.

Detector Status	**P$_{beam}$ [GeV/c]**	**Particle**	**Mean [GeV/c^2]**	**σ [GeV/c^2]**
w/o Lambda Disks	6	J/ψ	3.086	0.052
w/ Lambda Disks	6	J/ψ	3.085	0.053

Table 4.10: Reconstructed invariant mass without and with Lambda Disks Detector for produced mesons from $\bar{p}p \to J/\psi\pi^+\pi^-$ channel.

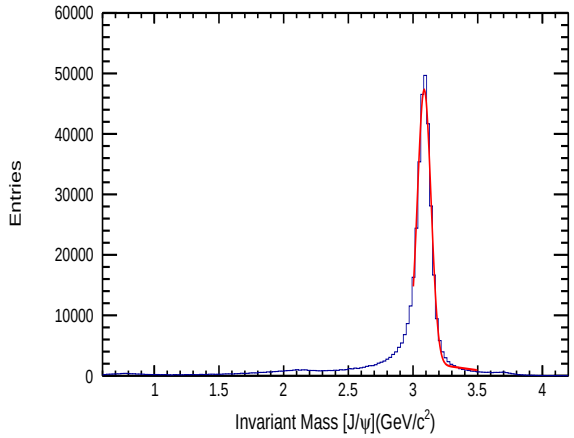

(a)

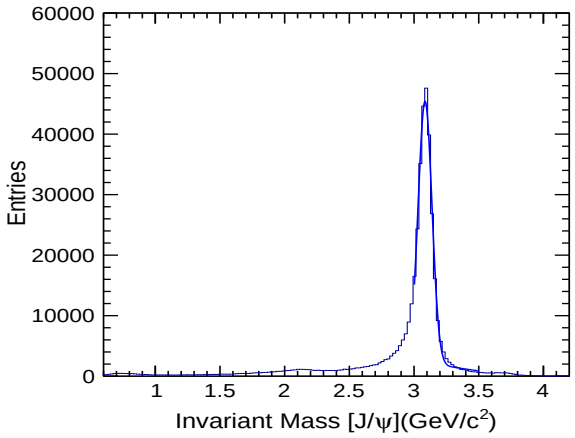

(b)

Figure 4.35: Reconstructed invariant mass of J/ψ at beam momentum of 6.0 GeV/c are shown in (a) and (b) without and with Lambda Disks Detector.

4.4.2 Reconstruction Efficiency with and without Lambda Disks Detector

The track reconstruction efficiency is defined as described in subsection 4.3.3. Monte Carlo Truth match is performed to check whether reconstructed data resembles the original one created by the event generator. Final state particles electron and positron from the $\bar{p}p \rightarrow J/\psi\pi^+\pi^-$ reaction are combined to reconstruct the J/ψ meson for the efficiency calculation. The overall reconstruction efficiency is calculated for the J/ψ particle and is shown in the Figure 4.36.

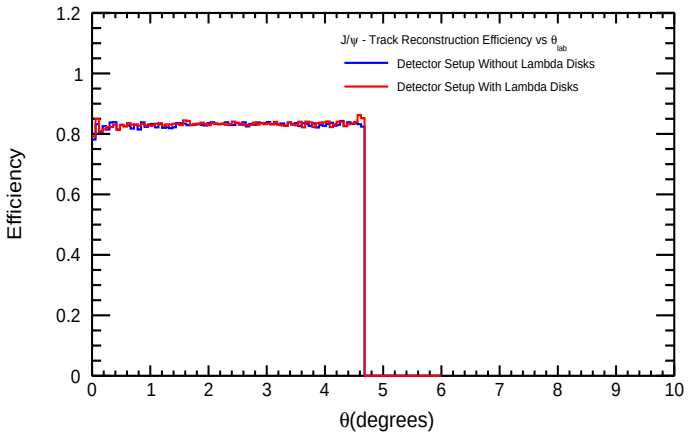

Figure 4.36: Reconstructed efficiency of J/ψ at beam momentum of 6.0 GeV/c is shown with and without Lambda Disks.

Detector Status	$\mathbf{P}_{beam}$**[GeV/c]**	**Particle**	**Avg.Reco. Effi.**[%]
w/o Lambda Disks	6.0	J/ψ	84
w/ Lambda Disks	6.0	J/ψ	84

Table 4.11: Overall reconstruction efficiency without and with Lambda Disks Detector for produced mesons from $\bar{p}p \to J/\psi\pi^+\pi^-$ channel.

Efficiency values in percentage tabulated in Table 4.11. It is found that the average reconstruction efficiency is same for J/ψ meson with and without the Lambda Disks detector. From the results, it is concluded that the implementation of Lambda Disks Detector does not affect the reconstruction efficiency and resolution of the $\bar{p}p \to J/\psi\pi^+\pi^-$ reaction.

Chapter 5

Characterization of Double Sided Silicon Strip Detectors

Silicon strip detectors are often used as tracking detectors in particle physics experiments all over the world. Each strip of the detector provides a one-dimensional spatial information of charged particle tracks traversing the detector. By combining the information of two fired strips which have certain stereo angle between them, one can reconstruct a 3-D point. Either one uses two single sided strip detectors placed back to back towards each other or one uses a sensor where both the front and the back side are structured. The later approach has the advantage that the material budget is reduced and the same amount of charge is seen on the front and backside. Therefore, the $\overline{\text{P}}$ANDA Lambda Disks Detector (LDD) prefers to use double sided silicon strip sensors. This chapter describes the results obtained in the characterization of double sided silicon strip sensors using different biasing methods. Sensor characterization is important to determine the quality and characteristics before they are put into operation. The most reliable quality parameter is the leakage current of the sensor which one can compare with the measured value of the manufacturer before the sensors have been cut out from the wafers. Also the measurement of the bias voltage is important at which the sensors are fully depleted. In order to provide a constant supply voltage to the readout electronics, DC-to-DC converters are used. A DC-to-DC converter is an electronic device which converts one level of voltage to another level. Quality assurance tests of DC-to-DC converters are done to verify their quality and performance.

5.1 Double Sided Micro Strip Trapezoidal Sensors with two Different Biasing Methods

The characterization of two types of trapezoidal shaped strip sensors is performed using two different biasing methods. One biasing method is known as punch through biasing and another method is called poly-silicon resistor biasing. Both sides of a sensor, p side as well as n side have a bias ring surrounding all strips near to the sensor edges. This bias ring is p^+ doped on the p side and n^+ doped on the n side. Biasing voltage to the sensor is provided through these bias rings. Bias rings of p side are surrounded by the guard rings which work as a shield for the conducting sensor edges from the depletion voltage. To deplete the sensor it has to be put onto a fixed depletion voltage which has to be applied to the top and bottom side of the sensor. A direct connection to the strip is not possible otherwise it would be impossible to see a signal. Therefore, one needs a separation between the applied voltage and the strips.

5.1.1 Punch Through Method

In this biasing technique, the bias ring is not directly connected to the implanted strips. There is a small gap in between the implanted strips and the bias ring. In this gap, n^- doped substrate is placed which creates a potential across the junction before the connections of strips to the bias ring. When the reverse bias voltage is provided to the bias ring, the depletion zone grows towards the strip implants. Once it touches the strips at the punch through voltage the strip potential follows the bias voltage minus the punch through voltage.

5.1.2 Poly-Silicon Resistor Method

In this method of biasing, a resistor is placed between each strip and the bias ring. Each individual strip can be kept at the desired potential through the biased resistor and this resistor prevents the signal sharing between the strips through the bias line. As these resistors are made out of poly-silicon material, this method is called poly-silicon resistor biasing method. Punch through as well as poly-silicon structures can be viewed as shown in Figures 5.1a and 5.1b.

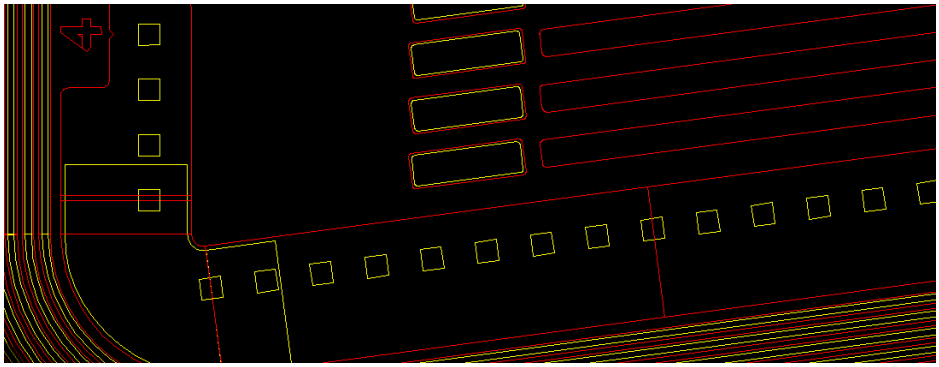

(a) A corner part of a trapezoidal strip sensor from p-side. This layout was designed with punch through method.

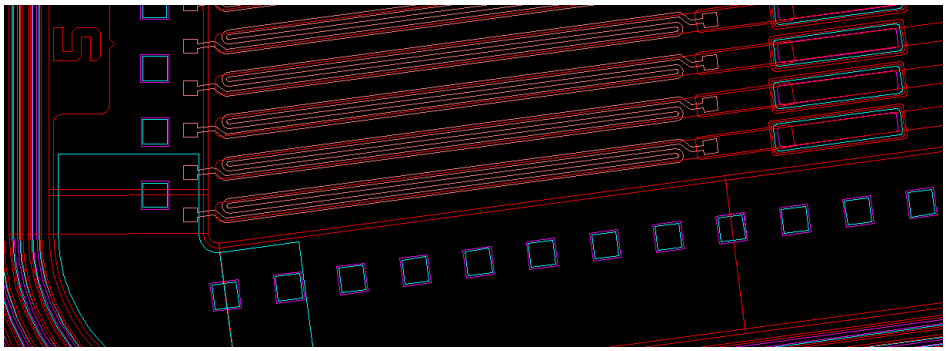

(b) Corner segment of a trapezoidal strip sensor from p-side. The snake like shaped structures in pink colour are the poly-silicon resistors connecting the strips to the bias ring.

Figure 5.1: Corner segments of the p-side for two sensors with different biasing. Parts of the p side strips, p side bias ring, and guard rings can be seen. Figures are adopted from Ref. [56].

5.2 Characterization of Trapezoidal Sensors with two Different Measurement Setups

Two measurement setups are used to perform the measurements on the sensors. In one measurement setup a probe station is used to perform measurements on the whole sensor. In the second setup a dedicated test board is used to perform measurements on the whole sensor as well as on individual strips of the sensor.

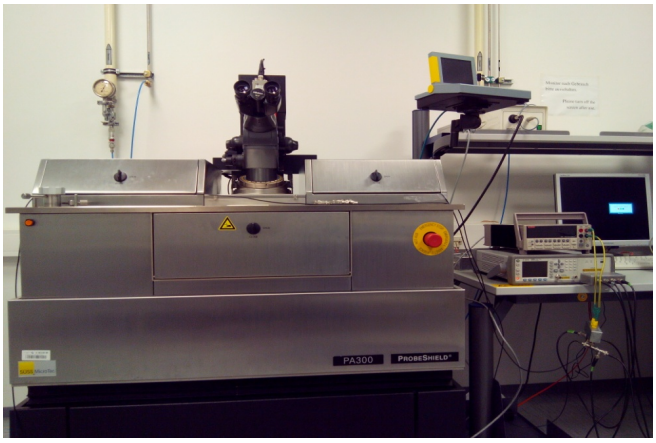

(a) Model PA 300, probestation.

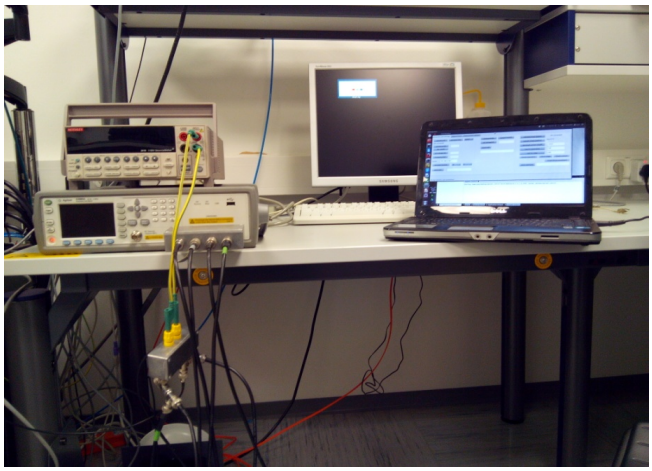

(b) A picture of source meter, LCR meter, PC with video tracker system.

Figure 5.2: A picture of probestation with the other measurement components.

5.2.1 Probestation

A picture of a probe station with full measurement setup is shown in Figure 5.2. The probe station has a holding table called chuck where a sensor can be placed. The chuck can be remotely handled through a computer interface and it is possible to change its position in all three directions and additionally rotate it around the vertical axis. The sensor is fixed on the chuck by a vacuum which is applied through holes in the chuck. The contacts between sensor and measurement setup are made with prober needles. These prober needles are hold by metallic stands. Maximum sixteen prober needles can be mounted onto the probe-station. Two needles are used to measure the whole sensor during these studies.

A personal computer is connected to the probe station to control it. The probe station has a combination of microscope and camera to view the prober needles position and place them on the sensor. The connections made by prober needles on the p-side and the n-side of the sensor to take measurements are shown in Figure 5.3.

5.2.2 Characterization with Probe Station

When a sensor is kept on a chuck inside the probe station, it is not possible to make a contact with the bottom side of the sensor. The only way to provide the bias voltage to the sensor for the measurement by contacting its edge on the top. The sensor edge is in direct contact with the n^- doped substrate so it can establish contact to the n-side of the sensor by leaving the p-side of the sensor accessible from the top. Thus, sensors can be biased by one needle contacting the p-side bias ring and another are contacting the n-side by edge contact. Ten trapezoidal sensors were biased by the punch through method. To characterize a sensor one has to measure two important observables, leakage current and capacitance of the whole sensor.

Leakage current measurement: Leakage current is the current which flows due to minority charge carriers which are thermally generated in the junction. This current is generally small and measured in micro-

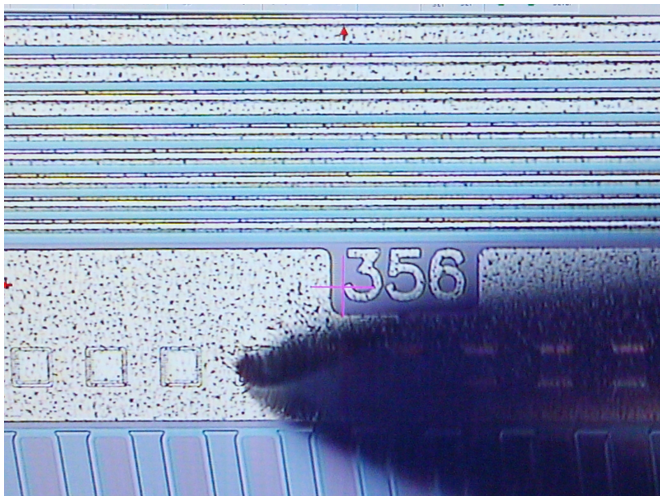

(a)

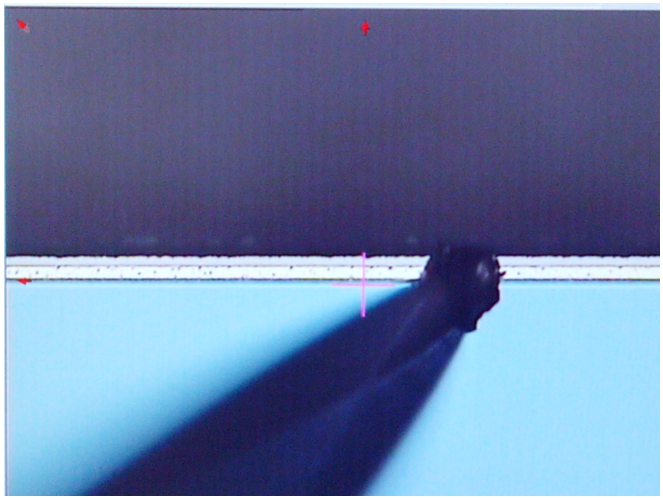

(b)

Figure 5.3: The corners of the p-side and the n-side of a sensor are shown in panels (a) and (b) with the prober needles contacting the pads viewed with the video tracker from the probe station PC.

amperes. Figure 5.4 shows the leakage current of eight sensors which is comparable to the measured values of the leakage current by the manufacturer company CiS. In upper Figure 5.4a, the leakage current variations with the bias voltages are shown for four sensors from wafer no. 321589. The leakage current for these sensors are observed near about 2 μA before the breakdown voltage. In lower Figure 5.4b, leakage currents are shown for four different sensors which are taken from another wafer (322635). The breakthrough voltage for all sensors is above 200V varying between 220V and 270V. The current below breakthrough is between 1μA and 3μA for the first wafer and (2-4)μA for the second. The leakage current is dependent

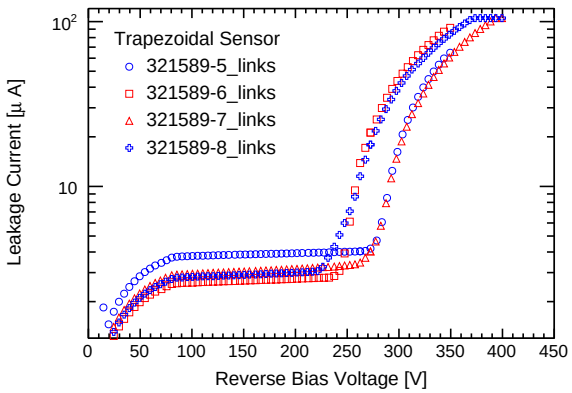

(a) Leakage current of sensors from wafer no. 321589

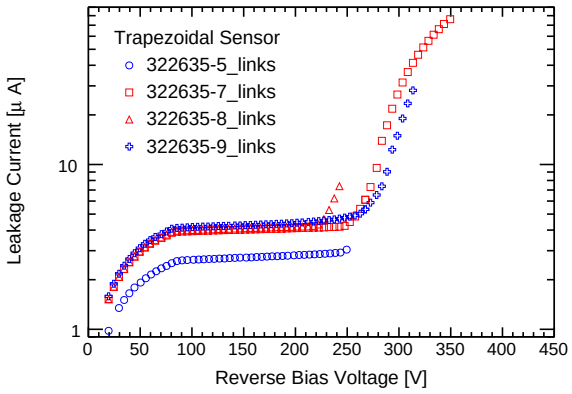

(b) Leakage current of sensors from wafer no. 322635

Figure 5.4: Leakage currents of sensors from wafer no. 321589 are shown in panel (a) and panel (b) shows the same from wafer no. 322635 with measured with the probe station.

on the sensor temperature at the time of the measurement as it is proportional to the number of minority charge carriers (n_i) which are thermally generated [57].

$$I_{leakage} \propto n_i \propto T^{1.5} \exp(-\frac{E_{g0}}{2kT}),$$

where E_{g0} is the energy band gap at T = 0 K. Depending upon the dopant concentration, the number of thermally generated carriers can exceed the number of dopant-generated carriers.

Capacitance Measurement: Capacitance measurements are performed by contacting p-side and the n-side of the sensor with an LCR meter. Capacitance measurements are important to determine the voltage at which the full depletion of the sensor is reached.

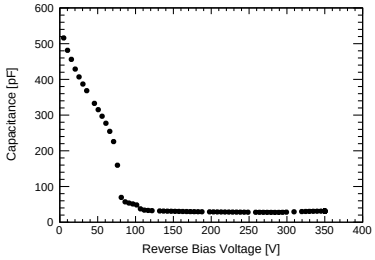

(a) Punch through biased sensor no. 321589-5

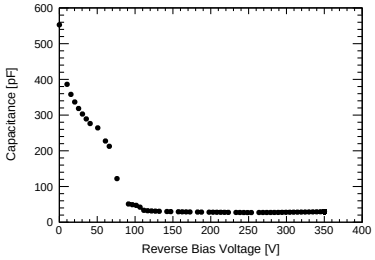

(b) Punch through biased sensor no. 321589-6

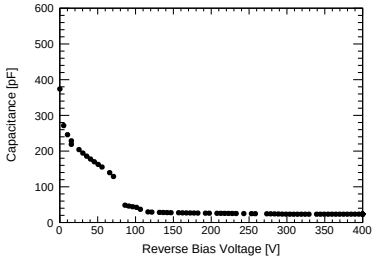

(c) Punch through biased sensor no. 321589-7

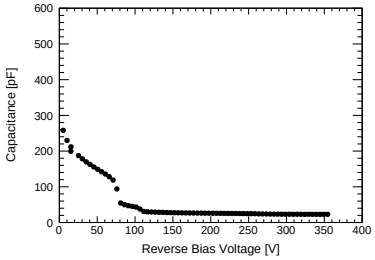

(d) Punch through biased sensor no. 321589-8

Figure 5.5: C-V characterstics for the sensors from wafer no.- 321589.

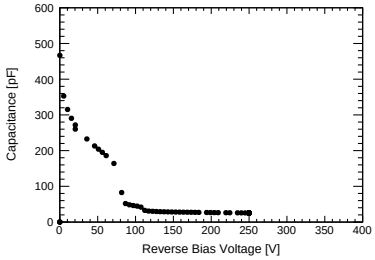

(a) Punch through biased sensor no. 322625-5

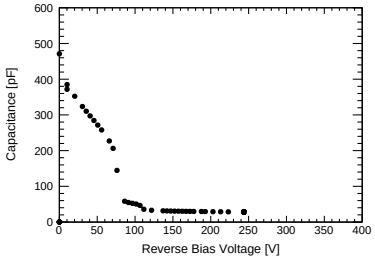

(b) Punch through biased sensor no. 322625-7

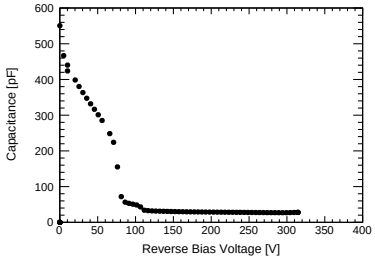

(c) Punch through biased sensor no. 322625-8

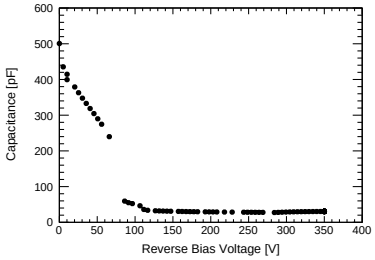

(d) Punch through biased sensor no. 322625-9

Figure 5.6: C-V characterstics for the sensors from wafer no.- 322625.

One needs to calibrate the LCR meter every time before taking the measurement as it will ignore the contribution of cables and needles to the total capacitance of the sensor. The capacitance of the sensor drops with rising biasing voltage comparable with a plate capacitor with using distances of the plates. When the depleted zone of a sensor covers the full volume the capacitance does not drop further. The voltage needed at this point is called depletion voltage. In Figures 5.5 and 5.6, C-V behaviour of eight sensors which used punch through biasing shows the depletion voltage of the sensors. All measurements are performed with 200 kHz frequency of LCR meter and we observed that full depletion voltage of all eight sensors around 100 - 120V.

5.2.3 Probe card: A Dedicated Test Board

The probe card, a dedicated test board, is used as another measurement setup. It is produced for the characterization of a single sensor and allows to contact all strips on the top and the bottom side. In addition single strip can be accessed individually. However, once the sensor is bonded to the board, it can not be used for another measurement setup. Also measurement points for individual strip once fixed to the board can not be changed later. A probe card measurement setup consists of a LCR meter and a source meter which are controlled by the measurement software from a computer. The communication between the computer and the LCR meter are done via an ethernet connection. A picture of the dedicated test board with a sensor is shown in Figure 5.7.

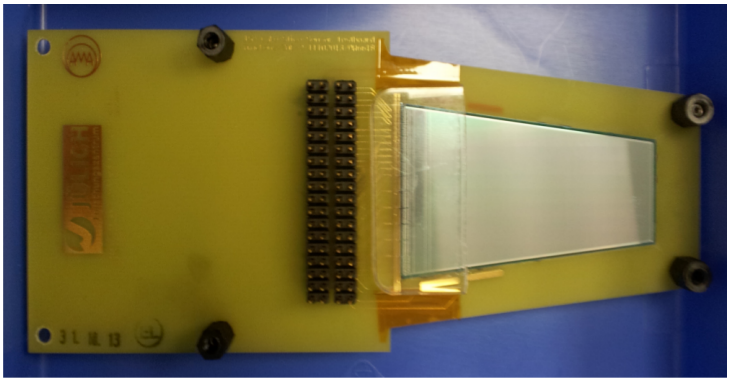

Figure 5.7: A picture of a dedicated test board with the sensor. Figure is taken from the Ref. [56].

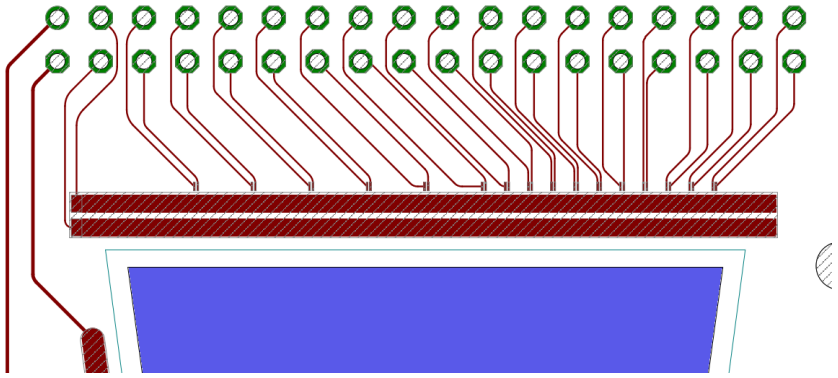

Figure 5.8: A section of test board with the strips. Figure is taken from the Ref. [56].

5.2.4 Characterization with Dedicated Test Board

With the dedicated test board, one can perform measurements on the whole sensor or on individual strips. The layout of the section of the test board is shown in Figure 5.8. Measurements on the trapezoidal sensors which are biased by poly-silicon resistors are performed by this test board.

Leakage Current Measurement: The leakage current of a whole sensor measured by the dedicated test board is shown in Figure 5.9a which is near about 2μA and is in good agreement with the manufacturer. Leakage current of every second strip from n-side and p-side are also measured and found to be less than 2μA as shown in Figures 5.9b and 5.9c. The break through voltage for individual strips is about 100V much lower than for the whole sensor with a large variation from strip to strip.

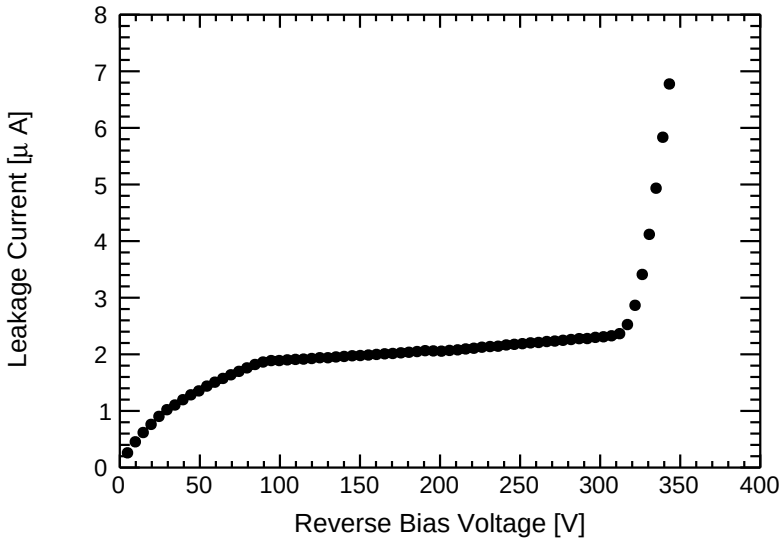

(a) Leakage current of the whole sensor.

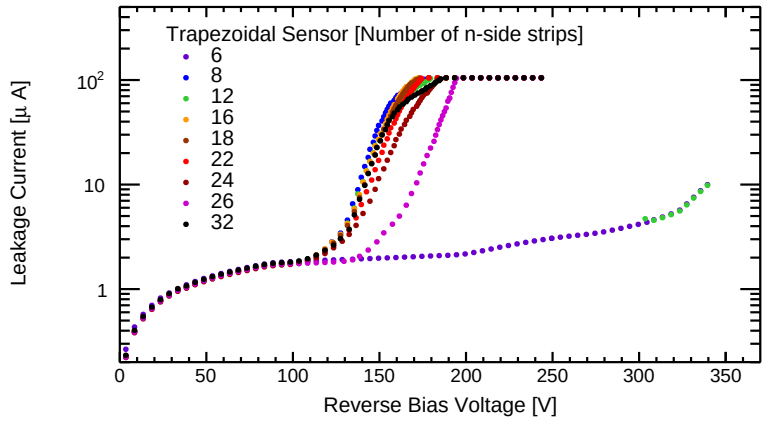

(b) Leakage current of every second strip of n-side.

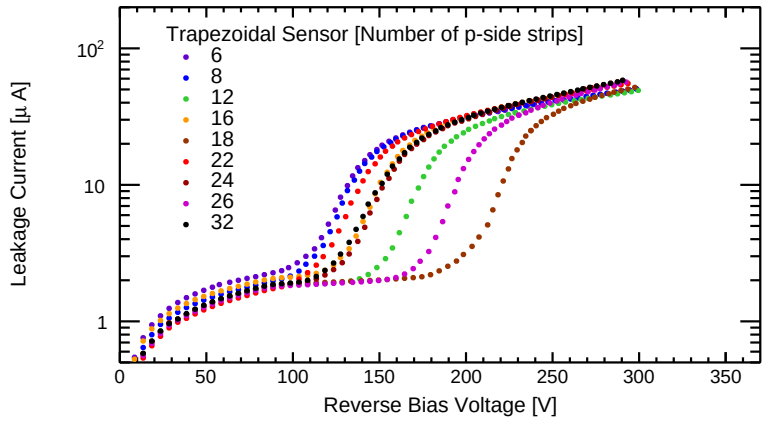

(c) Leakage current of every second strip of p-side.

Figure 5.9: Leakage current of a whole sensor is shown in panel (a). In panels (b) and (c) leakage currents are shown for the individual strips of n-side and p-side of the same sensor. Measurements are taken with the test board.

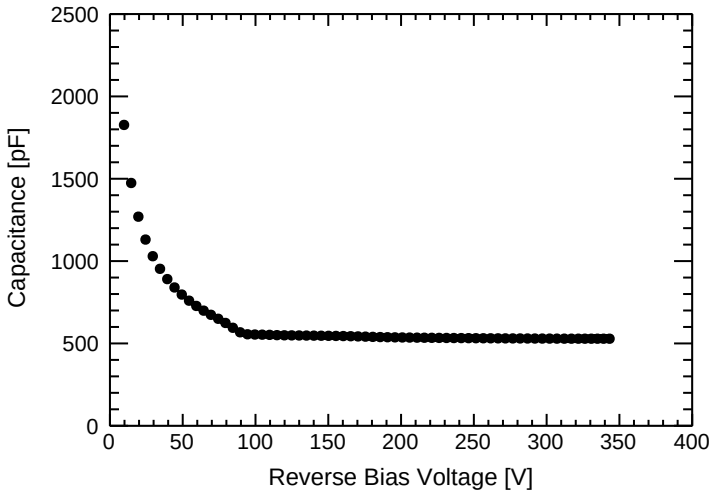

(a) Capacitance of the whole sensor.

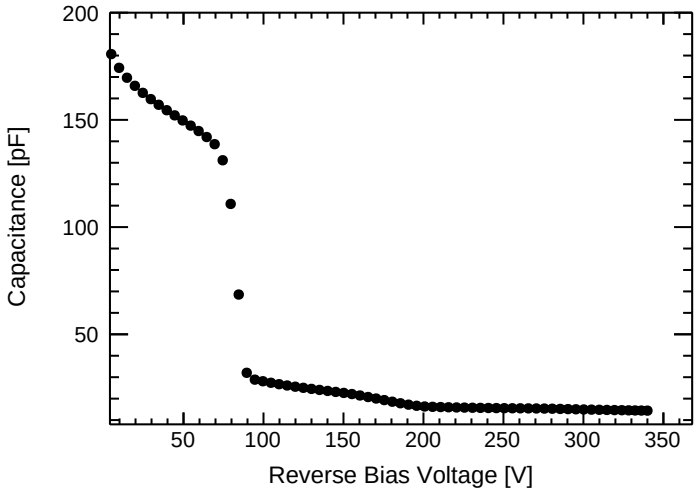

(b) Capacitance of a single strip of n-side.

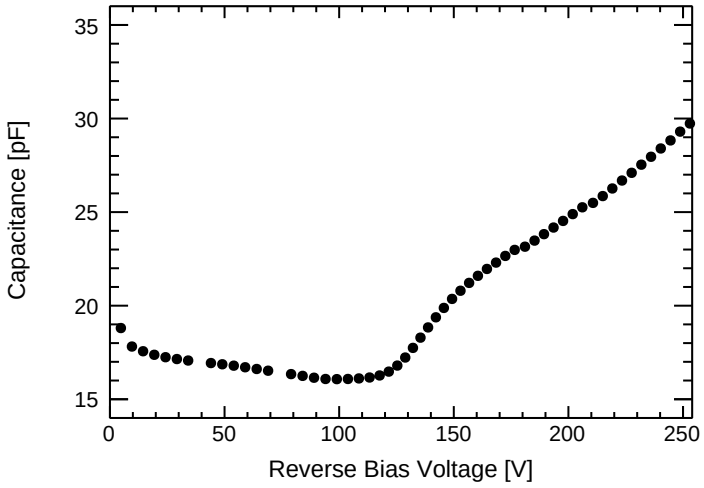

(c) Capacitance of a single strip of p-side.

Figure 5.10: Capacitance of the whole sensor is shown in panel (a). In panels (b) and (c), CV characteristics are shown for single strips of the n-side and the p-side of the same sensor. Measurements are taken with the test board.

One can see a break through about 320V which is significantly higher than the values at probe station. Below the breakthrough voltage the leakage current is stable at 2μA.

Capacitance Measurement: The capacitance of a sensor is measured by connecting p and n side of a sensor to an LCR meter via the test board setup. The C-V curve is shown in Figure 5.10a and the depletion voltage for this particular sensor is found to be close to 100V. C-V characteristics of both side strips (p-side and n-side) are also measured by the test board as shown in Figures 5.10b and 5.10c. It is found that n-side strip from this sensor are depleted at bias voltage of 200V while same strip from p-side shows abrupt change in capacitance above the bias voltage of 100V.

Connections to 16 individual strips of the sensor are made and capacitance for each strip of p and n-side is measured at depletion voltage and shown in Figure 5.11. The capacitance of the strips of n-side and p-side should increase linearly with the increment in strip length. However, it is observed that capacitance of n-side strips vary linearly with their length but this is not the case of p-side strips for this particular sensor.

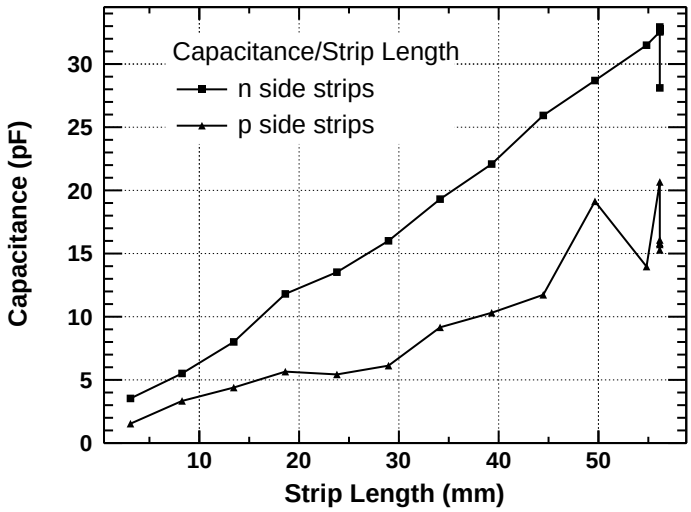

Figure 5.11: Variation of capacitance with the length of strips.

5.3 DC - DC Converters

A DC-DC converter is a device that accepts a DC input voltage and produces a DC output voltage. Generally, DC-DC converters are used to provide power regulation, noise isolation etc. The $\overline{\text{P}}$ANDA experiment utilizes DC-DC converters for the front-end electronics of the Micro Vertex Detector to supply power. Quality Assurance tests have been made on FEASTMP DC-DC converter modules which are developed by from CERN. The assembled DC-DC converter module is shown in Figure 5.12 and several features of these converter modules are tabulated in Table 5.1.

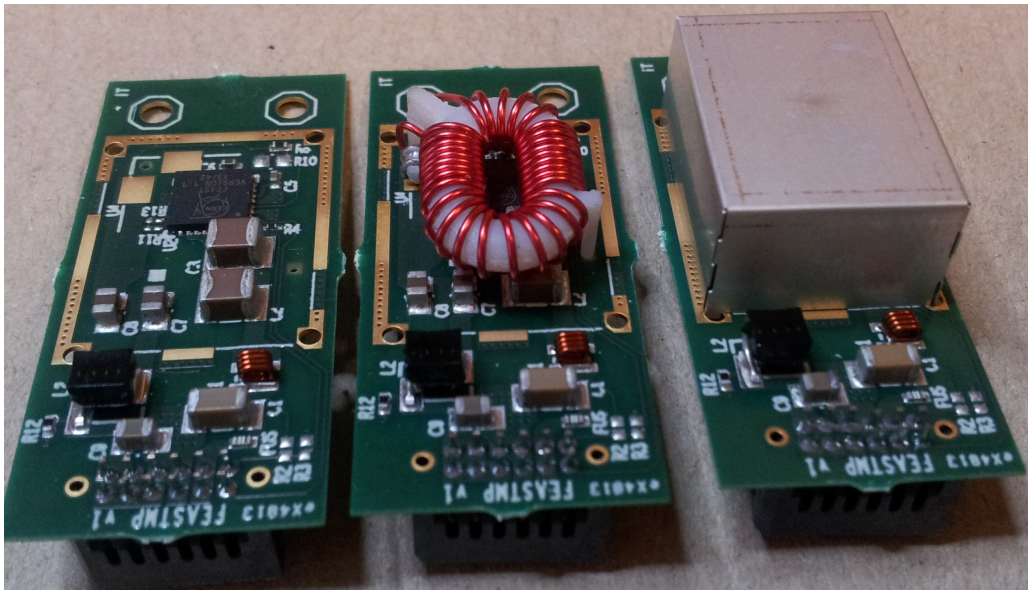

Figure 5.12: FEASTMP DC-DC converter modules fully assembled (right), with shield removed (center) and with main inductor removed (left) [58].

Table 5.1: Features of FEASTMP DC-DC converter modules.

Features	Values
Input voltage	5V - 12V
Output current	1A - 4A
Output voltage	1.2V or 2.5V
Output power	10 W
Efficiency	85 %

5.3.1 Quality Assurance (QA) Tests on DC-DC Converter Modules

Quality test measurements have been made on the available 1.2V and 2.5V output FEASTMP modules without any cooling system. A Block diagram of the measurement setup is shown in Figure 5.13.

Following components are used for the measurement setup:

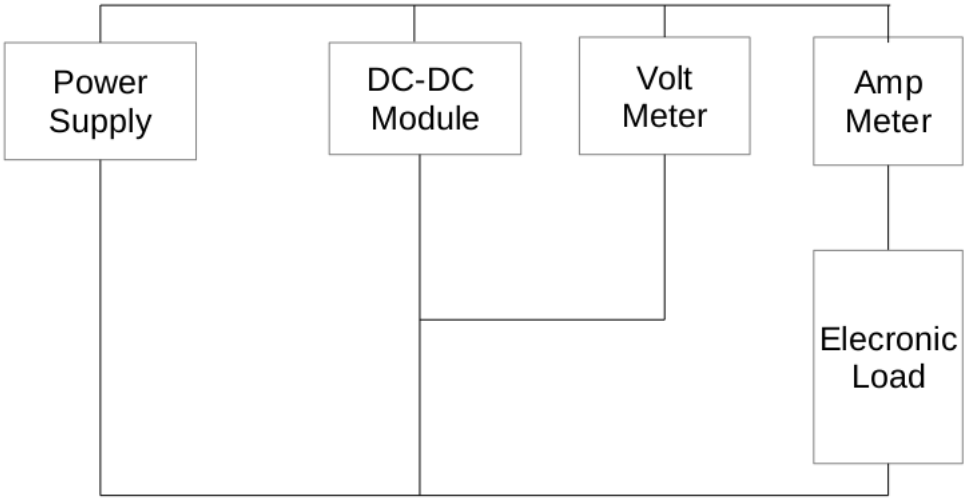

Figure 5.13: Block diagram for the measurement test setup.

- A FEASTMP DC-DC converter module
- Power supply to provide the input voltage
- An Ameter and a voltmeter to measure current and voltage
- An electronic load to measure the output current

Quality Assurance tests include I-V characterization, efficiency measurement and load regulation tests for these modules. All the measurements were performed without any cooling system.

5.3.1.1 I-V Characteristics of DC-DC Converter Module

The variation of the output voltage for different output currents at different input voltages i.e. I-V characteristics of the device have been measured.

Figures 5.14a and 5.14b show the I-V characteristics for two different modules.

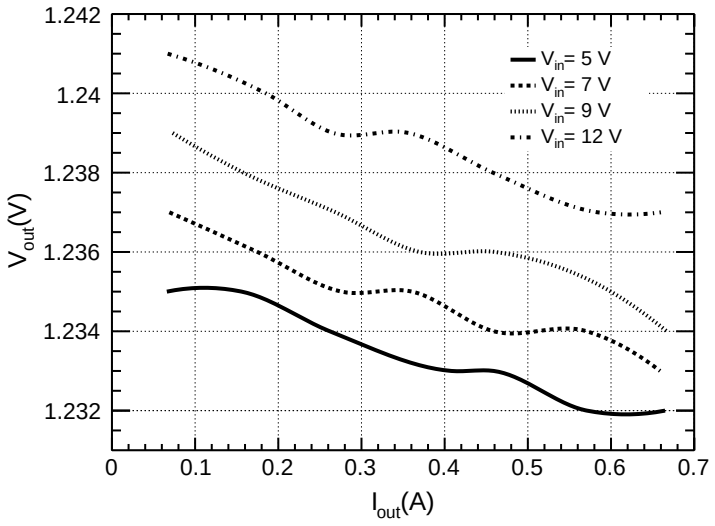

(a)

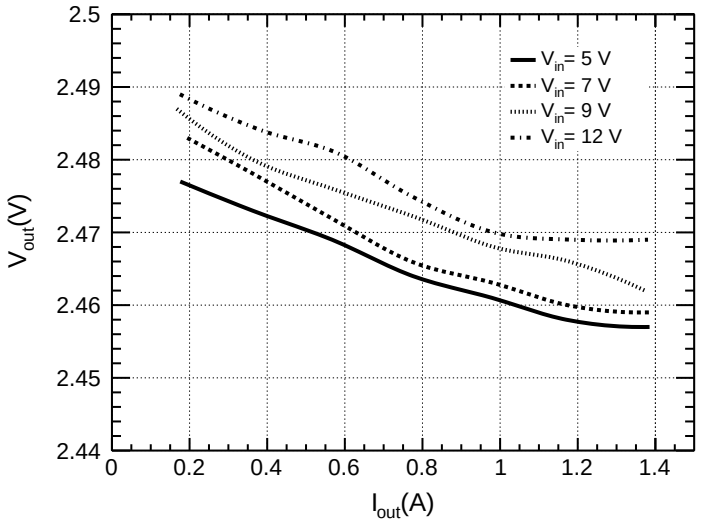

(b)

Figure 5.14: I-V characteristics for 1.2V and 2.5V DC-DC Converter Modules at different input voltages. Panels (a) and (b) are shown for 1.2V and 2.5V DC-DC converters module respectively.

The drop in output voltage with the increment in the output current has been observed.

5.3.1.2 Efficiency Measurements

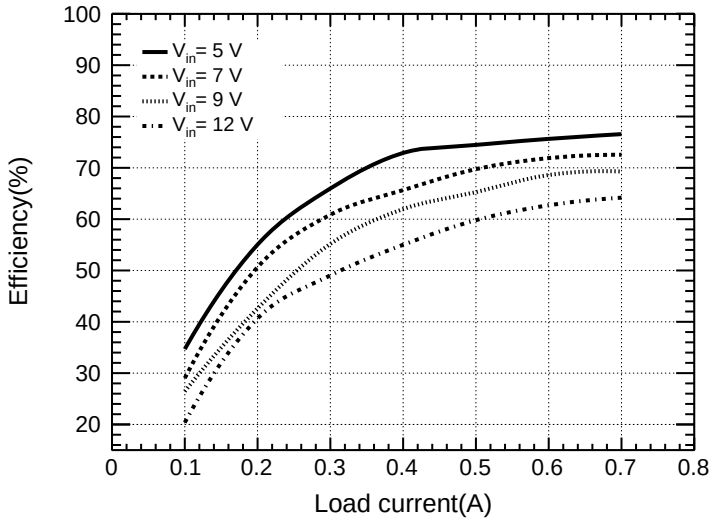

(a)

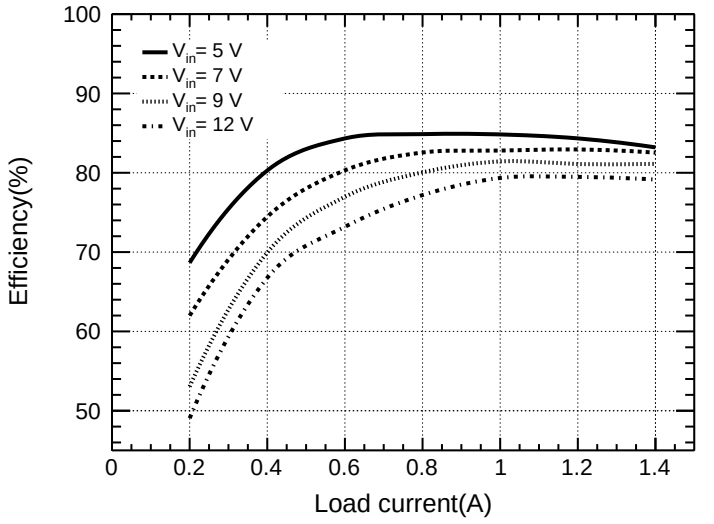

(b)

Figure 5.15: Efficiency vs. output current for 1.2V and 2.5V DC-DC Converter Modules at different input voltages. Panels (a) and (b) are shown for 1.2V and 2.5V DC-DC converters module respectively.

The efficiency of the DC-DC converters is defined as the ratio of the output power to the input power. The efficiency of the 1.2V output voltage module is optimized at 0.7A output current around 70% for input voltage range between 5 to 12V. We could not test above 0.7A load current due to the high resistivity of the thin connecting wires used in the setup. For the 2.5V DC-DC converter, the highest efficiency is reached at 0.6A for 5V input

voltage. The variation of the efficiency with the load current is shown in Figures 5.15a and 5.15b.

5.3.1.3 Load Regulation

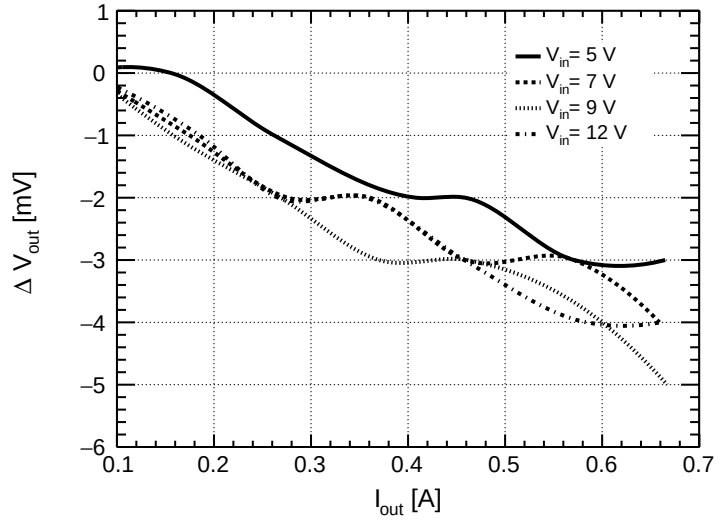

(a)

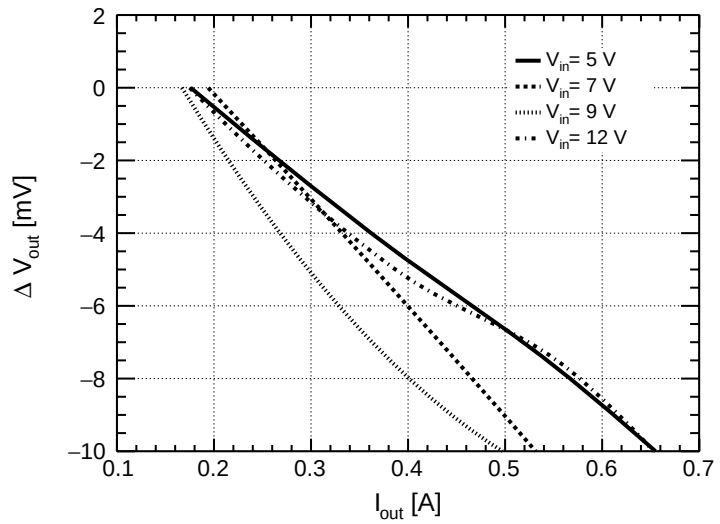

(b)

Figure 5.16: Load regulation for 1.2V and 2.5V DC-DC Converter Modules at different input voltages. Panels (a) and (b) are shown for 1.2V and 2.5V DC-DC converters module respectively.

The output voltage is set to zero and difference of output voltages with the variation of load current at different input voltage has been plotted to see how the load regulate at different input voltages and are shown in

Figures 5.16a and 5.16b. The drop independent on the input voltage, is almost linear and shown in following figures for different modules.

Chapter 6

Summary and Conclusions

The non-perturbative regime of QCD has been explored extensively over the last few decades with many questions remaining answered. The future $\overline{\text{P}}$ANDA experiment is proposed to explore some of them, namely confinement of quarks, structure of hadrons, existence of glueballs and hybrids, origin of mass of hadrons etc.

More specifically, the $\overline{\text{P}}$ANDA experiment aims to focus on the study of charmonium states, glueballs and hybrid nuclei, the electromagnetic form factor of the proton and for double hypernuclei. A more detailed discussion is given in Chapter 1 of this thesis.

The $\overline{\text{P}}$ANDA detector will do tracking as well as particle identification of produced particles at an incoming beam of antiproton in the range 1.5 to 15 GeV/c. $\overline{\text{P}}$ANDA is a 4π detector with high momentum resolution and particle identification capability. The interaction region will be surrounded by the target spectrometer, containing the folowing sub-detector systems: Micro Vertex Detector (MVD), Straw Tracker Tube (STT), Gas Electron multipliers (GEM) etc. and extended by the forward spectrometer with the Forward Tracking System (FTS), forward Electromagnetic Calorimeter (EMC) and Muon Detection System, etc as discussed in Chapter 2.

There is a large gap between the MVD and GEM detectors without any tracking detectors. The Lambda Disks Detector is introduced in this volume, which is described in Chapter 3. By including the Lambda Disks Detector into the $\overline{\text{P}}$ANDA setup, there is a possibility to improve the hyperon studies in the $\overline{\text{P}}$ANDA physics program. It will increase the reconstruction probability of hyperons with a large lifetime and extend their measurements up to higher beam momentum with large statistics. This

thesis presents a the feasibility study of the Lambda Disks Detector in the $\overline{\text{P}}$ANDA setup.

We have presented the simulation studies of three channels with and without the Lambda Disks Detector. We have selected the $\bar{p}p \rightarrow \bar{\Lambda}\Lambda$ hyperon channel to study the reconstruction performance of Λ hyperons with the Lambda Disks Detector added to $\overline{\text{P}}$ANDA setup. The reconstruction of the Λ decay products (mostly from $\Lambda \rightarrow p\pi^+$ and $\bar{\Lambda} \rightarrow p\pi^-$) differs from ordinary charged particle reconstruction in $\overline{\text{P}}$ANDA as the charged particles do not come from the interaction point.

As the addition of a new detector should not affect the reconstruction of other important channels. Therefore, two well reconstructed channels ($\bar{p}p \rightarrow D^{*+}D^{*-}$ and $\bar{p}p \rightarrow J/\psi\pi^+\pi^-$) are chosen to determine the effect of Lambda Disks Detector on the reconstruction of these channels. These channels contain charm quarks and are very important for the charmonium physics program of $\overline{\text{P}}$ANDA.

We have simulated and reconstructed the $\bar{p}p \rightarrow \Lambda\bar{\Lambda}$ channel using the $\overline{\text{P}}$ANDA simulation framework at beam momentum 1.8 GeV/c, which is near to the production threshold and at 4 GeV/c to compare the performance of the detector with increasing beam momentum. In order to perform the feasibility studies for the Lambda Disks Detector, we have studied the angular distributions from the daughter particles of the Lambda (Λ) hyperons to map the direction of the final state particles inside the target spectrometer. Momentum correlations (p_z versus p_T) of Λ hyperons as well as their decay products are studied to understand the kinematics of these particles. The decay vertex positions of the produced Λ hyperons are studied to estimate the fraction of events decaying before and after the LDD, since this detector detects only final state particles (p, $\bar{p}$, π^-, π^+) from this decay channel.

We have also studied the vertex and momentum resolution from $\bar{p}p \rightarrow \Lambda\bar{\Lambda}$, with and without the LDD. We found that the vertex resolution of Λ and $\bar{\Lambda}$ remain unchanged after the addition of LDD. However, we observed that the addition of LDD worsens the momentum resolution

in the z-direction. Hit count studies are performed of the daughter particles from both hyperons and it is observed that the hit counts increase by adding the LDD to the detector set up. At low beam momentum (1.8 GeV/c), the most significant effect is an increse of the number of hits for protons in the angular range of the LDD. The average number of hit points per track rises above four, which allows individual tracking for the particle. At a higher beam momentum (4.0 GeV/c), antiprotons are forward boosted in comparison to protons and usually have more than six hits in the angular range covered by the Lambda Disks. Final state pions (π^+ and π^-) register more than six hits after the addition of LDD to $\overline{\text{P}}$ANDA. The increse in the number of particle hits by adding the LDD is a positive sign towards its development. We have estimated the mass resolution and reconstruction efficiency of Λ and $\bar{\Lambda}$ hyperons with and without the LDD, which are the most important parameters for the feasibility studies of this detector. A double Gaussian function is fit to the mass distribution of hyperons because the combinatorial background is also Gaussian in nature. The average reconstruction efficiency for Λ is around 42% at the lower beam momentum and 25% at the higher beam momentum whereas for $\bar{\Lambda}$ is observed 48% at the lower beam momentum and 52% at the higher momentum. Average reconstruction efficiency of Λ decreases whereas the $\bar{\Lambda}$ reconstruction efficiency increases with the higher beam momentum. Overall, the $\Lambda\bar{\Lambda}$ reconstruction efficiency is found to be 28.5% and 20% at beam momenta 1.8 GeV/c and 4.0 GeV/c, respectively.

The track reconstruction efficiency and mass resolution are studied for two mesonic channels. Simulation results show that the reconstruction efficiency and mass resolution of these two channels are not affected by the addition of the LDD to the $\overline{\text{P}}$ANDA setup.

As a part of this thesis to gain hardware experience, we have done the characterization of trapezoidal Double-sided Silicon Strip sensors. We need to perform Quality Assurance (QA) tests, which is basically performing I-V and C-V characterization for these sensors. The most important parameter for these QA tests are the leakage current and depletion voltage

of the whole sensor as well as for the individual strips. It is essential to know these parameters as it is important for the operation. We have done the characterization of the DSSDs using two different biasing techniques with a probe station and a dedicated test board setup in Forschungszentrum Jülich, Germany. From the I-V and C-V characterization results, we have observed that extracted values of the required parameters are in good agreement with the values measured by the manufacturer (CiS) of these sensors. The value of the leakage current and depletion voltage for each characterized sensor is found to be near about 4μA and 100V, respectively. The leakage current and depletion voltage of strips from n-side and p-side are also measured and found to be about 2 μA and 100V, respectively.

The QA tests on the DC-DC converters are also performed, which is required to supply the constant power to each sensor used for the LDD. The QA tests include I-V characteristics, efficiency measurements, load regulation on the available DC-DC converter modules and our results are found in good agreement with the results of these converter modules manufacturers data.

One of the important studies for developing a detector is the estimation of the material budget. We have performed material budget studies for the current geometry of the LDD. The sensors of inner and outer ring are made up of silicon of the carbon support structure. The material budget used for the LDD should be as low as possible due to the restriction imposed by the detectors located in the forward and backward direction. The concerning parameter for the material budget is the fractional radiation length for the introduced materials and that is found to be 20% of a radiation length (X_0).

It is concluded from these simulation studies that the reconstruction efficiency and resolution of the produced Λ hyperons are not affected after the addition of the Lambda Disks Detector. However, the number of hit points per track are increasing with the addition of these two disks to the central detector system of $\overline{\text{P}}$ANDA, which is a positive sign towards the development of the Lambda Disks Detector.

In this work, an ideal track finder algorithm is used to find the tracks from secondary decay vertices, considering them decayed at origin, due to the unavailability of a secondary track finder algorithm with the present PandaRoot software. Also, the Lambda Disks Detector are kept at fixed positions, one is at 40 cm and another is at 60 cm from the interaction point for this study. Once the secondary tracking algorithm is implemented within the PandaRoot Software, one should repeat the same study with a new tracking algorithm. It is also important to see the variation of reconstruction efficiency by changing the locations of the LDD in order to optimize the position of the detector. In this analysis, we have used the existing kinematic vertex fitter (PndKinVtxFitter) and we have observed that the χ^2 probability distribution of the Λ hyperons rises sharply at the upper end of the spectra. Therefore, covariance matrix in the kinematic fitter needs to be improved for the proper description of the measurement errors.

Finally, if one considers the improvement in the reconstruction efficiency of hyperons with LDD, then $\overline{\text{P}}$ANDA should add the LDD. This will help to improve the hyperon studies.

Another major concern is the required space for the routing of the LDD supplies through the whole $\overline{\text{P}}$ANDA setup. There is very limited space in the backward direction. However, one can think of routing in the forward direction first and could be able to take it in the backward direction parallel to the STT if the addition of the LDD shows a significant improvement in the reconstruction of hyperons.

Bibliography

[1] David Griffiths. Introduction to Elementary Particles , 2nd, Revised Edition. ISBN: 978-3-527-40601-2.

[2] K.A. Olive et al. (Particle Data Group), Chin. Phys. C, 38, 090001 (2014) and 2015.

[3] Quark model. `http://www.wikiwand.com/en/Quark_model`.

[4] The Quark Model. `http://web2.physics.fsu.edu/~roberts/roberts_quark_model.html`.

[5] W. Erni *et al.* [PANDA Collaboration], "Physics Performance Report for PANDA: Strong Interaction Studies with Antiprotons," arXiv:0903.3905 [hep-ex].

[6] T. Johansson [PS185 Collaboration], "Antihyperon-hyperon production in antiproton-proton collisions," AIP Conf. Proc. **796**, 95 (2005).

[7] P. D. Barnes *et al.*, "Observables in high statistics measurements of the reaction $\bar{p}p \to La\bar{m}bdaLambda$," Phys. Rev. C **54**, 1877 (1996).

[8] V. Flaminio, W. G. Moorhead, D. R. O. Morrison and N. Rivoire, "Compilation of Cross-sections. 3. P and $\bar{P}$ Induced Reactions," CERN-HERA-84-01.

[9] H. Becker *et al.* [CERN-Munich Collaboration], "Measurement of the Reactions $\bar{P}P \to \bar{\Lambda}\Lambda$, $\bar{p}p \to \bar{\Lambda}\Sigma^0$ and $\bar{P}P \to \bar{\Lambda}$ (Missing Mass) at 6-GeV," Nucl. Phys. B **141**, 48 (1978).

[10] K. Schnning *et al.* [PANDA Collaboration], "Antihyperon-hyperon production in antiproton-proton annihilations with PANDA," J. Phys. Conf. Ser. **503**, 012013 (2014).

[11] Conceptual Design Report. https://www-alt.gsi.de/documents/FOLDER-1080636714.html.

[12] Facility for Antiproton and Ion Research. http://www.fair-center.de.

[13] D. Bettoni, "The PANDA experiment at FAIR," eConf C **070805**, 39 (2007).

[14] A. Lehrach, K. Bongardt, B. Lorentz, R. Maier, D. Prasuhn, H. Stockhorst, R. Tolle and D. M. Welsch, "Beam dynamics of the High-Energy Storage Ring (HESR) for FAIR," Int. J. Mod. Phys. E **18**, 420 (2009).

[15] R. Maier, "The High-Energy Storage Ring (HESR)," Conf. Proc. C **110328**, 2104 (2011).

[16] Facility for Antiproton and Ion Research. http://www.fair-center.eu/public/experiment-program.html.

[17] APPA-Collaborations. Atomic and plasma physics, and applied sciences in bio, medical and material sciences (APPA) research pillar Science case. http://www.flairatfair.eu/typo3/fileadmin/files/documents/reports\/APPA_SC_2012-11-13-final.pdf.

[18] Facility of Antiproton and Ion Reserach. http://www.fair-center.eu/for-users/experiments/cbm.html.

[19] Facility of Antiproton and Ion Reserach. http://www.fair-center.eu/en/for-users/experiments/nustar.html.

[20] Facility of Antiproton and Ion Reserach. http://www.fair-center.eu/public/experiment-program/antiproton-physics/panda.html.

[21] CAD-Renderings of the PANDA Detector. https://panda-wiki.gsi.de/foswiki/bin/view/Detector/Pictures.

[22] The PANDA Collaboration."Technical Design Report for The Cluster-Jet Target and Developments for the Pellet Target".

[23] The PANDA Collaboration, Technical Design Report for Solenoid and Dipole Spectrometer Magnets.

[24] The PANDA Collaboration, W. Erni et.al. Technical Design Report for the PANDA Micro Vertex Detector. http://arxiv.org/abs/1207.6581v2.

[25] The PANDA Collaboration, W. Erni et.al. Technical Design Report for the PANDA Straw Tube Tracker. http://arxiv.org/abs/1205.5441.

[26] https://panda.gsi.de/oldwww/framework/det_iframe.php?section=GEM.

[27] W. Erni et.al. Technical Design Report for PANDA Electromagnetic Calorimeter (EMC), http://arxiv.org/pdf/0810.1216v1.pdf

[28] https://panda.gsi.de/article/time-of-flight-detectors.

[29] Technical Progress Report for PANDA. https://panda.gsi.de/oldwww/archive/public/panda_tpr.pdf.

[30] W. Erni et. al. "Technical Design Report for the: PANDA Muon System", 2012. http://www-panda.gsi.de/archive/MuonTDR/Muon_TDR.pdf.

[31] Thomas Würschig, "Design optimization of the PANDA Micro-Vertex-Detector for high performance spectroscopy in the charm quark sector", Dissertation, 19. JUL. 2011, Bonn.

[32] F.Hügging. "Development of a Micro-Vertex-Detector for the PANDA-Experiment at the FAIR facility", IEEE Nuclear Science Symposium Conference Record, N30(190):1239–1243, 2006.

[33] I. Abt, "Silicon Detectors," NATO Sci. Ser. C **534**, 295 (1999).

[34] W. R. Leo, "Techniques for Nuclear and Particle Physics Experiments: A How to Approach," Berlin, Germany: Springer (1987) 368 p

[35] Sanjay Kumar Swarnkar , B.Tech Project Report, 2014. IIT-Indore.

[36] FairRoot. `https://fairroot.gsi.de`.

[37] CERN Root. `https://root.cern.ch`.

[38] R. Brun, R. Hagelberg, M. Hansroul and J. C. Lassalle, "Geant: Simulation Program for Particle Physics Experiments. User Guide and Reference Manual," CERN-DD-78-2-REV, CERN-DD-78-2.

[39] S. Agostinelli *et al.* [GEANT4 Collaboration], "GEANT4: A Simulation toolkit," Nucl. Instrum. Meth. A **506**, 250 (2003). doi:10.1016/S0168-9002(03)01368-8

[40] PandaRoot. `https://panda-wiki.gsi.de/foswiki/bin/view/Computing/PandaRoot`.

[41] R. Kliemt, Simulations with the Panda Micro-Vertex-Detector. PhD thesis, University of Bonn, 2012.

[42] PandaROOT Event Generators. `https://panda-wiki.gsi.de/foswiki/bin/view/Computing/PandaRootGenerators`.

[43] A. Capella, U. Sukhatme, C. I. Tan and J. Tran Thanh Van, "Dual parton model," Phys. Rept. **236**, 225 (1994). doi:10.1016/0370-1573(94)90064-7

[44] S. A. Bass *et al.*, "Microscopic models for ultrarelativistic heavy ion collisions," Prog. Part. Nucl. Phys. **41**, 255 (1998) [Prog. Part. Nucl. Phys. **41**, 225 (1998)] doi:10.1016/S0146-6410(98)00058-1 [nucl-th/9803035].

[45] C. Hoppner, S. Neubert, B. Ketzer and S. Paul, "A Novel Generic Framework for Track Fitting in Complex Detector Systems," Nucl.

Instrum. Meth. A **620**, 518 (2010) doi:10.1016/j.nima.2010.03.136 [arXiv:0911.1008 [hep-ex]].

[46] R.E. Kalman. A new approach to linear filtering and prediction problems. `https://www.cs.unc.edu/~welch/kalman/media/pdf/Kalman1960.pdf`.

[47] V. Innocente et al. The GEANE program. CERN Program Library, 1991. W5013-E.

[48] `https://panda-wiki.gsi.de/foswiki/bin/view/Computing/PandaRootAnalysisJuly13`.

[49] S. Spataro [PANDA Collaboration], "Simulation and event reconstruction inside the PandaRoot framework," J. Phys. Conf. Ser. **119**, 032035 (2008) and references therein.

[50] P. D. Barnes *et al.*, Observables in high statistics measurements of the reaction $\bar{p}p \to \bar{\Lambda}\Lambda$," Phys. Rev. C **54**, 1877 (1996).

[51] P. D. Barnes *et al.*, "Study of the Reaction $\bar{p}p \to \bar{\Lambda}\Lambda$ Near Threshold," Phys. Lett. B **189**, 249 (1987).

[52] T. Johansson [PS185 Collaboration], "Antihyperon-hyperon production in antiproton-proton collisions," AIP Conf. Proc. **796**, 95 (2005). doi:10.1063/1.2130143

[53] H. Becker *et al.* [CERN-Munich Collaboration], "Measurement of the Reactions $\bar{P}P \to \bar{\Lambda}\Lambda$, $\bar{p}p \to \bar{\Lambda}\Sigma^0$ and $\bar{P}P \to \bar{\Lambda}$ (Missing Mass) at 6-GeV," Nucl. Phys. B **141**, 48 (1978). doi:10.1016/0550-3213(78)90333-4

[54] J. Beringer *et al.* [Particle Data Group Collaboration], "Review of Particle Physics (RPP)," Phys. Rev. D **86**, 010001 (2012). doi:10.1103/PhysRevD.86.010001

[55] Documentation of Rho Classes. `https://panda-wiki.gsi.de/foswiki/bin/view/Computing/PandaRootAnalysisJuly13`.

[56] D. Deerman, "Development of the $\overline{\text{P}}$ANDA MVD Trapezoidal Sensors and a Feasibility Study of the $\bar{p}p \rightarrow \Lambda_c\bar{\Lambda}_c$ Reconstruction", PhD Thesis 2015.

[57] S.M. Sze, "Physics of Semiconductor Device", 3rd Edition, Welay, 2006.

[58] `http://project-dcdc.web.cern.ch/project-dcdc/public/DCDCmodulesDatasheets.html`.